POLITECNICO DI TORINO
Repository ISTITUZIONALE

BIPV Yield Assessment for Transparent Envelope Applications in Early-Stage Building Design: A Cross-Tool Comparison

Original
BIPV Yield Assessment for Transparent Envelope Applications in Early-Stage Building Design: A Cross-Tool Comparison / Krupka, D., Raad, A., Li Castri, G., Favoino, F.. - In: ENERGIES. - ISSN 1996-1073. - 19:15(2026). [10.3390/en19153503]

Availability:
This version is available at: 11583/3016358 since: 2026-10-06T12:19:48Z

Publisher:
Multidisciplinary Digital Publishing Institute (MDPI)

Published
DOI:10.3390/en19153503

Terms of use:

This article is made available under terms and conditions as specified in the corresponding bibliographic description in the repository

Publisher copyright

(Article begins on next page)

11 October 2026

energies

MDPI

Article

BIPV Yield Assessment for Transparent Envelope Applications in Early-Stage Building Design: A Cross-Tool Comparison

Debora Krupka, Aseel Raad, Ginevra Li Castri and Fabio Favoino *

Technology Energy Building Environment Research Group, Energy Department, Politecnico di Torino, Corso Duca degli Abruzzi, 24, 10129 Turin, Italy; debora.krupka@polito.it (D.K.); aseel.raad@polito.it (A.R.); ginevra.licastri@polito.it (G.L.C.)

* Correspondence: fabio.favoino@polito.it

Abstract

Building-integrated photovoltaics (BIPVs) can expand the available photovoltaic area on buildings, especially in dense urban contexts with limited roof surfaces. For transparent-envelope applications, such as photovoltaic shading devices (PVSDs) and semi-transparent photovoltaic glazing (STPV), PV-yield assessment is particularly challenging because PV elements also function as part of the building envelope. Their energy yield depends on multiple interacting factors: irradiation, orientation, shading, incidence-angle effects, operating temperature, and, for STPV, glazing thermal behavior. In early-stage building design, however, these effects must be assessed while system characteristics are still evolving, and detailed product or module data are often unavailable. To address this gap, this study develops and evaluates an EnergyPlus-based approach for PV-yield assessments for transparent-envelope BIPV applications. The approach replaces fixed PV efficiency with a time-dependent effective efficiency that accounts for incidence-angle reflection and temperature-related efficiency losses. It is evaluated through a cross-tool comparison with established PV-yield assessment tools. For PVSD, the comparison separates unshaded conditions, louver self-shading, and urban-context shading. For STPV, it includes an analysis of the PV cell-temperature estimation and the link between electricity generation and glazing heat balance. Results show that PVSD yield differences are mainly governed by shading representation, while STPV results are more sensitive to cell-temperature assessment than to thermal coupling effects. Overall, the approach provides a consistent basis for comparing PVSD and STPV yield under early-stage input constraints, while including selected AOI- and temperature-related efficiency effects.

Keywords: building-integrated photovoltaics (BIPVs); transparent-envelope BIPV; photovoltaic shading devices (PVSDs); semi-transparent photovoltaic glazing (STPV); PV yield assessment; early-stage building design; EnergyPlus; cross-tool comparison

Check for updates

Academic Editors: Feng Xu and Baohua Wen

Received: 15 May 2026
Revised: 19 June 2026
Accepted: 23 June 2026
Published: 25 July 2026

Copyright: © 2026 by the authors. Licensee MDPI, Basel, Switzerland. This article is an open access article distributed under the terms and conditions of the Creative Commons Attribution (CC BY) license.

1. Introduction

Buildings accounted for 34% of energy-related CO_2 emissions in 2023 [1], making the building sector central to climate change mitigation. EU building policy, including the nearly zero-energy building (NZEB) requirement and the zero-emission building (ZEB) concept introduced in the 2024 EPBD recast, reinforces the need for high-performance buildings supplied largely by renewable energy [2]. Photovoltaic (PV) systems are therefore a key strategy for onsite renewable electricity generation and for reducing building-related emissions. Conventional rooftop PV is often a straightforward building-mounted option,

but in dense urban areas and taller buildings, the available roof area may be insufficient relative to the building energy demand. Building-integrated photovoltaics (BIPVs) can expand the available photovoltaic surface beyond conventional rooftop systems, but this also places PV-yield assessments under envelope-integrated conditions shaped by the façade geometry, shading, and the surrounding built context.

BIPV systems can be integrated into different parts of the building envelope, including roofs, façades, and external building-skin devices [3]. Within this broader field, this paper focuses on transparent-envelope BIPV applications. These are defined here as BIPV systems that generate electricity while influencing the amount of solar radiation entering through fenestration-related envelope components. The two system families used to represent this scope are photovoltaic shading devices (PVSDs) and semi-transparent photovoltaic windows (STPVs), with representative examples illustrated in Figure 1. PVSDs integrate PV modules into shading elements that generate electricity while providing solar-control functions, such as shading and daylight modulation. The PVSD configurations discussed in the literature include louvers, blinds, overhangs, and fixed or adjustable shading devices [4,5]. STPV windows integrate PV-active material into glazing elements, transmitting part of the incident radiation while absorbing or converting another part into electricity [5–7].

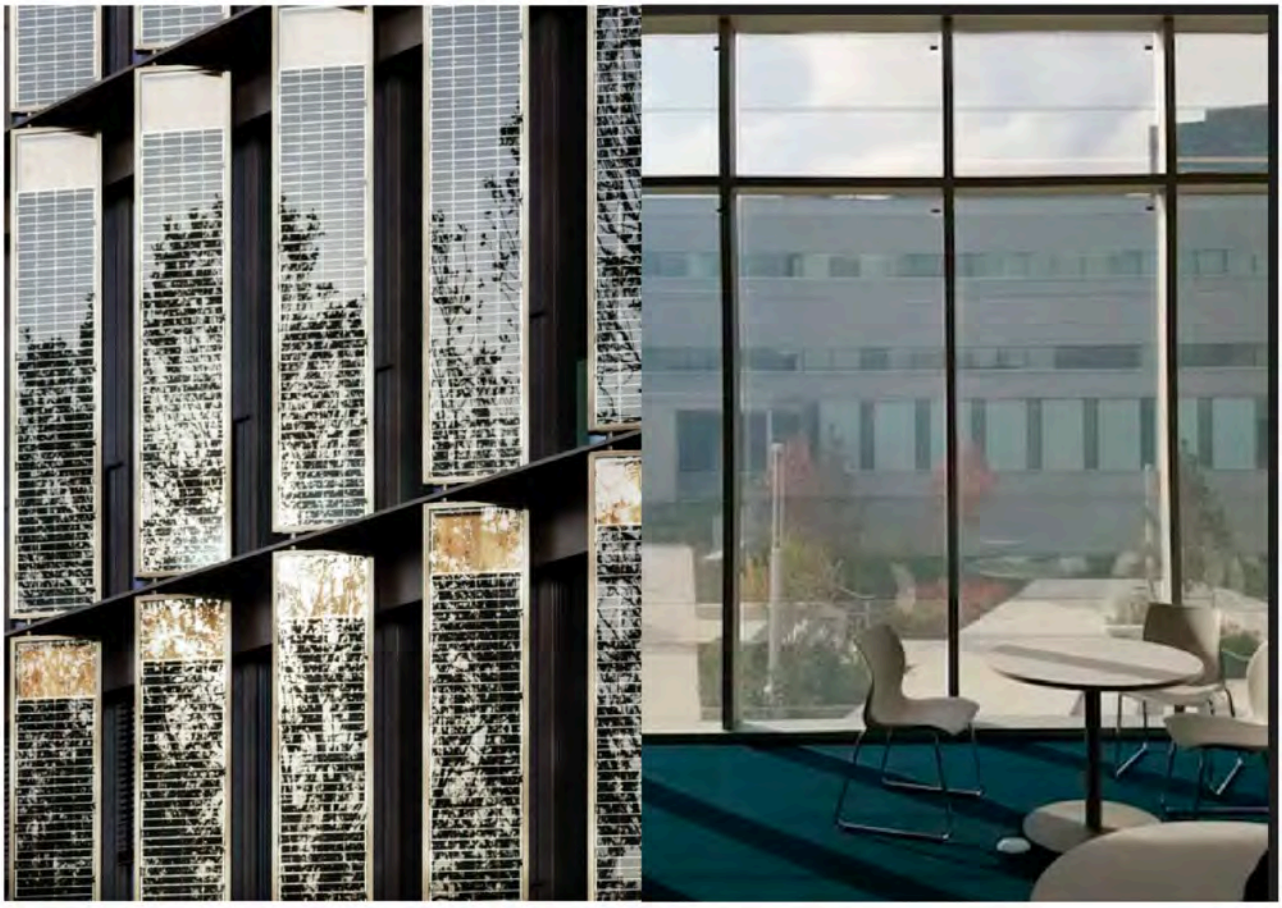

Figure 1. Representative examples of transparent-envelope BIPV applications considered in this paper: (**Left**), photovoltaic shading devices integrated into external façade shading elements, reproduced with permission from ingenhoven architects/HGEsch [8]; (**right**), semi-transparent photovoltaic windows integrated into glazing, reproduced with permission from onyx solar [9].

Although PVSD and STPV windows both affect fenestration-related solar radiation, they do so through different envelope positions. PVSDs are external PV-integrated shad-

ing elements that intercept solar radiation before it reaches the window, whereas STPV windows integrate PV-active cells or layers into the glazing system itself [6,10–12]. This distinction matters for PV-yield assessment because PVSD performance is mainly governed by external geometry and shading conditions, while STPV performance depends more directly on glazing-integrated optical, thermal, and electrical behavior. In this study, external PV louvers and STPV windows are selected as representative typologies for these two system families; other PVSD positions and semi-transparent applications, such as skylights, are not within the scope. Although transparent-envelope BIPV systems also influence daylight, thermal loads, and indoor comfort, this paper focuses specifically on PV-yield assessment, defined as the estimation of expected PV electricity generation. Such yield estimates are needed to compare design alternatives and to evaluate their contribution to building performance and renewable energy targets.

The need for yield information arises early in the design process, as decisions regarding the building form, envelope composition, and energy systems can still strongly shape sustainability performance. Subsequent changes in later design stages become more constrained and costly [13]. In the context of BIPVs, this timing is especially important because the system is not an independent building element. Its location, orientation, geometry, active area, transparency level, and module technology are linked to the building envelope and can therefore affect both electricity generation and overall building performance. This creates a methodological challenge: yield estimates are needed before many parameters that define PV output have been fixed. BIPV options may still change in terms of the system family, geometry, orientation, active PV area, transparency level, and module technology, while the specific PV product, module parameters, electrical layout, and detailed loss assumptions may still be pending. Although detailed electrical PV-yield assessment models can provide more specific performance estimates, they usually require these product and system assumptions to be defined first. This creates an early-stage input mismatch. BIPV alternatives must be compared while geometry, system type, active area, transparency, and PV technology may still change, but many product-specific and electrical-system parameters are not yet available.

This mismatch becomes clearer when considering what the PV-yield calculation is expected to represent. In this context, a PV-yield model is defined as the mathematical or computational representation employed to estimate the electrical output of a PV-active surface under specified environmental, geometric, and system assumptions. In established PV modeling workflows, this estimation establishes a correlation between irradiance on the PV plane and the optical effects at the module surface, temperature-dependent conversion efficiency, electrical behavior, inverter behavior, and system-loss assumptions [14]. Full electrical-system effects, such as string layout, mismatch, inverter behavior, wiring, soiling, and degradation, are outside this early-stage modeling scope. Instead, the present modeling scope centers on three yield mechanisms that are both relevant to PV-yield estimation and directly linked to information commonly available in building-performance workflows at this stage: (i) shading; (ii) angle-of-incidence (AOI)-related reflection; and (iii) cell-temperature-related efficiency losses. This focus connects yield estimation with geometric, irradiance, and temperature information that can usually be generated within early design-stage building-performance simulations.

Among these selected effects, shading affects the irradiance incident on the active PV layer. This is especially relevant for BIPV systems, where different module positions, self-shading, and surrounding obstructions can produce non-uniform exposure [5,7]. AOI-related reflection is considered as an optical loss because oblique incidence reduces the fraction of light transmitted through the module front layer and reaching the cell [15,16]. Cell-temperature-related efficiency losses are considered because increasing module or cell

temperatures reduce PV electrical output, with temperature sensitivity depending on PV technology and mounting configuration [7,17]. In BIPV applications, these effects cannot be treated only as generic PV losses, because the PV surface is constrained by the building envelope. Its orientation, tilt, and exposure to surrounding obstructions are determined by architectural geometry and urban context [3,7]. As a result, shading, AOI-related reflection, and temperature effects are directly linked to the specific BIPV configuration being assessed. A yield model for transparent-envelope BIPV should therefore be able to represent these aspects without requiring the full input set of detailed electrical PV models.

As PVSD and STPV windows impose different envelope conditions, the relative importance of these effects can vary between the two system families. For PVSDs, the yield assessment is strongly influenced by geometry and exposure conditions, including the orientation, louver geometry, slat angle, mutual self-shading, surrounding obstructions, and associated AOI-related reflection and cell-temperature-related efficiency losses [4,5]. This study distinguishes among unshaded conditions, system self-shading, and urban-context shading in order to separate differences caused by the PV-yield model formulation from those caused by geometric boundary conditions. STPV windows instead introduce a different challenge because the PV-active layer is embedded within the glazing assembly. Incident radiation is transmitted, reflected, absorbed, or partly converted into electricity within the window construction. This radiation partitioning affects the glazing temperature, while the resulting glazing and PV-layer temperatures in turn influence conversion efficiency. The STPV yield assessment therefore depends on how the solar-optical properties, electricity extraction, glazing heat balance, and PV cell temperature are represented. Selected studies on STPVs have addressed these effects through adapted simulation workflows or external calculations, particularly with regard to how electricity generation is represented in the window model, how cell temperature is estimated, and whether electricity extraction is linked to the glazing heat balance [18,19]. The modeling challenge is therefore not only to estimate STPV electricity generation, but also to define how this estimate is linked to the thermal behavior of the glazing system.

These requirements define the main modeling problem addressed in this paper: the yield model must remain usable with limited early-stage inputs, but still respond to shading geometry, AOI losses, temperature effects, and the specific PVSD or STPV configuration. Current BIPV yield-assessment workflows do not fully resolve this mismatch. The issue is not the absence of simulation tools, but rather the difficulty of combining the building geometry and shading representation, selected PV-loss modeling, compatibility with building-performance workflows, and usability under limited input data. Previous tool-comparison and workflow studies clarify this difficulty but address it mainly by reviewing, mapping, or comparing available tools. A broader review by Wijeratne et al. [20] of distributed solar PV design and management tools shows that existing tools cover selected tasks, including irradiation assessments, energy-output prediction, 3D modeling, and shading-loss analysis. However, no single tool satisfies all project requirements considered in that review. This is relevant here, because a transparent-envelope BIPV assessment requires several of these tasks to be linked within one design workflow. For BIPV-related applications, this fragmentation becomes critical because façade integration, three-dimensional context shading, local assumptions, and building-coupled effects must be considered together rather than as separate calculations. The IEA PVPS Task 15 survey reinforces this BIPV-specific limitation by showing that BIPV design practice relies on fragmented methods and tools across solar irradiation modeling, BIPV power-output modeling, building-performance modeling, and design-outcome assessment [21]. A BIPV cross-tool study by Yang et al. [22] examined a complex BIPV case with roof, façade, and canopy PV systems and showed that key workflow steps are supported with different levels of detail. These steps include the geometry

handling, weather and solar-resource definition, system layout, loss assumptions, and energy-generation calculation. The study also highlights a practical trade-off: PV-oriented tools generally provide stronger capabilities for PV and electrical-performance assessments, whereas BIM-, CAD-, and building-performance-related workflows are more directly suited to three-dimensional geometry and shading-sensitive building contexts, but often with more limited electrical-modeling detail. These studies clarify why tool choice matters for BIPV yield assessment: geometry, shading, PV-loss assumptions, and electrical-model detail are handled differently across workflows. What remains less resolved is how an EnergyPlus-based building simulation workflow can include selected PV-conversion losses without requiring detailed product and electrical-system inputs.

Beyond workflow fragmentation, a related limitation appears at the model level within EnergyPlus-based PV assessments. Saber et al. [23] compared the EnergyPlus Simple, Equivalent One-Diode, and Sandia PV models for opaque building-mounted PVs, including roof and external-sunshade applications, and found that the more detailed EnergyPlus models represented PV output and cell-temperature behavior more accurately than the Simple model. For STPVs specifically, Mun et al. [24] investigated crystalline-silicon and amorphous-silicon semi-transparent PV modules in EnergyPlus/OpenStudio and showed that the Simple model cannot represent module-specific operating behavior beyond the entered efficiency input. This makes the efficiency input itself a critical point of extension. STPV studies by Leite Didoné and Wagner [18] and Zhou et al. [19] further show that the STPV yield assessment requires explicit assumptions about how electricity generation is represented in the window model, how cell temperature is estimated, and whether the electricity-converted solar fraction is linked to the glazing heat balance.

Together, these workflow- and model-level limitations point to the need for an intermediate PV-yield modeling approach. Such an approach should support comparison of evolving BIPV geometries, system types, and selected loss mechanisms before product-specific module data and detailed electrical-system definitions are fixed. Here, fixed-efficiency estimates refer to calculations in which incident irradiance is converted to electricity using a prescribed efficiency value, without a time-dependent correction for incidence-angle or temperature effects. An intermediate approach therefore sits between these simple but physically limited estimates and detailed electrical models that are more specific but require fixed product and electrical-system inputs. This position follows from the input mismatch described above.

This study addresses this gap by developing and evaluating a PV-yield model for transparent-envelope BIPV applications in early-stage building design. The proposed model builds on the EnergyPlus Simple PV model through an effective-efficiency formulation, in which fixed PV efficiency is replaced with a time-dependent effective efficiency that varies with simulated operating conditions. This formulation adjusts nominal PV efficiency using AOI and temperature modifiers. The resulting EnergyPlus modified Simple model (MSM) therefore differs from the standard EnergyPlus Simple PV model and from fixed-efficiency EnergyPlus workflows. The MSM keeps the Simple model structure and its limited input requirements. It adds hourly AOI- and temperature-related efficiency corrections using information already available from the EnergyPlus simulation. This allows PV yield to respond to geometry, shading, incidence angle, and cell temperature without requiring a detailed electrical PV model. The model is intended for a comparative assessment, not a final electrical system design. By replacing nominal efficiency with a time-dependent effective-efficiency input, it provides a more physically informed basis for comparing PVSD and STPV alternatives under early design-stage input constraints.

Accordingly, the objective of this study is to develop and benchmark a limited-input EnergyPlus modified Simple model for early design-stage PV-yield assessments

of transparent-envelope BIPV applications. The model combines geometry and shading representations from building-performance simulations with time-dependent AOI- and temperature-related PV-conversion effects. The benchmark is organized around the two modeling challenges established above. For PVSD, it tests model behavior across unshaded, self-shaded, and urban-shaded conditions. For STPVs, it examines how cell-temperature assessments and the thermal–optical–electrical coupling formulation affect yield estimates. This formulation, referred to here as the coupling formulation, describes the link between PV electricity generation and the glazing heat balance. The comparison is used as a benchmark-based plausibility check under aligned simulation assumptions, not as validation against measured performance. The following sections present the model formulation, comparative analysis design, and the resulting PVSD and STPV evaluations.

2. Materials and Methods

The methodology first defines the EnergyPlus-based PV-yield model and its effective-efficiency formulation. It then describes the comparative analysis for PVSD and STPV cases, followed by the KPIs, normalization basis, and post-processing procedure.

2.1. Simulation Environment and PV Model Basis

The PV-yield model was developed for use inside an EnergyPlus-based building simulation setup. Although this paper reports only PV-yield results, the model was designed to remain compatible with the wider BIPV assessment workflow from which the study is derived. EnergyPlus Version 24.2.0 was selected as the simulation tool because it allows PV generation to be evaluated within the same simulation environment used for energy and thermal building calculations.

EnergyPlus simulations were executed through Honeybee Version 1.9.0 in Grasshopper (Rhinoceros 8). Grasshopper was used to generate parametric geometries and case variants, while Honeybee provided the interface for translating these variants into EnergyPlus building performance simulation (BPS) models.

Within EnergyPlus, the available PV models were assessed against the requirements of the study. The model selected as the starting point needed to support comparisons across different BIPV system families as well as PV cell technologies, while remaining compatible with limited early-stage input information. On this basis, the EnergyPlus Simple model (SM) was selected. The aim was not to use the most detailed PV model available, but to use a model structure that is simple enough for consistent comparisons across system families and technologies while still allowing the physical impacts on PV yield addressed in this study to be incorporated.

The SM calculates PV electricity from incident irradiance on the PV surface, active PV area fraction, and a conversion-efficiency input. This efficiency input can be specified either as a fixed value or as a schedule. In its fixed-efficiency form, the model does not account for time-dependent changes in conversion efficiency under varying operating conditions. The scheduled-efficiency option was therefore used as the point of extension. Figure 2 summarizes the EnergyPlus Simple PV model structure and identifies the scheduled-efficiency input used in this study. The proposed model extends the SM by using this scheduled-efficiency option to represent a time-varying effective efficiency. This extended formulation is referred to as the EnergyPlus modified Simple model (MSM). The effective efficiency is defined here as an adjusted nominal efficiency that reflects the physical effects considered in the model. The effective-efficiency formulation is defined in the following section.

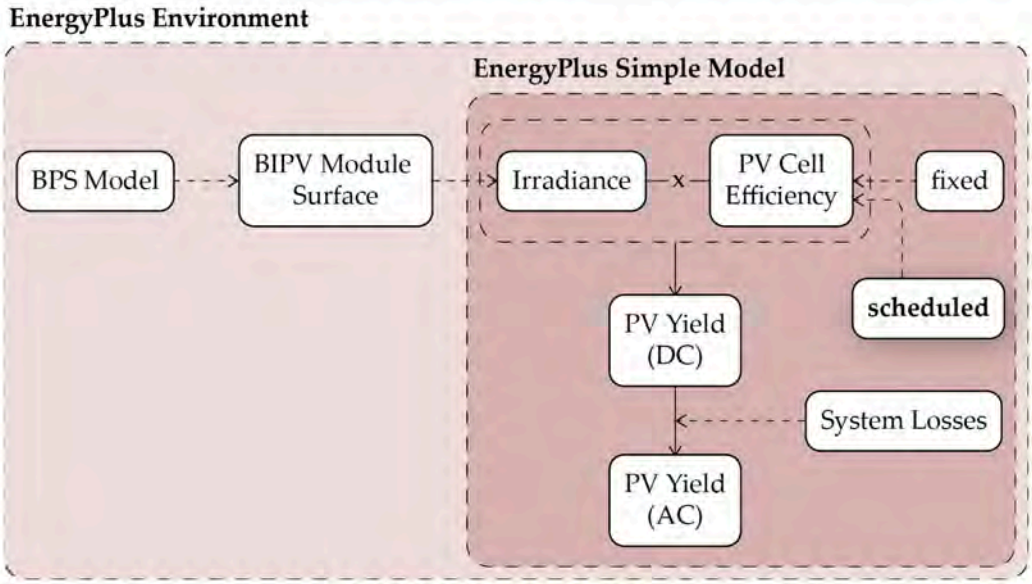

Figure 2. EnergyPlus Simple PV model structure and scheduled-efficiency input used as the basis for the modified Simple model.

2.2. Effective Efficiency Formulation

Based on this scheduled-efficiency structure, the effective efficiency is expressed as the nominal conversion efficiency adjusted by two dimensionless modifiers. The modifiers represent the two physical effects explicitly considered in the proposed model: angle-of-incidence (AOI) effects and temperature effects. The effective efficiency is calculated as follows:

$$\eta_{\text{eff}}(t) = \eta_{\text{nom}} \cdot M_{\text{AOI}}(t) \cdot M_T(t) \quad (1)$$

where $\eta_{\text{eff}}(t)$ is the time-dependent effective efficiency, η_{nom} is the nominal conversion efficiency, $M_{\text{AOI}}(t)$ is the AOI modifier, and $M_T(t)$ is the temperature modifier. The nominal efficiency represents the reference conversion efficiency under standard conditions, while the effective efficiency varies over time according to the simulated incidence-angle and cell-temperature conditions.

In this formulation, a modifier value of one indicates no additional reduction, while values below one reduce the nominal efficiency. The following subsections define the two modifier terms used in Equation (1).

2.2.1. AOI-Loss Representation

The AOI modifier represents the reduction in effective irradiance caused by increased front-surface reflection at oblique incidence angles. It is calculated separately for direct-beam, sky-diffuse, and ground-reflected irradiance components and then combined into a radiation-weighted modifier. This correction is included because transparent-envelope BIPV elements, including façades and shading devices, often operate at oblique incidence angles, where front-surface reflection can affect the PV yield [15].

AOI-related reflection is represented with the Martin–Ruiz correlation [16]. This incidence angle modifier (IAM) formulation requires one angular-loss coefficient and can therefore be applied consistently across the test cases without product-specific optical layer data. Other IAM approaches, including ASHRAE and Sandia, are also established in PV performance modeling; however, they rely on different empirical formulations, and the Sandia IAM model uses a multi-coefficient polynomial form [15]. Physical IAM models can represent layer-level optical behavior in greater detail, but they require product-specific optical inputs, such as layer properties, thicknesses, and refractive indices [15]. In the

present early-stage workflow, such product-specific optical data are not assumed to be available. Martin–Ruiz was therefore selected because it requires only one angular-loss coefficient and can be applied without product-specific optical layer data. The formulation is also implemented in pvlib and used by Solargis for angular-loss correction [25,26]. The AOI modifier is evaluated as

$$M_{\mathrm{AOI}} = \frac{B(1 - LF_B) + D(1 - LF_D) + A(1 - LF_A)}{B + D + A} \tag{2}$$

where B, D, and A are the direct-beam, diffuse, and ground-reflected plane-of-array irradiance components, respectively, and LF_B, LF_D, and LF_A are the corresponding fractional AOI loss factors. The term $1 - LF$ therefore represents the transmitted fraction applied to each irradiance component. In this formulation, the modifier decreases when the weighted contribution of angular reflection losses increases, while a value close to one indicates that AOI-related losses are limited.

The Martin-Ruiz model defines the direct-beam loss factors as follows:

$$LF_B(\alpha) = \frac{exp(-cos\,\alpha / a_r) - exp(-1/a_r)}{1 - exp(-1/a_r)} \tag{3}$$

where α is the incidence angle of the direct-beam component in radians and a_r is the angular-loss coefficient, an empirical dimensionless parameter used in the Martin–Ruiz model to describe module angular-loss behavior. The loss factors for ground-reflected and sky-diffuse radiation are approximated as functions of the surface tilt angle β:

$$LF_A(\beta) \cong exp\left[-\frac{1}{a_r}\left(c_1\left(sin\beta + \frac{\beta - sin\beta}{1 - cos\beta}\right) + c_2\left(sin\beta + \frac{\beta - sin\beta}{1 - cos\beta}\right)^2\right)\right] \tag{4}$$

$$LF_D(\beta) \cong exp\left[-\frac{1}{a_r}\left(c_1\left(sin\beta + \frac{\pi - \beta - sin\beta}{1 + cos\beta}\right) + c_2\left(sin\beta + \frac{\pi - \beta - sin\beta}{1 + cos\beta}\right)^2\right)\right] \tag{5}$$

where c_1 and c_2 are empirical fitting parameters of the integrated diffuse and reflected-loss approximations. The same AOI modifier formulation was applied to all PV-active surfaces to avoid adding technology-specific optical assumptions. Following Martin and Ruiz [16], the angular-loss coefficient was set to $a_r = 0.17$, with $c_1 = \frac{4}{3\pi}$ and $c_2 = -0.069$. In the Martin–Ruiz model, a_r is an empirical coefficient that describes the angular-loss behavior of PV modules. The value of a_r = 0.17 was selected because Martin and Ruiz use it as a typical value for silicon PV modules when deriving the diffuse and ground-reflected angular-loss approximations. This value is close to their fitted coefficients for clean silicon modules, reported as (a_r = 0.169) for m-Si and (a_r = 0.163) for a-Si [16]. The use of one representative value for both technologies is also supported by Martin and Ruiz's finding that module technology has a second-order influence on angular response compared with the air/glass interface [16]. Therefore, a_r = 0.17 was applied to both the m-Si PVSD and a-Si STPV cases as a representative clean, unsoiled silicon-module coefficient.

2.2.2. Temperature-Loss Representation and Cell-Temperature Assessment

The temperature modifier accounts for changes in conversion efficiency when the operating cell temperature differs from the standard test conditions (STC) value of 25 °C. Its calculation requires a value for the PV cell temperature, which is treated differently for PVSD and STPV test cases because of their different envelope-integration conditions. Once the PV cell temperature is defined, the temperature modifier is evaluated in the same

way for both PVSD and STPV cases, following the traditional linear temperature-efficiency expression proposed by Evans and Florschuetz and reviewed by Dubey et al. [17]:

$$M_T(t) = 1 + \gamma_{\text{rel}}[T_c(t) - 25^\circ\text{C}] \tag{6}$$

where $M_T(t)$ is the temperature modifier, $T_c(t)$ is the PV cell temperature in °C, and γ_{rel} is the signed relative temperature coefficient expressed as a fractional value per °C. Therefore, temperature coefficients reported in %/°C are converted before use; for example, −0.4%/°C is entered as $-0.004\ ^\circ\text{C}^{-1}$. With this signed convention, a negative temperature coefficient reduces the temperature modifier when the operating cell temperature exceeds 25 °C, thereby lowering the resulting effective efficiency.

Technology-specific nominal efficiencies are defined in the comparative analysis design in Section 2.3, while the temperature modifier uses signed relative temperature coefficients of −0.4%/°C for m-Si and −0.2%/°C for a-Si. These coefficients are used as representative literature-supported values for the relative temperature dependence of PV conversion efficiency. For the m-Si PVSD cases, the selected coefficient is equivalent to −0.400%/K and lies within the monocrystalline silicon range reported by Martín-Chivelet et al. for ASHRAE/CEC-based PV technology data (−0.898 to −0.227%/K), close to the reported typical value of −0.453%/K [7]. For the a-Si STPV cases, the selected coefficient is equivalent to −0.200%/K. This value lies within the broader a-Si range of approximately 0.10–0.30%/°C reported for thin-film PV technologies by Ghosh [27], when expressed as a signed coefficient, and remains close to the a-Si range reported by Martín-Chivelet et al. for ASHRAE/CEC-based data (−0.351 to −0.215%/K) [7]. The stronger negative coefficient assigned to m-Si reflects the higher temperature sensitivity generally reported for crystalline silicon, while the lower-magnitude coefficient assigned to a-Si reflects the weaker temperature dependence commonly reported for amorphous silicon [17,27].

For PVSDs, the PV layer is treated as an opaque externally exposed PV surface. Cell temperature is therefore estimated using a simplified NOCT-based steady-state formulation, in which the temperature rise above ambient air temperature scales linearly with plane-of-array irradiance. This formulation is used because the modeled PVSD layer is exposed as an exterior PV element, not as a PV-active layer embedded within a glazing heat balance. The NOCT-based expression therefore provides a simplified operating-temperature estimate from outdoor air temperature, plane-of-array irradiance, and the selected NOCT value. This Ross-type NOCT expression is commonly used when only limited module-temperature parameters are available, although it does not explicitly resolve the wind-speed effects, mounting-specific heat transfer, or detailed thermal coupling [7,28]. The NOCT cell temperature was set to 45 °C as a representative manufacturer/datasheet-style value for rack-mounted commercial silicon PV modules. This value is supported by reported manufacturer and measured NOCT values for comparable rack-mounted silicon modules [29] and is consistent with Ross coefficients reported for free-standing crystalline-silicon modules [30]. The PV cell temperature is calculated as follows:

$$T_c = T_a + \frac{(NOCT - T_{\text{NOCT,ref}}) \cdot G_{\text{POA}}}{G_{\text{NOCT,ref}}} \tag{7}$$

where T_a is the outdoor dry bulb air temperature in °C and G_{POA} is the plane-of-array irradiance in W/m^2. The reference values are $T_{\text{NOCT,ref}}$ = 20 °C and $G_{\text{NOCT,ref}} = 800\ \text{W/m}^2$ [30].

For STPVs, two cell-temperature approaches are tested because the PV-active layer is embedded within the glazing assembly, as shown in Figure 3. In this paper, STPV laminate refers to the exterior-facing PV-active layer, while STPV glazing refers to the complete modeled double-glazing unit. The first approach is an adapted NOCT-based approach.

It retains the irradiance-dependent temperature term of Equation (7) but replaces the outdoor-air temperature input with the exterior surface temperature of the STPV laminate, obtained directly from the EnergyPlus simulation. The second approach, referred to as the heat-balance-based approach, instead assesses PV cell temperature from the mean temperature across the STPV laminate, using the simulated exterior surface temperature and a reconstructed inner-face temperature, as described below.

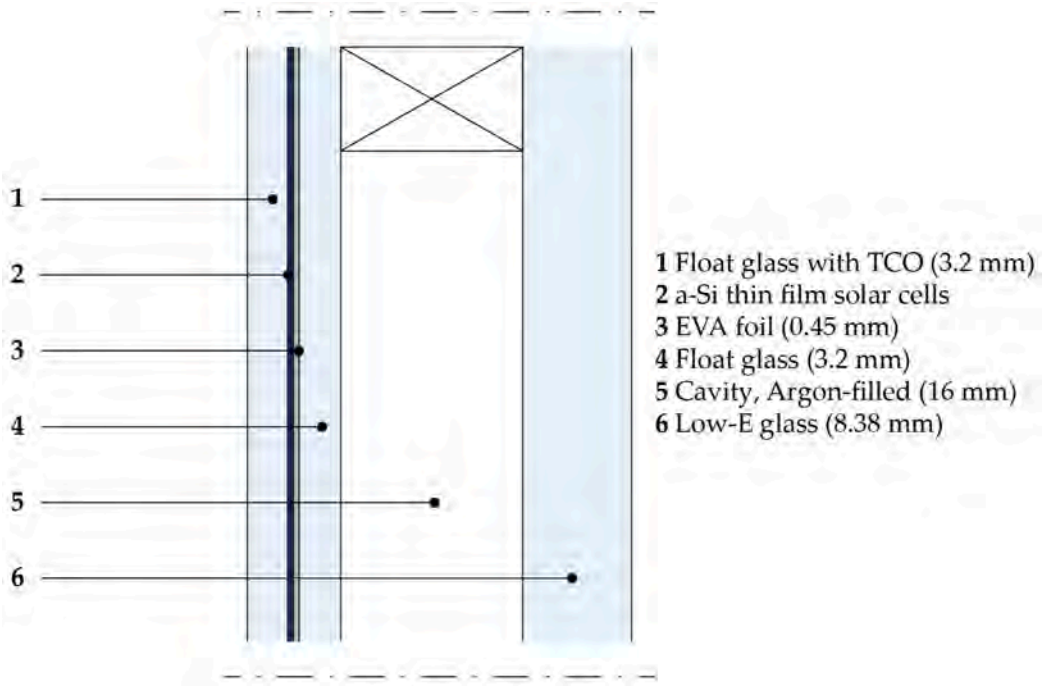

Figure 3. STPV glazing stratigraphy used for the modeling-choice analysis, with the STPV laminate as the exterior-facing layer of the double-glazing unit.

In the heat-balance-based approach, the STPV laminate is treated as the outer glazing layer of a double-glazing unit. This assumption is made for the sake of this work, but it could be extended to other insulated glazing configurations and other positions of the BIPV layer within the glazing system. The exterior surface temperature of this outer layer, θ_1, is available directly from the EnergyPlus simulation outputs. However, EnergyPlus does not report the adjacent glazing-face temperature at the inner side of the same laminate, θ_2, by default. This temperature is therefore reconstructed from the exterior-face glazing heat-balance equation reported in the EnergyPlus Engineering Reference [31]. Since EnergyPlus has already solved the heat balance during the simulation, the remaining terms in the equation are known output variables or defined material parameters, allowing the equation to be rearranged and solved for θ_2. The relevant EnergyPlus heat-balance variables and glazing surface temperatures are shown schematically in Figure 4.

For the outer layer of a double-glazing unit, the exterior-face heat-balance equation is defined as:

$$E_o\varepsilon_1 - \varepsilon_1\sigma\theta_1^4 + k_1(\theta_2 - \theta_1) + h_o(T_o - \theta_1) + S_1 = 0 \quad (8)$$

Solving Equation (8) for the adjacent surface temperature θ_2 gives:

$$\theta_2 = \theta_1 + \frac{-E_o\varepsilon_1 + \varepsilon_1\sigma\theta_1^4 - h_o(T_o - \theta_1) - S_1}{k_1} \quad (9)$$

Because the PV-active layer is embedded within the STPV laminate and is not represented as a separate thermal node, its cell temperature is approximated by the mean temperature across the outer glazing layer:

$$T_c = \frac{\theta_1 + \theta_2}{2} \tag{10}$$

This value should therefore be interpreted as a layer-averaged estimate of the embedded PV cell temperature, derived from the two boundary temperatures of the exterior STPV laminate.

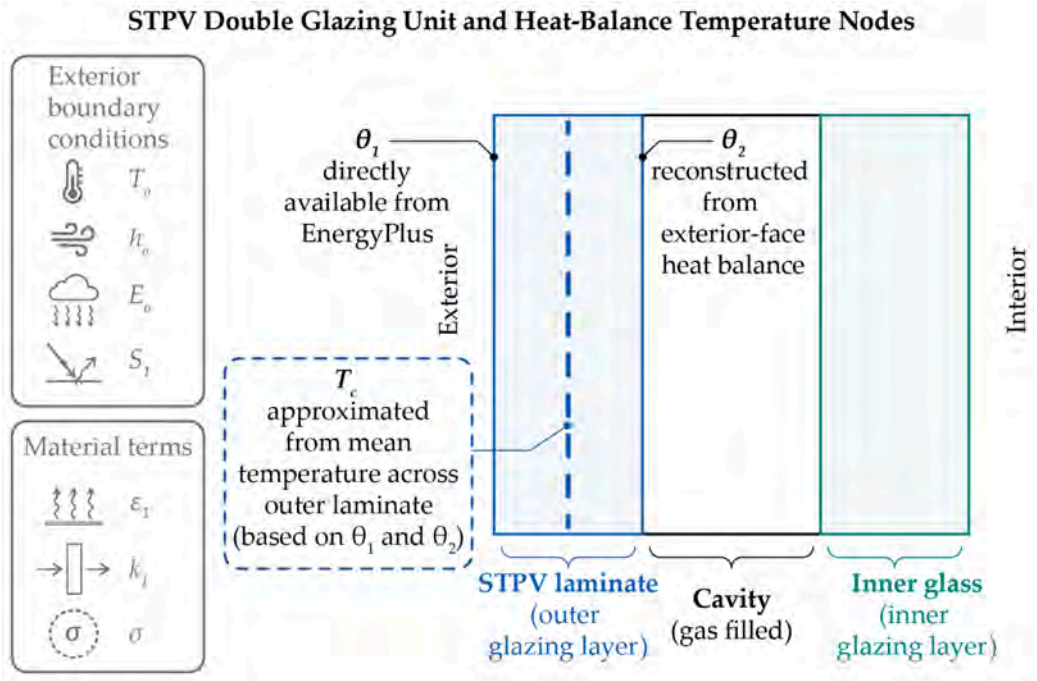

Figure 4. Heat-balance variables and temperature nodes used to reconstruct the inner-face temperature of the STPV outer glazing layer, redrawn by the authors based on the EnergyPlus engineering reference [31].

The reconstruction is algebraic at each simulation timestep: it uses the EnergyPlus window heat-balance variables available for that timestep to reconstruct the adjacent inner-face temperature of the exterior STPV laminate. It does not add a separate PV-active thermal node, PV-layer heat-capacity, or transient thermal response beyond the glazing thermal state represented by EnergyPlus. The optical and thermal layer properties used in the reconstruction remain fixed as defined in the STPV glazing construction. The EMS reconstruction uses glazing-layer heat-balance variables and does not separately solve frame-edge heat transfer.

In these equations, θ_1 denotes the exterior surface temperature of the STPV laminate and is obtained directly from EnergyPlus, while θ_2 is the reconstructed temperature at the inner face of the same laminate; both are expressed in K when used in the heat-balance equations. The terms h_o [W/m^{2}K], T_o [K], and S_1 [W/m^2] denote the exterior convective heat-transfer coefficient, outdoor air temperature, and absorbed radiation at the exterior surface, respectively. The parameters ε_1 [–], k_1 [W/m^{2}K], and σ [W/m^{2}K^4] denote the surface emissivity, conductance of the STPV laminate, and Stefan–Boltzmann constant. E_o [W/m^2] represents the outdoor longwave irradiation term used in the EnergyPlus exterior surface heat balance. The reconstructed cell temperature is converted to °C before it is used in the temperature modifier and before temperature results are reported.

The comparative evaluation of the two STPV temperature-assessment approaches is defined in Section 2.3.2.

As an implementation verification, the reconstructed θ_2 values were also compared with corresponding glazing-node temperatures calculated in WINDOW 8.1 under selected matched boundary conditions. This cross-software consistency analysis is reported in Appendix D and is used only to verify the numerical implementation of the reconstruction procedure, not as measured validation of the STPV cell-temperature model.

2.2.3. EnergyPlus EMS Implementation

The effective-efficiency calculation was executed with the EnergyPlus Energy Management System (EMS), which provides a framework for implementing user-defined control and modeling routines within EnergyPlus; further details on EMS syntax, sensors, actuators, calling points, and examples are provided in the EnergyPlus EMS Application Guide [32]. In this study, EMS was used as an intermediate calculation layer between the building-performance simulation outputs and the scheduled-efficiency input of the Simple PV model. Its role was to read the simulation variables needed for AOI and temperature correction, calculate the corresponding effective-efficiency value at each timestep, and export this value as an hourly schedule. Figure 5 summarizes this calculation sequence conceptually, and Appendix E reports the corresponding EMS/IDF pseudocode.

Because the EnergyPlus Simple model (SM) requires PV efficiency to be available before the PV yield calculation is executed, the effective-efficiency time series had to be generated first and then supplied to the model as an input schedule. The simulations were therefore executed through a two-run sequence. In the first run, EMS calculated the effective-efficiency time series from the simulated angle-of-incidence and cell-temperature values and exported it as an hourly schedule. In the second run, this schedule was imported into the Simple PV model and used as the efficiency input for PV electricity calculation, thereby forming the EnergyPlus modified Simple model (MSM) proposed in this study. Figure 6 summarizes this sequence, from EMS-based schedule generation to its use in the MSM. This workflow retains the original SM structure while replacing the fixed efficiency input with a time-dependent effective efficiency value.

The EMS implementation was chosen to keep the modifier calculation within the same simulation environment as the PV-yield calculation. In principle, however, the modifier calculation could also be executed externally to produce the schedule required for the PV-yield calculation.

2.3. Comparative Analysis Design

To evaluate the consistency and suitability of the proposed PV-yield model, a comparative analysis is conducted under controlled test conditions for the climatic context of Turin, Italy. Turin is used as the primary reference climate for the comparative analysis. It represents the main case-study context and a mid-latitude temperate European climate, with both heating- and cooling-relevant conditions and sufficient façade solar availability for PV-yield assessments. It was selected as the main reference climate because it provides an intermediate, non-extreme boundary condition for the full cross-tool comparison, rather than a predominantly cold or predominantly high-irradiance case. Because the two transparent-envelope BIPV system families addressed in this paper differ in construction, PV cell technology, and integration conditions, the evaluation is organized into two complementary analyses. The PVSD analysis tests how the proposed model behaves relative to external PV-yield tools and other EnergyPlus PV models as geometric detail and urban shading are added step by step. The STPV analysis follows a different sequence because the main uncertainty concerns the formulation of the STPV model itself. Alternative STPV

formulations are therefore tested within the proposed model before the selected configuration is compared with the other EnergyPlus PV models. The overall structure of this comparative analysis is summarized in Figure 7. Table 1 provides a compact overview of the modeled BIPV test cases, including the PV technology, orientations, angular variation, and main analysis assigned to each case.

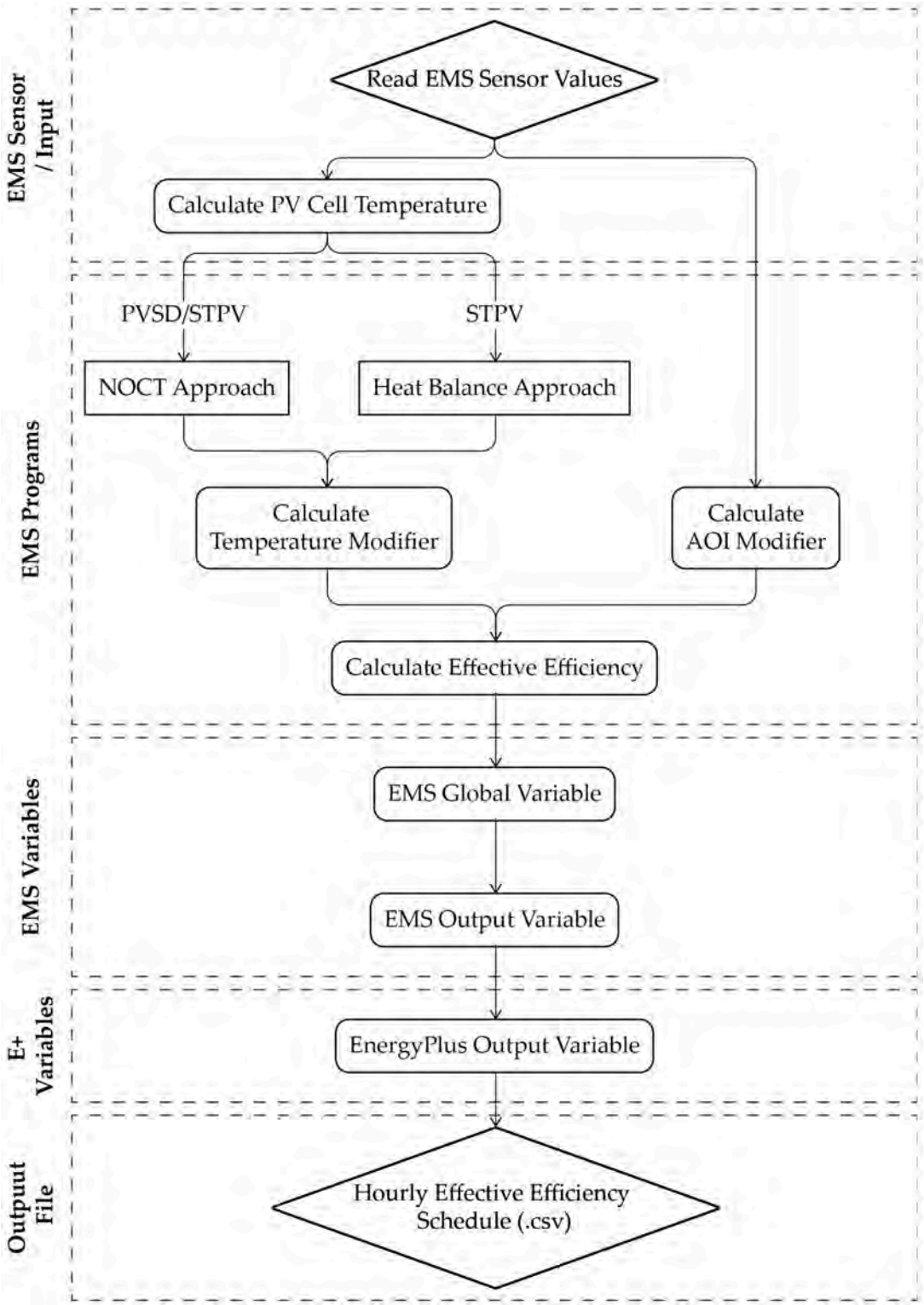

Figure 5. EnergyPlus EMS workflow for generating the hourly effective-efficiency schedule from AOI and temperature modifiers.

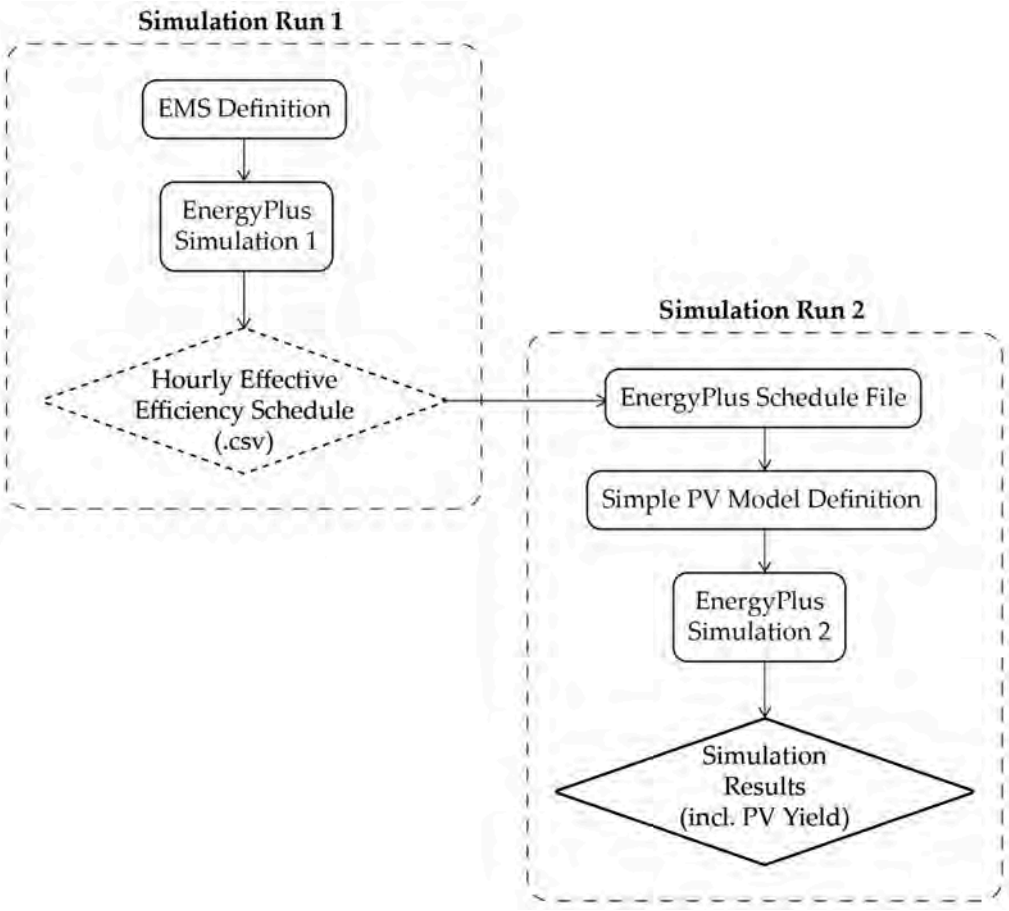

Figure 6. Two-run EnergyPlus sequence for generating the hourly effective-efficiency schedule and applying it in the Simple PV model.

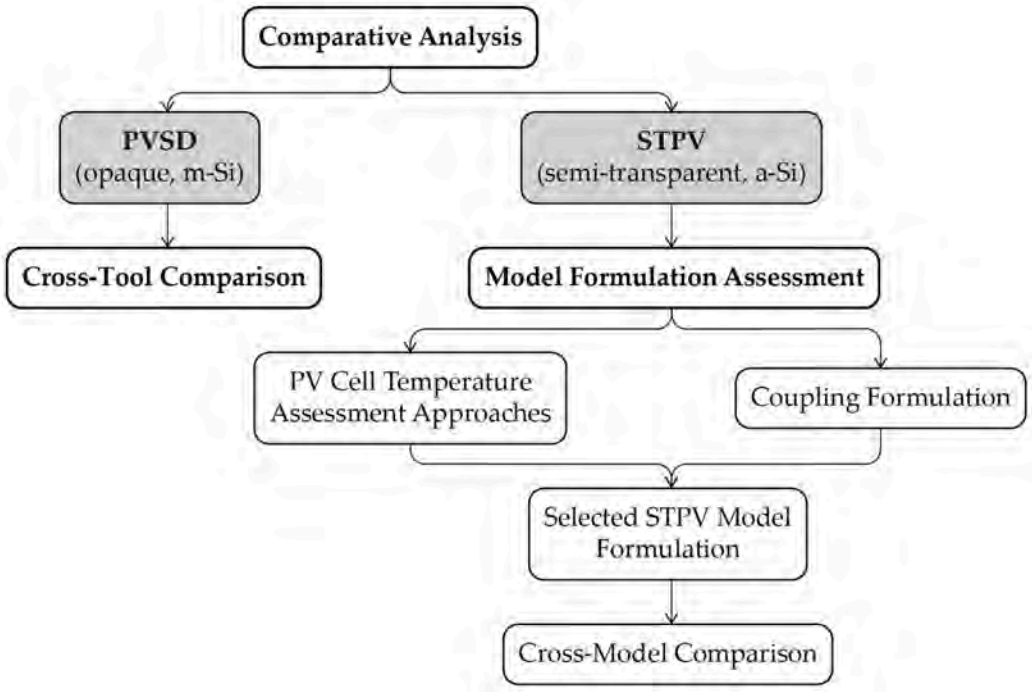

Figure 7. Schematic overview of the comparative analysis design for the PVSD cross-tool comparison and STPV model-formulation assessment.

Table 1. Overview of BIPV test cases used in the comparative analysis.

System Family	Modeled Case	PV Technology	Orientations	Angular Variation	Main Analysis
PVSD	Horizontal louvers	m-Si	East, South	Tilt: 0–90°, 15° increments	Cross-tool comparison across Levels 0–2
PVSD	Vertical louvers	m-Si	East, South	Rotation: −90° to +90°, 15° increments	Cross-tool comparison across Levels 0–2
STPV	Semi-transparent PV window	a-Si	East, South	Fixed vertical glazing	Modeling-choice and cross-model comparison

Together, the PVSD and STPV analyses assess whether the proposed model produces comparable annual yield levels and trends under controlled conditions, while also identifying the STPV formulation used for the subsequent EnergyPlus cross-model comparison.

Selected climate-transferability checks are also carried out for Trondheim and Malaga to test whether the relative model behavior observed for Turin changes under colder northern and warmer southern European boundary conditions. The full comparative analysis remains centered on Turin; the additional locations are used only for selected PVSD and STPV cases. Trondheim and Malaga were selected to bracket the Turin reference case. Trondheim represents a colder northern European, heating-relevant climate context, while Malaga represents a warmer southern European, cooling-relevant climate context.

The reference climate and the two additional climate-transferability locations are characterized using heating and cooling degree days and annual irradiation components. Their Köppen–Geiger classes, climate descriptions, and degree-day indicators are reported in Table 2.

Table 2. Climate classification and degree-day indicators for the reference climate and additional climate-transferability locations.

City	Country	Köppen–Geiger Climate Zone	Description	HDD [°C·d]	CDD [°C·d]	HDD STC Base [°C·d]	CDD STC Base [°C·d]
Trondheim	Norway	Dfc	Snow climate/fully humid, cool summer	2822.96	33.68	4710.80	47.71
Turin	Italy	Cfa	Warm temperate climate/fully humid, hot summer	1249.07	460.89	7347.40	0.69
Malaga	Spain	Csa	Warm temperate climate/summer dry, hot summer	109.88	867.67	2717.02	107.97

The degree-day values are calculated using base temperatures of 12 °C for heating and 18 °C for cooling. Additional degree-day values are calculated using a 25 °C base temperature, corresponding to the PV standard test condition temperature, to contextualize temperature-related differences between climates. The irradiation comparison includes direct normal irradiation (DNI), diffuse horizontal irradiation (DHI), and global horizontal irradiation (GHI), as shown in Figure 8.

Trondheim has the highest heating degree-day value and only limited cooling degree days, making it the strongest heating-relevant boundary condition in the selected set. Turin has both substantial heating and cooling degree-day values, supporting its role as the intermediate temperate reference case. Malaga has significantly lower heating and significantly higher cooling degree-day values than Turin, representing the warmest southern European boundary condition. The irradiation comparison shows a similar trend: Trondheim has much lower annual DNI and GHI, while Turin and Malaga have considerably higher direct and global irradiation. Malaga shows the highest DNI and GHI values, whereas DHI varies less strongly across the three climates. These comparisons provide the context for the selected climate-transferability analysis.

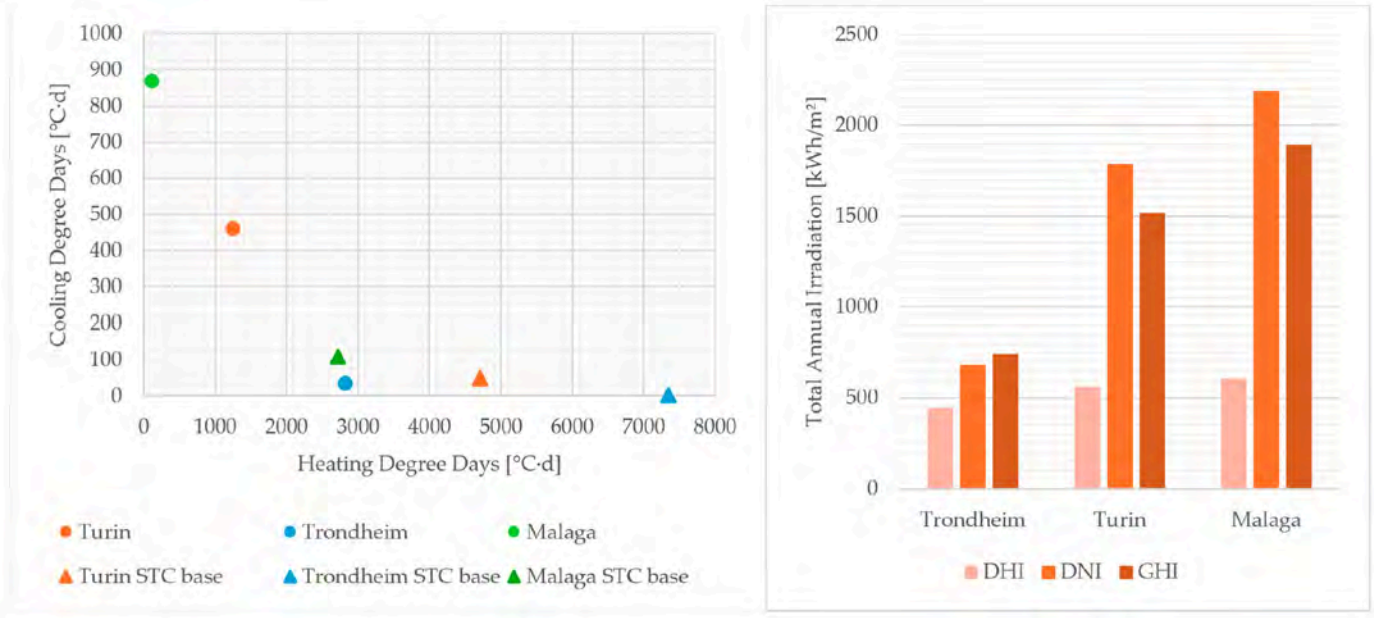

Figure 8. Degree-day and annual irradiation comparison for the reference climate and additional climate-transferability locations.

2.3.1. PVSD Cross-Tool Comparison Across Geometry Levels

The investigation of photovoltaic shading devices (PVSDs) uses horizontal and vertical louvers as controlled test-case typologies. These two typologies are used to evaluate model behavior under different geometric exposure and self-shading conditions while keeping the PV technology and yield-model assumptions fixed. The louvers are modeled as opaque monocrystalline silicon (m-Si) PV elements with an 18% nominal efficiency. This value is an early-stage m-Si assumption, and it lies within the monocrystalline silicon efficiency range reported by Martín-Chivelet et al. for ASHRAE/CEC-based PV technology data (0.084–0.221), supporting its plausibility for a controlled contemporary PVSD test case [7]. The proposed model is evaluated with the AOI-loss representation and NOCT-based cell-temperature assessment approach defined in the previous sections.

The simulations are conducted for South- and East-facing façades. This reduced orientation set was selected to keep the test-case matrix manageable while retaining two contrasting solar-exposure conditions. South represents a high-exposure façade condition in the investigated northern-hemisphere climate, while East provides a lateral façade case with morning-dominated irradiation and different incidence-angle behavior. North is excluded because of its limited relevance for PV electricity generation in the investigated climatic context of Turin. West is not evaluated separately; instead, East is used as the selected lateral orientation because East and West are expected to provide broadly comparable annual exposure levels under the same unobstructed climate conditions.

To isolate the influence of geometric and contextual shading complexity on annual PV yield, the PVSD typologies are examined across three levels of increasing complexity. Level 0 establishes an unshaded reference using a 1.0 m^2 PV surface evaluated for a defined set of tilt and rotation angles at 15° increments. The 15° increment provides a regular sampling of tilt- and rotation-dependent PV-yield behavior. This level isolates the effects of orientation and AOI-related reflection without geometric shading. Level 1 introduces explicit louver geometry, with a 0.3 m slat depth and 0.5 m spacing, corresponding to a depth-to-spacing ratio of 0.6. This controlled geometry was selected to introduce mutual self-shading between louver elements while avoiding an overly dense louver arrangement. The ratio is also consistent with PVSD optimization work identifying the width-to-spacing ratio as a relevant design variable and reporting favorable values around 0.6–1.0 [33]. The

geometry is used as a comparison setup, not as an optimized louver design. Level 2 places the PVSD configurations on an office-building archetype within an urban context composed of eight surrounding buildings at a distance of 15 m. This level assesses the combined influence of louver geometry and external urban obstructions.

The PV-surface tilt and rotation angles reported across the comparison levels follow the PVGIS convention. For horizontal louvers, tilt ranges from 0° for an upward-facing surface to 90° for a vertical surface. For vertical louvers, rotation is referenced to South, with 0° representing South, −90° representing East, and +90° representing West. These angle conventions are illustrated in Figure 9.

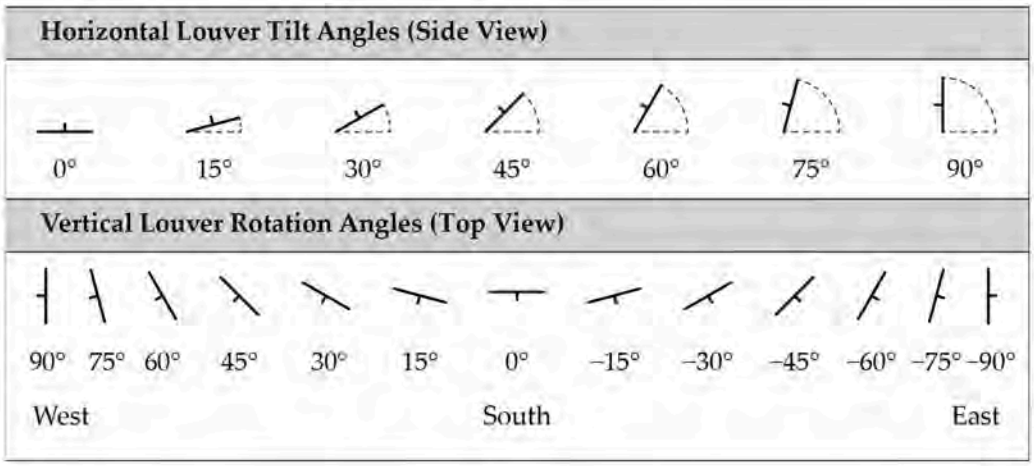

Figure 9. PVGIS-based angle conventions used to report PVSD configurations: horizontal louver tilt angles in side view and vertical louver rotation angles in top view.

The proposed model is benchmarked against four PV-yield assessment approaches. These include two external tool-based approaches, PVGIS Version 5.3 [34] and Ladybug Tools (LBT version 1.9.0) [35], and two alternative EnergyPlus PV models, the fixed-efficiency Simple model (SM) and the Equivalent One-Diode model (EODM). The same TMY weather file exported from PVGIS (PVGIS-SARAH3: 2005-2023) is used in all cases to ensure consistent climatic input. The comparison-relevant differences between these approaches are described below in terms of the geometry representation, irradiance assessment, and PV-yield calculation.

The approaches differ mainly in how they represent geometry and convert solar input into PV yield. LBT, SM, the proposed model, and EODM are geometry-based workflows. For these approaches, the PV input geometry is generated parametrically in Grasshopper, keeping PV surface areas, orientations, tilt angles, and shading configurations consistent across the corresponding simulations. PVGIS is included as an external reference approach, but its standard workflow does not explicitly represent the three-dimensional louver geometry or surrounding urban context used in the Grasshopper-based simulations. It is therefore evaluated only for Level 0 and retained as an unshaded external reference for the higher geometry levels. The resulting cross-tool differences combine PV-conversion assumptions with tool-specific irradiance and shading representation. This is especially relevant at Levels 1 and 2, where the EnergyPlus- and Ladybug-based simulations include self-shading and urban-context shading that are not represented by the PVGIS reference calculation.

Within the geometry-based workflows, LBT represents the PV surfaces explicitly and calculates incident radiation on a 10 × 10 cm spatial grid; annual yield is then derived from monthly radiation totals using a fixed-efficiency assumption and a 15% system derate factor. The SM serves as the fixed-efficiency EnergyPlus baseline. Since the SM and the

proposed model use the same EnergyPlus geometry and irradiance basis, their direct comparison isolates the effect of replacing fixed efficiency with the time-dependent AOI and temperature modifiers introduced in the proposed model. The EODM provides a more detailed EnergyPlus electrical-model reference, but it is evaluated only at Level 0. This restriction avoids introducing additional uncertainty from adapting the required electrical input parameters to the different PV areas and geometries used at Levels 1 and 2.

The complete PVSD cross-tool comparison setup, including the tools, models, and geometry representations assigned to each level, is summarized in Figure 10.

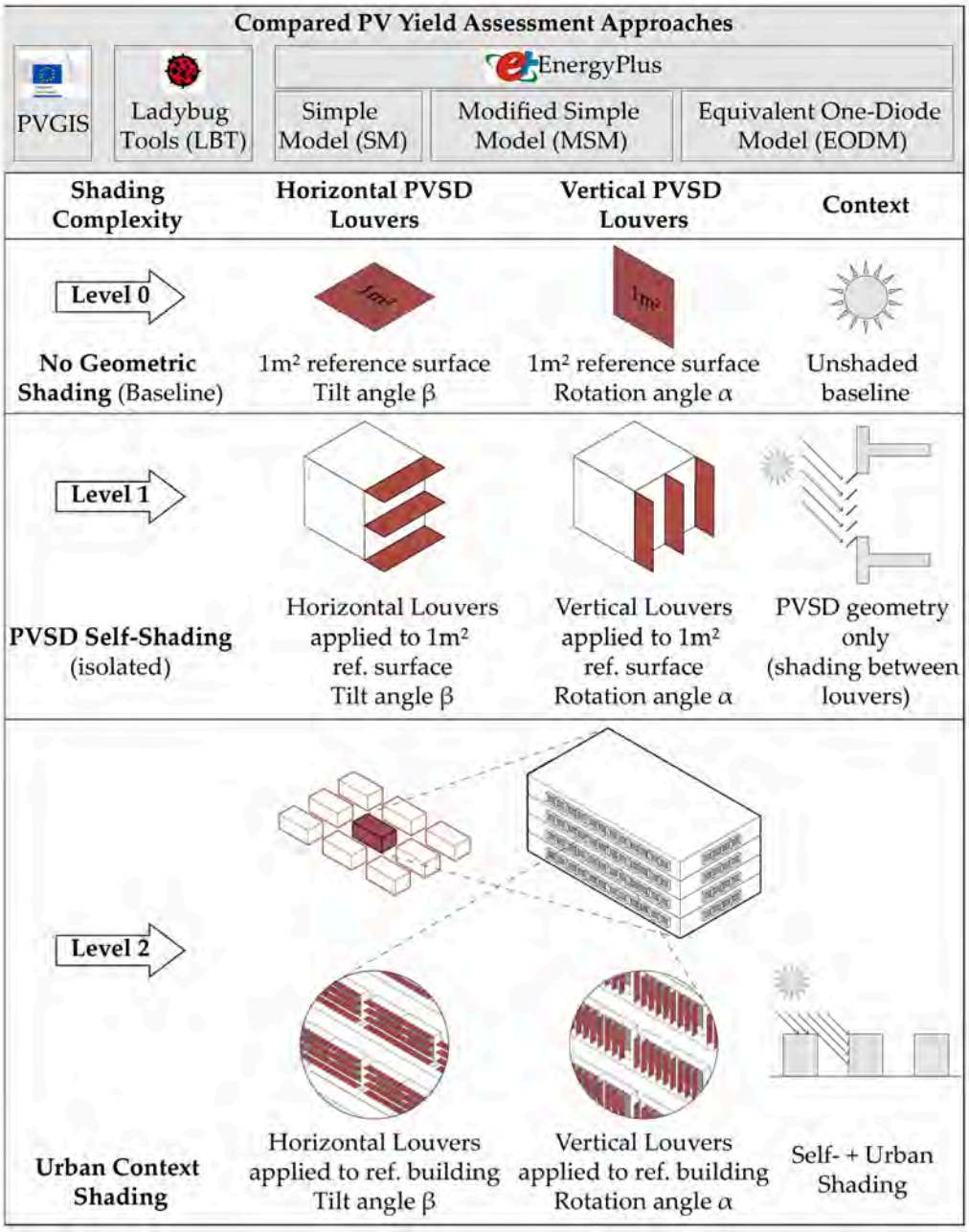

Figure 10. PVSD cross-tool comparison setup across geometry levels and assessment approaches.

In addition to the full Turin-based PVSD comparison, a selected additional climate-transferability check is performed at Level 0 for Trondheim and Malaga. This extension is limited to Level 0 because this level isolates model differences before explicit louver self-shading or urban-context shading is introduced. Four PVSD configurations are selected for this check: horizontal louvers facing East with a 90° tilt, horizontal louvers facing South

with a 60° tilt, vertical louvers facing East with a −90° rotation angle, and vertical louvers facing South with a −90° rotation angle. These cases were selected because the Turin Level 0 comparison shows relatively large deviations between MSM and at least one benchmark approach, especially PVGIS.

2.3.2. STPV Modeling-Choice Analysis and Cross-Model Comparison

The STPV investigation models the window as part of the exterior envelope of a room-scale building-performance simulation model. The modeled STPV window is a double-glazing unit in which the STPV laminate forms the exterior-facing glazing layer, as introduced in Figure 3. Following the terminology introduced in Section 2.2.2, the STPV laminate is the exterior-facing PV-active layer, while the STPV glazing is the complete modeled double-glazing unit.

This room-scale setup allows PV yield to be assessed while accounting for the role of the STPV glazing as a building element. Because the STPV laminate is integrated within the window assembly, its thermal state depends on the window heat balance and on both outdoor and indoor boundary conditions. These boundary conditions affect glazing temperature, which is then used to determine PV cell temperature and PV yield. The STPV glazing construction introduced in Figure 3 is applied to the room-scale setup shown in Figure 11.

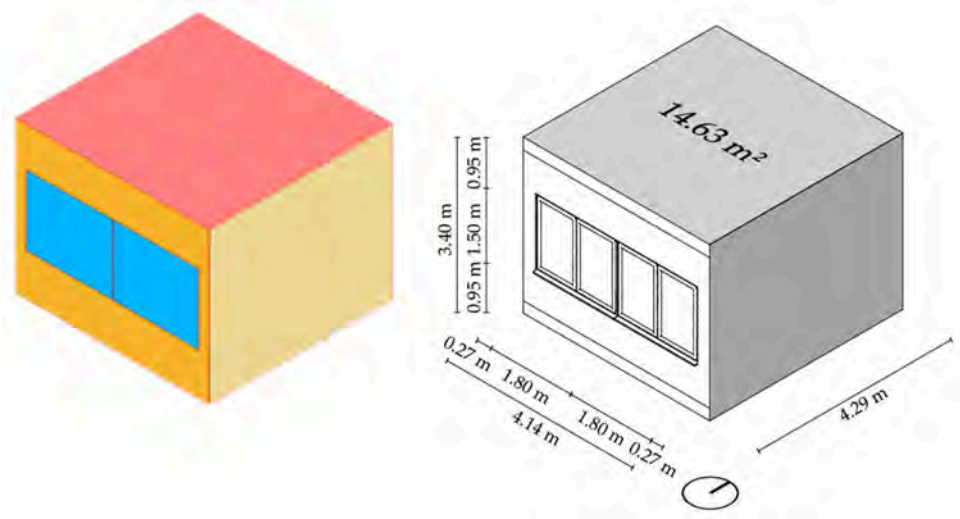

Figure 11. Room-scale simulation geometry used for the STPV modeling-choice analysis and cross-model comparison.

The test case is evaluated for South and East orientations using an office room extracted from the same Italian office-building archetype used for the Level 2 PVSD cross-tool comparison. The same orientations are used here to keep the PVSD and STPV comparisons aligned across the high-exposure South case and the lateral East case. All room boundaries are modeled as adiabatic except for the external wall containing the window, so that heat exchange through the room envelope is limited to the façade condition under investigation. Occupancy, internal loads, schedules, and HVAC settings are reported in Appendix A, Table A1. The main envelope parameters are summarized in Table 3. The visible transmittance value reported for the window refers to the complete modeled STPV glazing unit. This differs from the visible transmittance of the STPV laminate itself, which is reported separately in Table 4.

Table 3. Envelope parameters used for the STPV modeling-choice analysis and cross-model comparison.

Envelope Component	Parameter	Unit	Value
External Wall	U-Value	W/m^2K	0.15
Window	U-Value	W/m^2K	1.41
	SHGC	-	0.26
	T_{vis}	-	0.32

The STPV laminate is parameterized to represent an amorphous silicon (a-Si) PV cell technology. The a-Si case was selected as a lower-efficiency thin-film STPV counterpart to the opaque monocrystalline-silicon PVSD cases, allowing the proposed model to be tested across two different PV technology families. The a-Si laminate represents one established semi-transparent BIPV glazing technology, with reported use in window, façade, double-skin façade, and mock-up building-envelope applications [24,36–38]. It is used here as a lower-efficiency thin-film STPV case, not as a representation of all STPV technologies. The representation in this study uses a nominal efficiency of 3.6% and a laminate visible transmittance of 36%, based on the dataset reported in [39]. The dataset is based on experimentally characterized commercial semi-transparent a-Si PV laminates for building integration, providing the optical and electrical input basis used in the modeled glazing construction. The efficiency value is derived from the opaque a-Si reference case with 6% efficiency by assuming a linear relationship between visible transmittance and efficiency. The complete glazing-layer properties are reported in Table 4. Other STPV technologies, such as CdTe, organic PVs, dye-sensitized PVs, or perovskite-based glazing, would require their own optical, electrical, and thermal parameter sets and are outside the controlled test-case scope of this comparison.

Table 4. Layer properties and data sources used to define the STPV glazing construction.

Layer	d [mm]	λ [W/mK]	τ	ρ_{front}	ρ_{back}	ε_{front}	ε_{back}	Ref.
STPV laminate	6.85	0.67	0.3 (0.36)	0.11 (0.08)	0.11 (0.31)	0.84	0.84	[39]
Argon	16.00	-	-	-	-	-	-	-
Low-E Glass	8.38	0.85	0.59 (0.89)	0.3 (0.04)	0.21 (0.05)	0.05	0.85	WINDOW 8.1 Database [40]

Note: d = thickness; λ = thermal conductivity; τ = solar transmittance; ρ = solar reflectance; ε = emissivity. Subscripts "front" and "back" refer to the exterior- and interior-facing sides of each layer, respectively. Values in parentheses indicate visible optical properties, where applicable.

The STPV analysis first compares the tested cell-temperature approaches and coupling formulations within the proposed model. This step evaluates the influence of each tested combination on the calculated PV cell temperature, effective efficiency, and annual PV yield. The resulting comparison is used to select one combination as the proposed model configuration for the second step. This configuration is then compared with the fixed-efficiency Simple model (SM) and the Equivalent One-Diode model (EODM) in an internal EnergyPlus cross-model comparison. The EODM input parameters are adapted to the a-Si STPV laminate and reported in Appendix B.2, Table A3.

After the Turin-based STPV modeling-choice and cross-model comparison, an additional STPV cross-model climate comparison is carried out for the selected heat-balance-based decoupled MSM configuration, SM, and EODM. This comparison is evaluated for East and South orientations in Turin, Trondheim, and Malaga.

The modeling-choice analysis is structured as a two-by-two matrix as shown in Table 5. One matrix dimension is the PV cell-temperature assessment approach, and the other is the coupling formulation. Each cell-temperature assessment approach is evaluated under

both coupling formulations, resulting in four tested combinations. The matrix separates the effect of the temperature basis from the effect of the coupling formulation, while also testing their combined effect. To avoid ambiguity, "window heat-balance calculation" refers here to the EnergyPlus thermal solution of the complete STPV glazing system. "Heat-balance-based approach" refers specifically to the cell-temperature assessment approach that derives PV cell temperature from simulated glazing-temperature outputs.

Table 5. STPV modeling-choice analysis matrix.

PV Cell Temperature Assessment Approach /Coupling Formulation	Decoupled Formulation	Coupled Formulation
Adapted NOCT-based approach	NOCT + decoupled	NOCT + coupled
Heat-balance-based approach	Heat-balance + decoupled	Heat-balance + coupled

The first matrix dimension is PV cell-temperature assessment. As defined in Section 2.2.2, two approaches are compared within the proposed model for the STPV application. The adapted NOCT-based approach applies an irradiance-dependent temperature correction to a glazing-related temperature basis, while the heat-balance-based approach calculates PV cell temperature from simulated glazing-temperature outputs. These two approaches test how the selected temperature basis for the STPV laminate affects the calculated PV cell temperature, effective efficiency, and annual PV yield.

The second matrix dimension is the coupling formulation. Two formulations are tested: a decoupled formulation and a coupled formulation. Coupling describes how the calculated effective efficiency is linked to subsequent simulation steps. After the PV cell temperature is calculated using the selected cell-temperature assessment approach, the resulting effective efficiency is either used only in the PV-yield calculation or also represented in the subsequent window heat-balance calculation.

In the decoupled formulation, EnergyPlus solves the window heat balance using the fixed solar-optical properties assigned to the STPV glazing construction. The resulting glazing-temperature outputs are then used to calculate the PV cell temperature, effective efficiency, and PV yield according to the selected cell-temperature assessment approach. The calculated effective efficiency is applied only in the PV-yield calculation and is not fed back into the subsequent window heat-balance calculation. This formulation represents a one-directional workflow from the simulated glazing thermal state to PV-yield calculation, with the window heat-balance calculation based on the fixed solar-optical properties of the glazing construction.

In the coupled formulation, the calculated effective efficiency is also represented in the subsequent window heat-balance calculation. This is done through a solar-optical correction that approximates the physical effect of PV electricity conversion on the glazing heat balance: the fraction of incident solar radiation converted into electricity is not retained as heat in the STPV laminate and therefore reduces the effective absorbed solar fraction.

The solar-optical correction is based on the optical balance of the glazing layer, where incident solar radiation is divided into transmitted, absorbed, and reflected fractions:

$$\tau + \alpha + \rho = 1 \tag{11}$$

where τ is solar transmittance, α is solar absorptance, and ρ is solar reflectance. Rearranging Equation (11) gives the following:

$$\alpha = 1 - \tau - \rho \tag{12}$$

Ideally, the electricity-converted fraction would be subtracted directly from the solar absorptance. However, EnergyPlus does not allow solar absorptance to be modified directly as an independent input for simulation. The correction is therefore applied indirectly through the solar-optical properties. To preserve the daylight and indoor solar-gain behavior of the STPV glazing, solar transmittance is kept constant. The timestep-specific effective efficiency is instead added to solar reflectance, following previous STPV modeling approaches [18,19,41]. Through Equation (12), this increase in reflectance reduces the remaining absorbed fraction.

EMS implements this coupled formulation by switching between predefined glazing constructions with different solar-reflectance values according to the calculated effective efficiency. The updated solar-optical state is then used in the subsequent window heat-balance calculation. This creates a sequential feedback loop: glazing temperature affects the effective efficiency, effective efficiency adjusts solar reflectance, and the adjusted reflectance affects the next heat-balance solution. The EMS-based construction-switching logic is summarized in Figure 12. The coupling remains approximate because the updated solar-optical state is applied sequentially and is not re-converged within the same timestep.

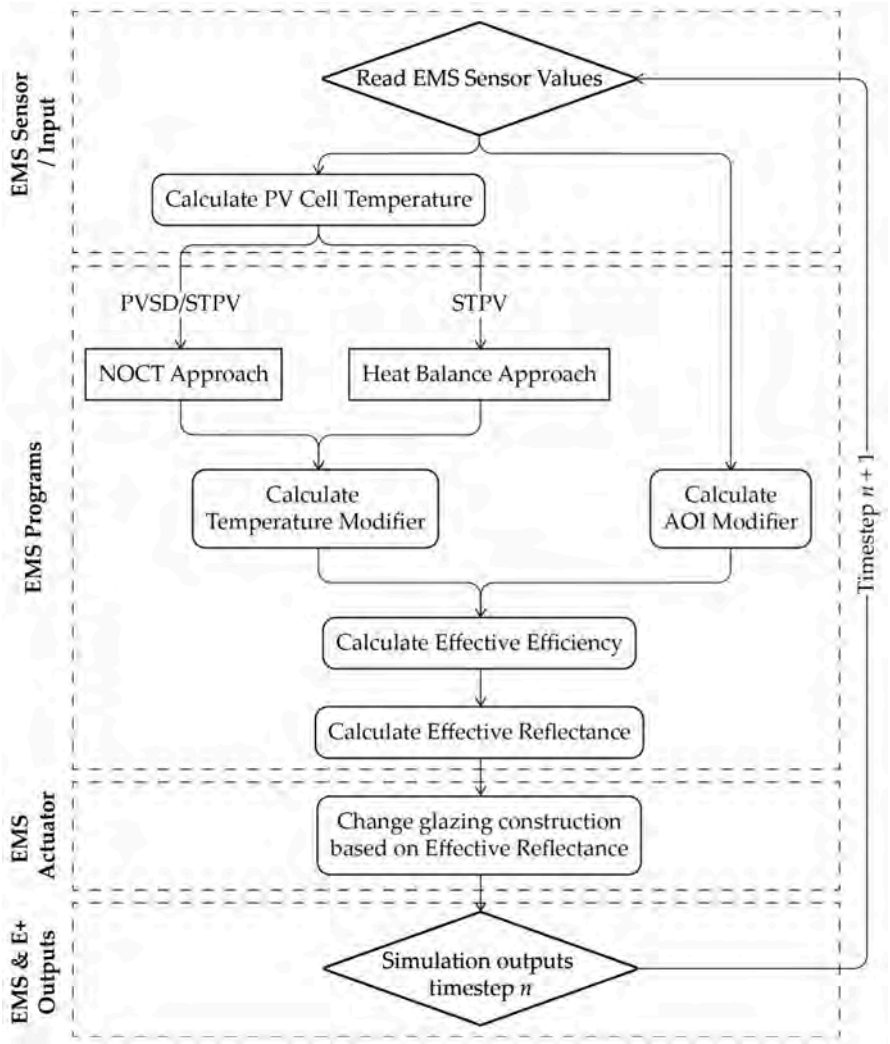

Figure 12. EnergyPlus EMS scheme for the STPV coupled formulation with effective-efficiency-based construction switching.

2.4. KPIs and Post-Processing

This section defines the key performance indicators (KPIs) used in the PVSD and STPV comparisons and describes how simulation outputs are post-processed into an-

nual comparison metrics. The annual PV yield is the main KPI for both system families. For STPVs, the PV cell temperature and effective efficiency are also extracted to evaluate the effects of the alternative temperature-assessment and coupling formulations. Table 6 summarizes the KPIs and diagnostic output indicators used in the comparisons before their calculation and normalization procedures are described.

Table 6. Key performance indicators and diagnostic output indicators used in the PVSD and STPV comparisons.

KPI	Symbol	Unit	BIPV System Family	Role
Annual PV Yield	Y_{PV}	kWh/m^2·y	PVSD, STPV	Primary KPI for comparing annual electricity generation per full integrated BIPV element area.
Absolute PV Yield Deviation	ΔY_{PV}	kWh/m^2·y	PVSD, STPV	Difference between a compared model/tool and the proposed model or selected proposed-model configuration.
Relative PV Yield Deviation	δY_{PV}	%	PVSD, STPV	Normalized difference in annual PV yield relative to the proposed model or selected proposed-model configuration.
Geometry-Level Yield Reduction	$R_{i\to j}$	%	PVSD	Relative reduction in annual PV yield between geometry levels.
Median PV Cell Temperature	$\tilde{T}_c$	°C	STPV	Diagnostic indicator for comparing temperature-assessment formulations during sunlit hours.
Median Effective Efficiency	$\tilde{\eta}_{eff}$	%	STPV	Diagnostic indicator for comparing effective PV conversion efficiency during sunlit hours.

The KPIs used in the analysis are defined as numerical annual or annual-summary quantities, with explicit symbols, units, and normalization bases. The main KPI is the annual PV yield, Y_{PV} [kWh/m^2·y], which represents the annual PV electricity generation normalized by the system-specific reporting area. For PVSDs, the reporting area is the full louver surface area, A_{louver} [m^2]. For STPVs, the reporting area is the total STPV glazing area, A_{STPV} [m^2]. In both cases, the reporting area refers to the full building-integrated element area, not only to the active PV cell area. The active-area fraction is therefore applied to the electricity-generation calculation before area normalization, while the denominator remains the full louver surface area for PVSDs and the total STPV glazing area for STPVs.

The annual PV yield is calculated from the PV-yield outputs available from each workflow. For PVGIS and Ladybug Tools, the outputs used in this comparison are monthly PV-yield values, which are aggregated to annual totals. For the EnergyPlus-based workflows, PV-yield outputs are exported as hourly time series and summed over the annual simulation period. These post-processing steps follow the temporal resolution of the available outputs. Separately from this output aggregation, the underlying computational temporal resolution differs between the workflows. PVGIS and Ladybug Tools calculate PV yield at an hourly resolution, whereas the EnergyPlus-based workflows calculate the PV yield at the sub-hourly simulation timestep. The active-area fraction, $f_{\mathrm{act}} = 0.9$, is applied consistently across the compared workflows, either within the simulation model or during post-processing, depending on the tool output structure. Where the correction is applied during post-processing, the active-area-corrected electricity output is calculated as follows:

$$E_{PV,act} = E_{PV,raw} \cdot f_{act} \tag{13}$$

where $E_{\mathrm{PV,raw}}$ [kWh] is the PV electricity output before active-area correction, and $E_{\mathrm{PV,act}}$ [kWh] is the corresponding electricity output after applying the active-area fraction. This correction is applied at the temporal resolution of the respective tool output. If the active-area fraction is already included in the simulation model or tool setup, $E_{\mathrm{PV,act}}(t)$ corresponds directly to the exported PV electricity output.

For hourly outputs, the annual PV yield is calculated as follows:

$$Y_{PV} = \frac{\sum_{t=1}^{8760} E_{PV}, act(t)}{A_{rep}} \quad (14)$$

where $E_{\mathrm{PV,act}}(t)$ [kWh] is the PV electricity generated during hour t, and A_{rep} [m^2] is the reporting area. For PVSDs, $A_{\mathrm{rep}} = A_{\mathrm{louver}}$. For STPVs, $A_{\mathrm{rep}} = A_{\mathrm{STPV}}$. For monthly tool outputs, the same KPI is calculated as follows:

$$Y_{PV} = \frac{\sum_{m=1}^{12} E_{PV,act,m}}{A_{rep}} \quad (15)$$

where $E_{\mathrm{PV,act},m}$ [kWh] is the PV electricity generated in month m. This convention ensures that the reported PV yield expresses the electricity contribution per full integrated BIPV element area, while still accounting for the assumed active-area fraction of 0.9 in the electricity-generation calculation.

A 15% system derate/loss factor is applied consistently across all workflows to account for system-level losses that are not modeled explicitly, including wiring, residual mismatch effects, inverter-related losses, soiling, availability, and degradation. The selected value, f_{derate} = 0.85, is close to the 14% aggregate system-loss default or recommendation used in common PV-yield workflows such as PVGIS and PVWatts/PVLib [42,43], and is also consistent with PV tool-comparison work that applies a uniform 14% system-loss assumption across simulations [44].

This aggregation follows the loss-factor logic described by Chivelet et al., where BIPV performance is reduced by several distinct loss terms, including soiling, wiring, inverter or power-electronics losses, and other component inefficiencies [45]. In this study, AOI-related optical losses, temperature effects, and geometric shading are treated separately. The derate factor therefore represents remaining non-module system losses that are not resolved individually. It does not represent detailed electrical layout, stringing, or nonlinear mismatch losses under non-uniform PVSD irradiance.

In PVGIS, this loss factor is specified directly in the tool settings. For all other workflows, the same assumption is applied during post-processing. Because the active-area correction is already included in Y_{PV}, but the system derate is not, the derated annual PV yield is calculated as follows:

$$Y_{PV,derated} = Y_{PV} \cdot f_{derate} \quad (16)$$

with $f_{\mathrm{derate}} = 0.85$. Unless stated otherwise, the reported annual PV-yield values refer to the derated yield. Appendix B.1 reports the common PV-yield input parameters used in the MSM and post-processing, while Appendix B.2 reports the additional EODM-specific input parameters.

2.4.1. PVSD

Following the normalization convention defined above, PVSD yield is reported per full louver surface area, A_{louver} [m^2], while the active-area fraction is included in the electricity output.

The main PVSD KPI is annual PV yield, $Y_{\mathrm{PV,PVSD}}$ [kWh/m^2·y], defined as

$$Y_{PV,PVSD} = \frac{E_{PV,PVSD,act,ann}}{A_{louver}} \quad (17)$$

where $E_{\mathrm{PV,PVSD,act,ann}}$ [kWh/y] is the annual active-area-corrected PV electricity output obtained from the respective tool output after hourly or monthly aggregation, and A_{louver} [m^2] is the full louver surface area.

Deviations are calculated with respect to the proposed model. Absolute deviations are defined as the arithmetic difference between each compared approach and the proposed model. The absolute PV-yield deviation, ΔY_{PV} [kWh/m^2·y], is calculated as follows:

$$\Delta Y_{PV} = Y_{PV,m} - Y_{PV,MSM} \tag{18}$$

where $Y_{\mathrm{PV},m}$ [kWh/m^2·y] is the annual PV yield of the compared model or tool, and $Y_{\mathrm{PV,MSM}}$ [kWh/m^2·y] is the annual PV yield of the proposed model.

Relative deviations are calculated by normalizing this difference by the corresponding annual PV yield of the proposed model. The relative PV-yield deviation, δY_{PV} [%], is calculated as follows:

$$\delta Y_{PV,m} = \frac{Y_{PV,m} - Y_{PV,MSM}}{Y_{PV,MSM}} \cdot 100 \tag{19}$$

A positive value of $\delta Y_{\mathrm{PV},m}$ indicates that the compared model or tool gives a higher annual PV yield than the proposed model, while a negative value indicates a lower annual PV yield.

For the direct comparison between the fixed-efficiency EnergyPlus Simple model (SM) and the proposed model, the same deviation calculation is used to quantify the yield effect of the time-dependent AOI and temperature modifiers.

For the geometry-level comparison, annual PV-yield reductions are calculated using the proposed model for the transitions from Level 0 to Level 1, from Level 1 to Level 2, and from Level 0 to Level 2. Each reduction is normalized by the annual PV yield of the first level in the respective comparison. The geometry-level yield reduction, $R_{i\to j}$ [%], is calculated as follows:

$$R_{i\to j} = \frac{Y_{PV,i} - Y_{PV,j}}{Y_{PV,i}} \cdot 100 \tag{20}$$

where $Y_{\mathrm{PV},i}$ [kWh/m^2·y] is the annual PV yield at the initial geometry level, and $Y_{\mathrm{PV},j}$ [kWh/m^2·y] is the annual PV yield at the subsequent geometry level. The geometry-level reductions are therefore normalized by the yield of the starting level in each comparison.

2.4.2. STPVs

For the STPV comparison, the reported KPIs are the annual PV yield, $Y_{\mathrm{PV,STPV}}$ [kWh/m^2·y]; annual median PV cell temperature, $\widetilde{T}_{\mathrm{c}}$ [°C]; minimum and maximum PV cell temperature, $T_{\mathrm{c,min}}$ and $T_{\mathrm{c,max}}$ [°C]; and annual median effective efficiency, $\widetilde{\eta}_{\mathrm{eff}}$ [%].

The PV cell temperature and effective efficiency are obtained from EMS-exported hourly time series. Annual median values are calculated only for hours with incident solar radiation on the STPV window. This set of hours is defined as H_{sunlit}. The median PV cell temperature is calculated as follows:

$$\widetilde{T}_c = \mathrm{median}(T_c(t)), \;\; t \in \; H_{sunlit} \tag{21}$$

where $T_{\mathrm{c}}(t)$ [°C] is the hourly PV cell temperature. The minimum and maximum PV cell temperatures are calculated from the same filtered dataset:

$$T_{c,min} = \min(T_c(t)), \;\; t \in \; H_{sunlit} \tag{22}$$

$$T_{c,max} = \max(T_c(t)), \;\; t \in \; H_{sunlit} \tag{23}$$

The median effective efficiency is calculated as follows:

$$\widetilde{\eta}_{eff} = \text{median}\Big(\eta_{eff}(t)\Big), \;\; t \in \; H_{sunlit} \tag{24}$$

where $\eta_{\text{eff}}(t)$ [%] is the hourly effective PV conversion efficiency.

The same sunlit-hour filter is applied to the exterior glazing temperature, which is extracted as a reference variable because the STPV laminate is located in the exterior-facing glazing layer. The median exterior glazing temperature, $\widetilde{T}_{\text{g,ext}}$ [°C], is calculated as follows:

$$\widetilde{T}_{g,ext} = \text{median}\big(T_{g,ext}(t)\big), \;\; t \in \; H_{sunlit} \tag{25}$$

where $T_{\text{g,ext}}(t)$ [°C] is the hourly exterior glazing temperature.

Following the same normalization convention, annual STPV yield is calculated from the hourly EnergyPlus output and normalized by the total STPV glazing area, A_{STPV}. The annual STPV yield, $Y_{\text{PV,STPV}}$ [kWh/m^2·y], is calculated as

$$Y_{PV,STPV} = \frac{E_{PV,STPV,act,ann}}{A_{STPV}} \tag{26}$$

where $E_{\text{PV,STPV,act,ann}}$ [kWh/y] is the annual active-area-corrected PV electricity output after hourly aggregation, and A_{STPV} [m^2] is the total STPV glazing area.

In the internal EnergyPlus cross-model comparison, deviations are calculated with respect to the selected proposed-model configuration. Absolute deviations are defined as the arithmetic difference between each compared EnergyPlus model and the selected configuration. Relative deviations are calculated by normalizing this difference by the corresponding value of the selected configuration. For any STPV comparison quantity X, the absolute deviation, ΔX_m, is calculated as follows:

$$\Delta X_m = X_m - X_{MSM,sel} \tag{27}$$

and the relative deviation, δX_m [%], is calculated as follows:

$$\delta X_m = \frac{X_m - X_{MSM,sel}}{X_{MSM,sel}} \cdot 100 \tag{28}$$

where X_m is the value of the compared EnergyPlus model, and $X_{\text{MSM,sel}}$ is the corresponding value of the selected proposed-model configuration. Depending on the comparison, X may represent annual PV yield, median PV cell temperature, or median effective efficiency.

Each processed output is linked to a case identifier containing the relevant comparison dimensions, including system family, typology, orientation, geometry level where applicable, PV-yield assessment approach, and, for STPVs, the cell-temperature assessment approach and coupling formulation.

3. Results

The results are reported separately for PVSD and STPV. The PVSD analysis compares annual yield across the three shading-complexity levels. The STPV analysis first evaluates the tested temperature and coupling formulations and then compares the selected MSM configuration with the other EnergyPlus PV models. Unless stated otherwise, relative differences are reported with respect to the EnergyPlus modified Simple model (MSM), used here as the proposed model. Positive values indicate a higher annual PV yield than MSM, while negative values indicate lower annual PV yield. The corresponding absolute

PV-yield values and additional monthly STPV results are provided in Appendix C to support numerical transparency.

3.1. PVSD Results: Cross-Tool Comparison

For the PVSD cases, the annual PV yield is used as the comparison metric and is expressed in kWh/m^2·y of installed louver area. The absolute annual PV-yield values underlying the relative comparisons are provided in Appendix C (Tables A4–A6 for Levels 0–2, respectively). This subsection first compares the PV-yield assessment approaches within each geometry level, from the unshaded reference condition to the urban-shading condition. It then isolates two effects: the yield difference caused by the AOI and temperature modifiers implemented in the MSM, and the yield reduction caused by increasing shading complexity from Level 0 to Level 2.

3.1.1. Level 0: Cross-Tool Differences Without Geometric Shading

Level 0 establishes the baseline comparison before geometric shading is introduced. It therefore provides the reference condition for assessing how the PV-yield assessment approaches differ under the same surface-orientation and irradiance conditions.

Across the Level 0 configurations in Figure 13, the PV-yield assessment approaches retain the same relative position with respect to MSM: EODM remains closest to MSM, SM and LBT remain higher than MSM, and PVGIS remains lower than MSM. EODM differs from MSM by about 0.5–3.3%, while SM is generally about 8.4–10.9% higher and LBT is about 7.2–10.8% higher. PVGIS shows the largest separation from MSM and remains lower across the full Level 0 set.

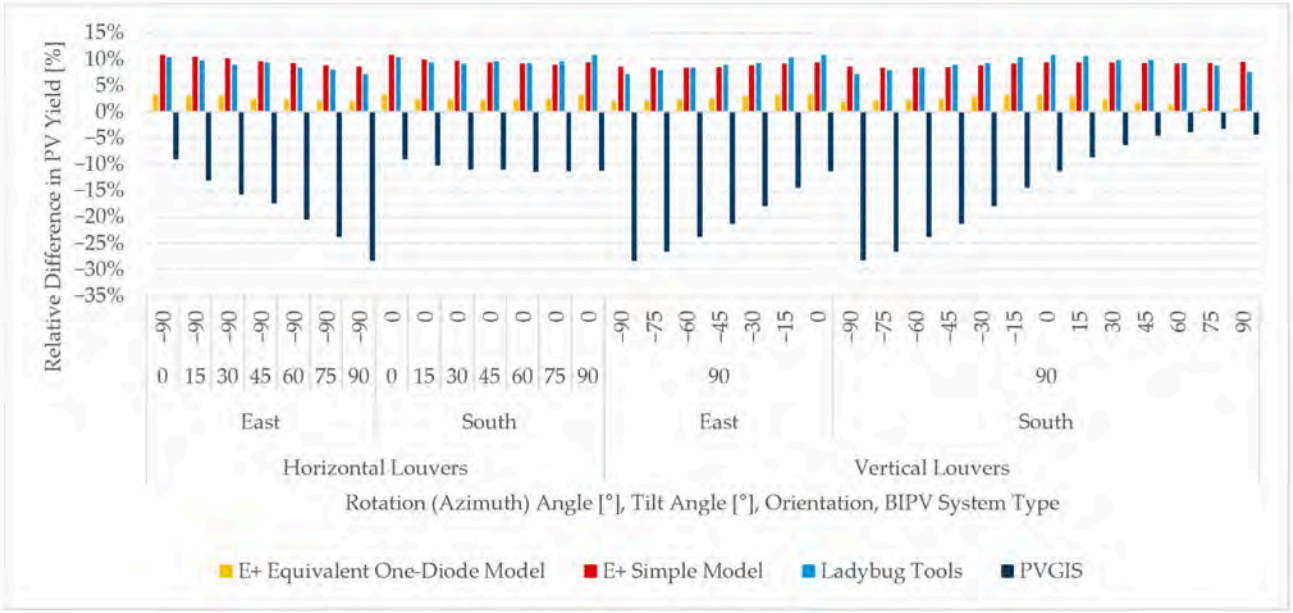

Figure 13. Relative differences in annual PV yield across assessment approaches for Level 0 PVSD configurations.

For horizontal louvers, the PVGIS deviation ranges from about −9.0% to −28.4% relative to MSM. The largest negative deviations occur in the East orientation at steeper tilt angles. For vertical louvers, PVGIS remains lower than MSM across all Level 0 cases, but the deviation varies strongly with rotation angle. In the South-facing set, negative rotations show larger deviations, reaching −28.3% at −90°, whereas positive rotations approach MSM more closely, with deviations of −3.3% to −4.3% near +75° to +90°.

Overall, Level 0 shows a clear separation between the assessment approaches, with EODM closest to MSM, SM and LBT moderately higher, and PVGIS consistently lower but more sensitive to louver orientation and angle.

The selected additional climate-transferability analysis at Level 0 shows that the relative ordering of the assessment approaches remains mostly unchanged across Trondheim, Turin, and Malaga for the four selected PVSD configurations, as shown in Figure 14. SM and LBT are higher than MSM in all selected cases, and EODM stays closest to MSM. Across the three climates and selected configurations, SM deviations range from 6.10% to 9.28%, with LBT deviations from 5.81% to 9.39% above MSM. For SM and LBT, the deviations are generally lowest in Trondheim and higher in Turin and Malaga, although the exact ranking between Turin and Malaga depends on the selected configuration. EODM shows much smaller differences, between 0.05% and 2.28%, and therefore remains close to MSM across all three climates. This is consistent with the close agreement already observed in the full Turin Level 0 comparison.

Figure 14. Relative differences in annual PV yield for selected Level 0 PVSD configurations across Turin, Trondheim, and Malaga.

PVGIS also keeps the same overall position as in the Turin Level 0 results, but with a wider spread than the other approaches. It remains below MSM in all selected cases, with deviations ranging from −28.42% to −0.10%. The largest negative deviations occur for the East-facing configurations in Turin and Malaga, while the South-facing horizontal case is closer to MSM, especially in Trondheim.

Overall, the climate-transferability analysis confirms the main Level 0 pattern observed for Turin. MSM keeps the same relative position across the selected climate locations: SM and LBT remain above it, EODM remains very close to it, and PVGIS remains below it. The climate location therefore does not change the cross-tool hierarchy, but it does affect the size of the deviations around MSM. This can be related to the different radiation patterns and outdoor temperature conditions under which the same PVSD orientations and angles are evaluated. In the selected cases, the climate-dependent ranges are relatively narrow for

SM, LBT, and especially EODM, while PVGIS shows the widest variation across climate and configuration.

3.1.2. Level 1: Cross-Tool Differences Under Self-Shading

Level 1 repeats the comparison after explicit PVSD louver geometry and self-shading are introduced. As shown in Figure 15, PVGIS no longer remains consistently below MSM, while SM and LBT remain mostly above MSM across the tested configurations.

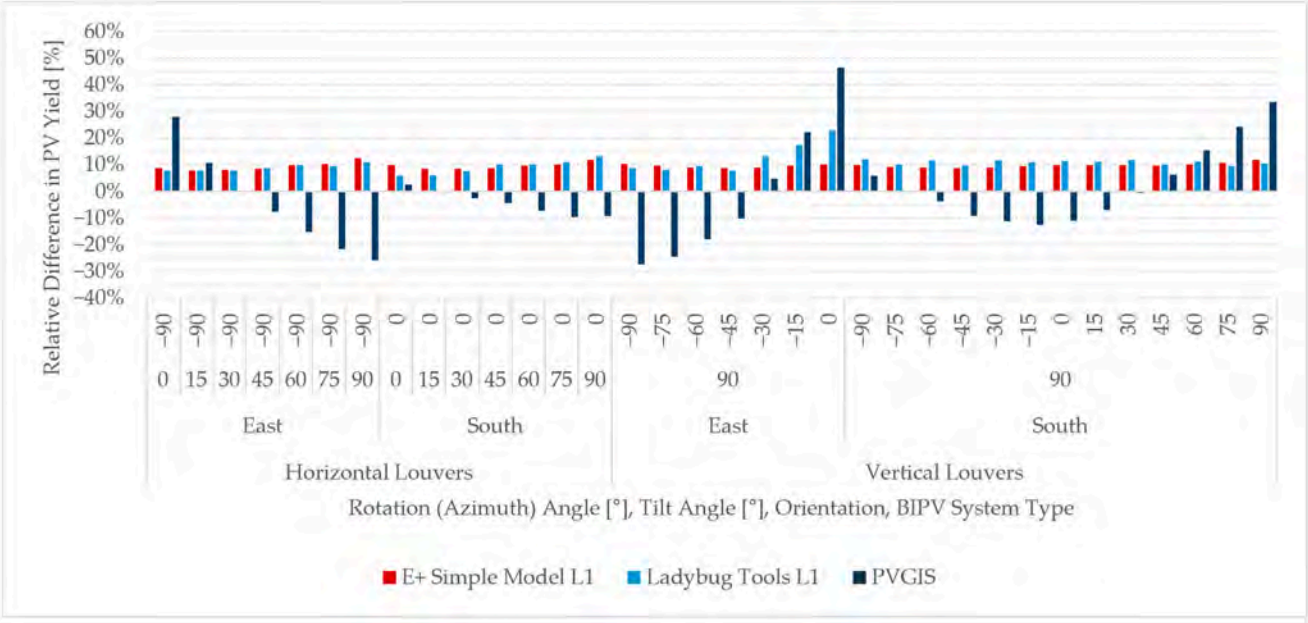

Figure 15. Relative differences in annual PV yield across assessment approaches for Level 1 PVSD configurations.

For horizontal louvers, the PVGIS deviation changes from positive to negative values as tilt angles increase. In the East orientation, PVGIS is 28.1% above MSM at 0°, nearly aligned with MSM at 30°, and 25.8% below MSM at 90°. In the South orientation, the range is narrower: PVGIS is 2.6% above MSM at 0° and decreases to negative deviations from 15° onward, reaching −9.7% at 75°.

For vertical louvers, the PVGIS range is wider and changes sign in both orientations. In the East orientation, PVGIS shifts from −27.3% at −90° to +46.4% at 0°. In the South orientation, PVGIS ranges from −12.5% at −15° to +33.5% at 90°, with values close to MSM at −75° and 30°.

SM remains above MSM across all Level 1 cases. Its deviations range from 7.9% to 12.5% for horizontal louvers and from 8.7% to 11.8% for vertical louvers. LBT also remains mostly above MSM, with deviations of 5.8–13.2% for horizontal louvers and 7.9–22.9% for vertical louvers. The largest LBT deviations occur for East-facing vertical louvers near 0°. Overall, Level 1 is characterized by a configuration-dependent PVGIS response, including several sign changes, while SM and LBT remain mostly higher than MSM.

3.1.3. Level 2: Cross-Tool Differences Under Urban Shading

Level 2 applies the PVSD configurations to the reference building and introduces the surrounding urban context. As shown in Figure 16, PVGIS is higher than MSM across all Level 2 configurations, while SM and LBT remain much closer to MSM. This separation is linked to the comparison boundary: PVGIS is kept as an unshaded external reference and therefore does not explicitly represent the three-dimensional louver geometry, façade

placement, or surrounding urban obstructions included in the Level 2 EnergyPlus- and Ladybug-based simulations.

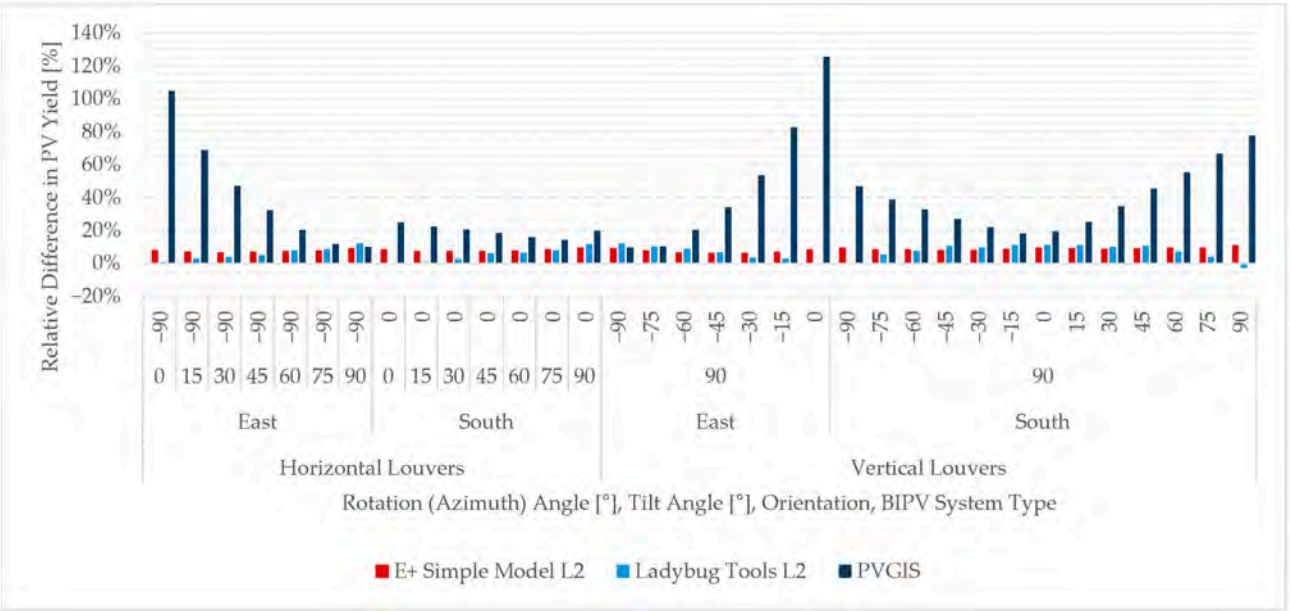

Figure 16. Relative differences in annual PV yield across assessment approaches for Level 2 PVSD configurations.

For horizontal louvers, the largest PVGIS deviations occur in the East orientation at low tilt angles. PVGIS is 104.9% higher than MSM at 0°, and the deviation decreases to 10.1% at 90°. In the South orientation, the PVGIS deviation remains positive and ranges from 14.2% to 24.9%, with the largest value at 0°.

For vertical louvers, PVGIS also remains higher than MSM across all Level 2 cases. In the East orientation, the deviation ranges from 9.8% at −90° to 125.8% at 0°. In the South orientation, it ranges from 18.2% at −15° to 77.8% at 90°, with the highest values occurring at positive rotation angles.

SM remains above MSM in all Level 2 cases, with deviations of 7.0–9.8% for horizontal louvers and 6.4–11.2% for vertical louvers. LBT remains closer to MSM than PVGIS, although its values include both small negative and positive deviations. For horizontal louvers, LBT ranges from −0.1% to 12.0%; for vertical louvers, it ranges from −2.8% to 12.0%. Overall, the Level 2 comparison is dominated by positive PVGIS deviations, while SM and LBT remain within narrower ranges around MSM.

3.1.4. Effect of AOI and Temperature Modifiers

This comparison isolates the difference between SM and MSM across Levels 0–2. SM uses a fixed efficiency, whereas MSM uses the time-varying effective-efficiency formulation with AOI and temperature modifiers. The relative difference between the two therefore represents the yield difference associated with these modifiers, because both models use the same EnergyPlus geometry and irradiance basis but differ in whether AOI-related reflection losses and temperature-related efficiency losses are applied.

As shown in Figure 17, SM remains higher than MSM across all louver typologies, orientations, angles, and geometry levels. The SM–MSM difference ranges from 6.2% to 11.1% across the full set, with most values between 7.0% and 10.0%.

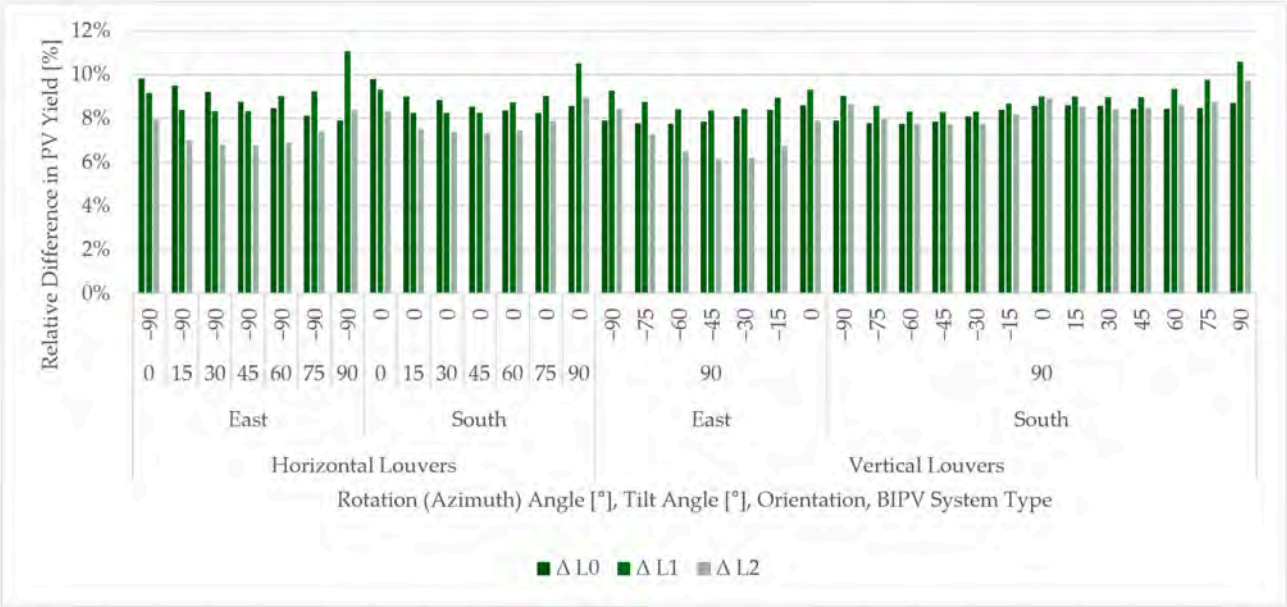

Figure 17. Relative differences in PV yield between EnergyPlus Simple model (SM) and the modified Simple model (MSM) across PVSD geometry levels.

For horizontal louvers, the difference ranges from 6.8% to 11.1%. In the East orientation, values decrease from 9.8% to 7.9% at Level 0 and from 8.0% to 6.8% at Level 2, while Level 1 increases toward the steeper tilt angles and reaches 11.1% at 90°. In the South orientation, the values remain between 7.3% and 10.5%, with the highest value again occurring at Level 1 and 90°.

For vertical louvers, the difference ranges from 6.2% to 10.6%. In the East orientation, Level 2 includes the smallest values, with a minimum of 6.2% at −45° to −30°. In the South orientation, the values remain within a narrower range of 7.7–10.6%, with the largest value at Level 1 and 90°. Overall, the SM–MSM difference remains positive across all Levels 0–2 cases, with most values clustered between 7.0% and 10.0% and only a few cases exceeding 10.0%.

3.1.5. Effect of Increasing Shading Complexity

This comparison evaluates yield reductions within MSM as shading complexity increases across geometry levels. Relative differences are calculated for the transitions from Level 0 to Level 1, from Level 1 to Level 2, and from Level 0 to Level 2. The values are reported as yield reductions relative to the first level in each pair.

As shown in Figure 18, the Level 0–Level 2 comparison produces the largest reductions across all configurations. Across the full case set, Level 0–Level 2 reductions range from 22.4% to 60.7%. Level 1–Level 2 reductions range from 17.8% to 37.1%, while Level 0–Level 1 reductions range from 0.5% to 39.5%.

For horizontal louvers, the largest reductions occur in the East orientation at low tilt angles. The Level 0–Level 2 reduction reaches 55.8% at 0° and decreases to 31.8–34.9% at 75–90°. The Level 0–Level 1 reduction follows a similar decrease, from 29.7% at 0° to 2.9–3.4% at 75–90°. The Level 1–Level 2 reduction remains within 29.5–37.1% in the East orientation. In the South orientation, the reductions are smaller, with Level 0–Level 2 values ranging from 22.4% to 27.4%.

For vertical louvers, the reductions vary with rotation angle. In the East orientation, the Level 0–Level 2 reduction increases from 34.7% at −90° to 60.7% at 0°. The Level 0–Level 1 reduction also increases toward 0°, from 1.5% at −90° to 39.5% at 0°, while the Level 1–Level 2 reduction remains between 31.6% and 35.0%. In the South orientation, the

Level 0–Level 2 reduction is lowest at 0° with 26.0% and increases toward both rotation extremes, reaching 51.1% at −90° and 46.0% at 90°. The Level 0–Level 1 reduction follows the same angular pattern, while the Level 1–Level 2 reduction remains between 24.6% and 28.3%.

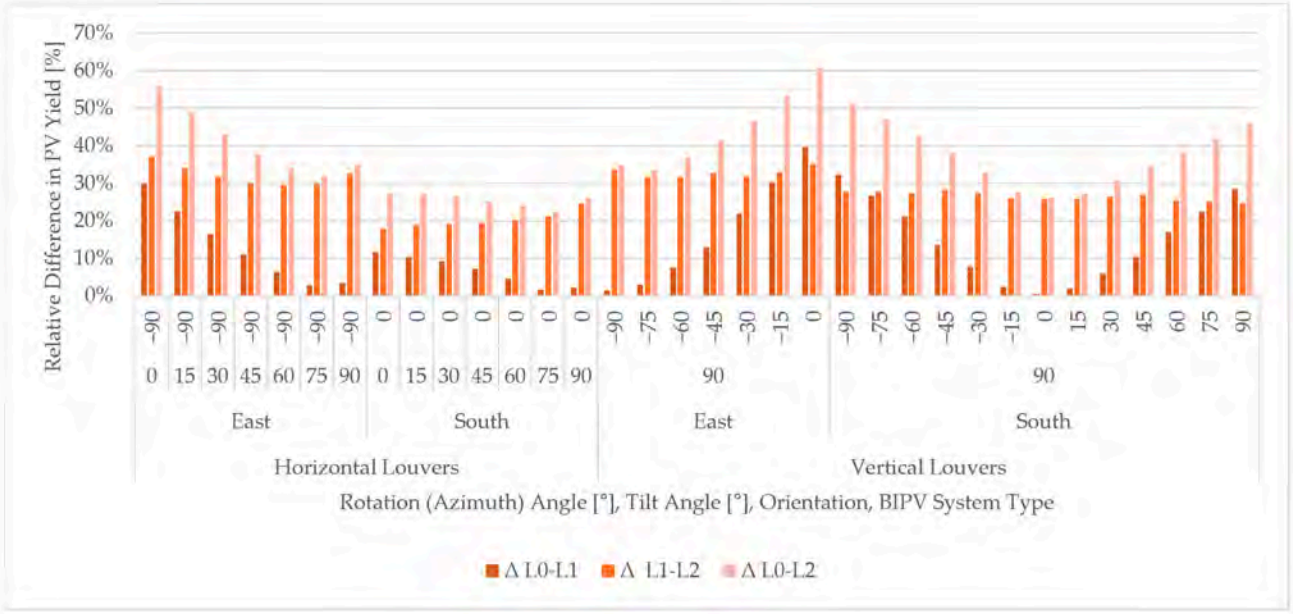

Figure 18. Relative PV yield reductions across PVSD geometry levels using the EnergyPlus modified simple model (MSM).

Overall, the inter-level comparison shows the largest yield reductions for the full Level 0–Level 2 transition, while the Level 1–Level 2 transition remains consistently higher than the Level 0–Level 1 transition in most configurations. This indicates that the additional urban-context shading introduced at Level 2 contributes substantially to the total yield reduction, beyond the self-shading already introduced by the louver geometry at Level 1.

3.2. STPV Results: Modeling-Choice and Cross-Model Comparison

For the STPV cases, annual median PV cell temperature, annual median effective efficiency, and annual PV yield are used to compare alternative MSM modeling choices for STPVs. The subsection first compares the heat-balance-based and NOCT-based cell-temperature approaches under decoupled and coupled formulations. It then compares the selected MSM configuration with SM and EODM using annual PV yield. Monthly values for the STPV modeling-choice comparisons and the final cross-model yield comparison are provided in Appendix C (Tables A7 and A8, respectively). Temperature and effective-efficiency medians are calculated only for hours with solar radiation incident on the STPV window.

3.2.1. Effects of Cell-Temperature and Coupling Formulations

For PV cell temperature, Figure 19 shows higher annual median values for the NOCT-based approach than for the heat-balance-based approach in both orientations. In the East orientation, the heat-balance-based cases range from 22.6 °C to 23.0 °C, while the NOCT-based cases range from 26.7 °C to 27.0 °C. In the South orientation, the corresponding ranges are 25.3–25.8 °C for the heat-balance-based cases and 31.4–31.9 °C for the NOCT-based cases. For both cell-temperature assessment approaches, the South-facing cases show higher annual median PV cell temperatures than the East-facing cases.

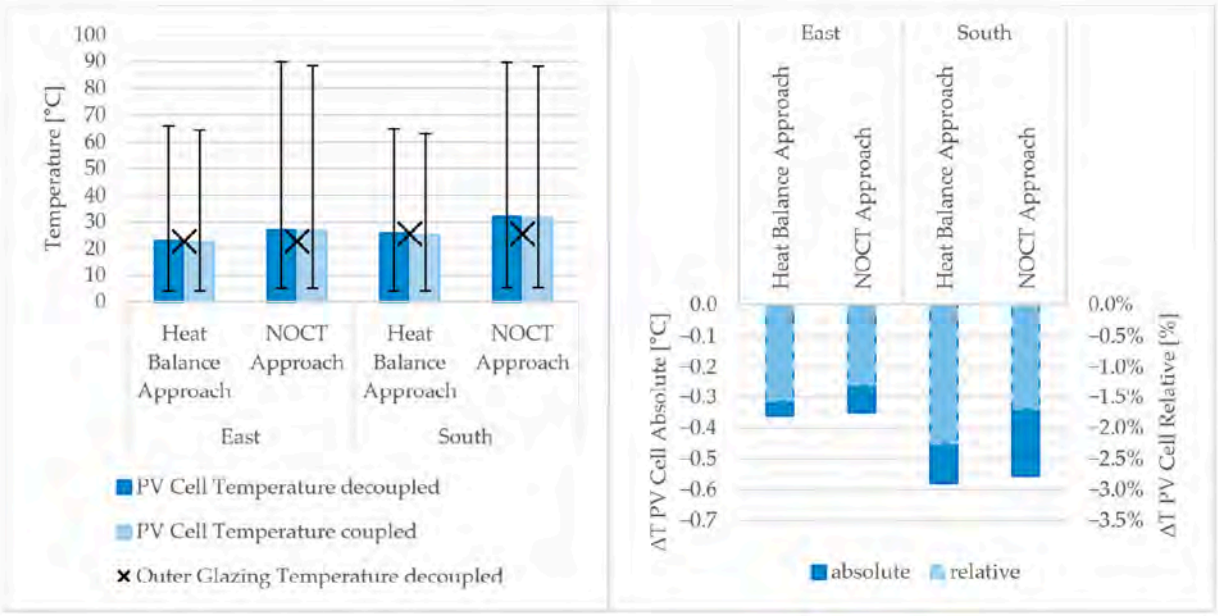

Figure 19. STPV cell-temperature assessment under coupled and decoupled formulations: (**Left**) annual median PV cell temperature during sunlit hours for heat-balance and NOCT approaches; (**Right**) absolute and relative PV cell-temperature differences between coupled and decoupled formulations.

The annual median outer glazing temperature is included as a reference quantity for the STPV laminate location. It is 22.7 °C in the East orientation and 25.5 °C in the South orientation. These values are close to the heat-balance-based PV cell-temperature values and lower than the NOCT-based values. In addition, the reported annual minimum and maximum PV cell temperatures refer to the full set of sunlit hours. These values show wider temperature ranges for the NOCT-based cases than for the heat-balance-based cases.

When compared by coupling formulation, the coupled formulation produces slightly lower annual median PV cell temperatures than the decoupled formulation in both orientations and for both cell-temperature assessment approaches. In Figure 19, where the coupled case is compared against the decoupled case, these differences are shown as negative values. The absolute differences range from −0.3 °C to −0.6 °C, corresponding to relative differences of −1.3% to −2.2%.

Figure 20 compares the annual median effective efficiencies with the nominal efficiency of 3.60%. All annual median effective efficiencies remain below the nominal value. In the East orientation, the heat-balance-based cases are 3.40%, while the NOCT-based cases are 3.36%. In the South orientation, the heat-balance-based cases range from 3.29% to 3.30%, while the NOCT-based cases range from 3.18% to 3.19%. Within each cell-temperature assessment approach, the coupled formulation produces slightly higher effective-efficiency values than the decoupled formulation.

The annual PV-yield values in Figure 20 are higher for the South orientation than for the East orientation across all four modeling-choice combinations. In the East orientation, the heat-balance-based cases are 23.8 kWh/m^2·y under both coupling formulations, while the NOCT-based cases range from 23.3 to 23.8 kWh/m^2·y. In the South orientation, the heat-balance-based cases range from 34.0 to 34.1 kWh/m^2·y, while the NOCT-based cases range from 33.2 to 34.1 kWh/m^2·y. The monthly values in Appendix C.2 show that the two orientations have different seasonal yield profiles. For the selected heat-balance-based decoupled MSM configuration, the East-facing STPV case increases from 0.92 kWh/m^2·m in January to 3.12 kWh/m^2·m in August. The South-facing case instead remains higher in winter and shoulder months, with values of 3.20 kWh/m^2·m in January, 3.29 kWh/m^2·m in March, and 3.23 kWh/m^2·m in December, while the lowest values occur in June and July.

This seasonal pattern is consistent with the vertical STPV geometry, where the South-facing window benefits from lower solar altitudes outside summer, while the East-facing window receives a stronger summer contribution.

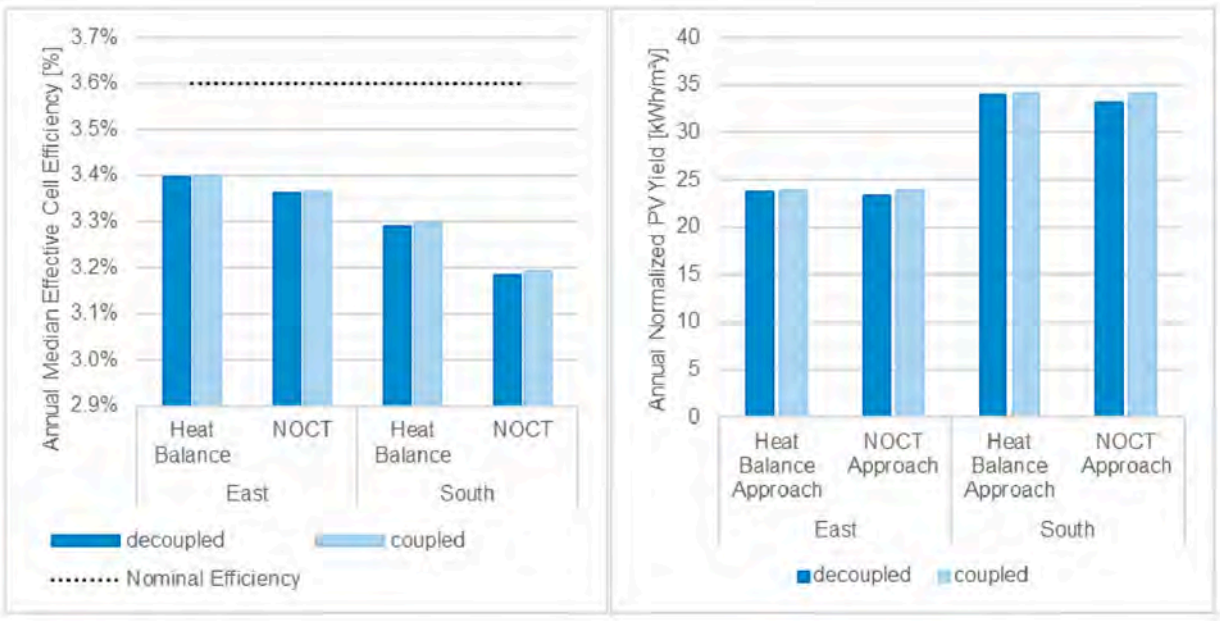

Figure 20. STPV effective efficiency and PV yield for heat-balance and NOCT cell-temperature assessment approaches under decoupled and coupled formulations: (**Left**) annual median effective efficiency compared with nominal efficiency; (**Right**) annual normalized PV yield.

Overall, the modeling-choice comparison shows larger differences between the two cell-temperature assessment approaches than between the two coupling formulations for annual median PV cell temperature and annual median effective efficiency. The annual PV-yield values remain within a narrower range across the four combinations, which is consistent with the low nominal efficiency and a comparatively small temperature coefficient of the tested a-Si STPV case.

3.2.2. Cross-Model Comparison for STPV Yield

The STPV cross-model comparison uses the heat-balance-based decoupled formulation as the selected MSM configuration. Annual PV yield is compared with SM and EODM.

As shown in Figure 21, SM has the highest annual PV yield in both orientations, followed by the selected MSM configuration and EODM. In the East orientation, annual PV yield is 25.9 kWh/m^2·y for SM, 23.8 kWh/m^2·y for MSM, and 17.5 kWh/m^2·y for EODM. In the South orientation, the corresponding values are 37.7 kWh/m^2·y for SM, 34.0 kWh/m^2·y for MSM, and 28.1 kWh/m^2·y for EODM. For the selected STPV configuration, the lower MSM yield relative to SM reflects the application of AOI- and temperature-loss modifiers to the glazing-integrated PV layer, which reduces the fixed-efficiency yield calculated by SM. The monthly values in Appendix C.2 show that this model ordering is maintained throughout the year: SM remains above the selected MSM configuration, while EODM remains below it every month for both orientations. The East-facing cases show higher monthly yields in late spring and summer, whereas the South-facing cases retain higher values in winter and shoulder months and show lower values during summer.

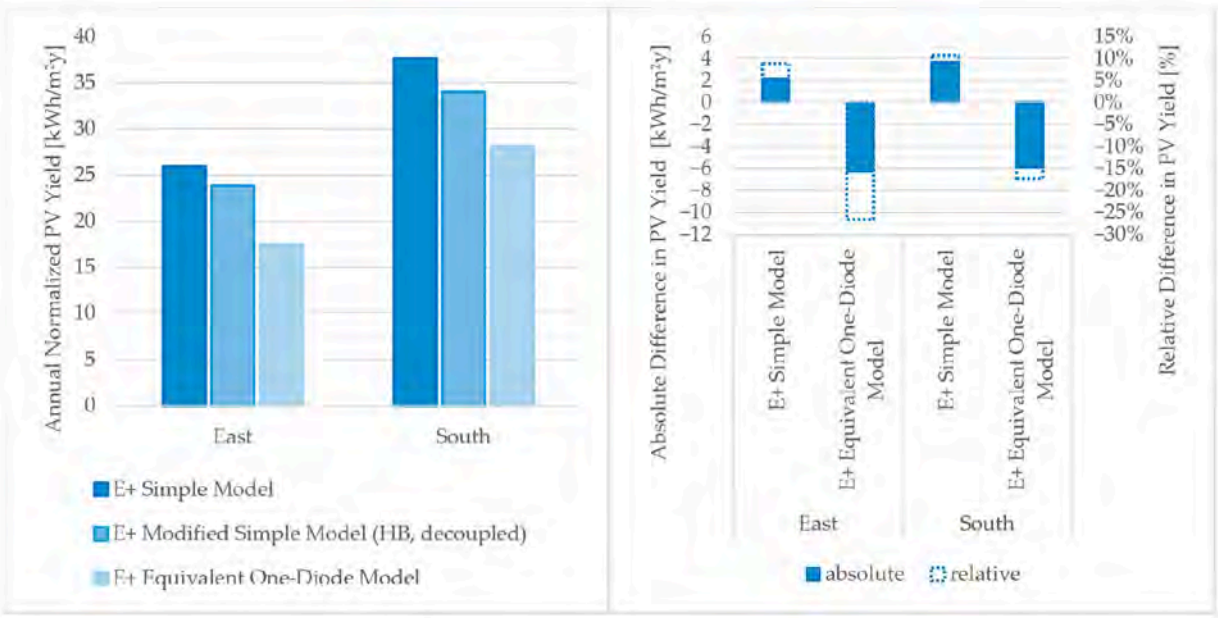

Figure 21. Cross-model comparison of STPV annual PV yield across EnergyPlus model configurations: (**Left**) annual normalized PV yield for SM, the selected MSM configuration, and EODM; (**Right**) absolute and relative differences with respect to the selected MSM configuration.

Figure 21 reports the absolute and relative differences between SM or EODM and the selected MSM configuration. SM is higher than MSM by 2.1 kWh/m^2·y in the East orientation and 3.7 kWh/m^2·y in the South orientation, corresponding to relative differences of 8.9% and 10.7%. EODM is lower than MSM by 6.3 kWh/m^2·y in the East orientation and 5.9 kWh/m^2·y in the South orientation, corresponding to relative differences of −26.6% and −17.3%.

Overall, the selected MSM configuration remains between SM and EODM in both orientations, with smaller differences to SM than to EODM.

The additional STPV cross-model climate comparison is shown in Figure 22. Across Trondheim, Turin, and Malaga, the relative ordering of the three EnergyPlus models remains unchanged in both orientations. SM remains higher than MSM, while EODM remains lower than MSM in all selected cases. Across the three climates and both orientations, SM deviations range from 7.52% to 11.76% above MSM, with the lowest deviations in Trondheim and higher deviations in Turin and Malaga.

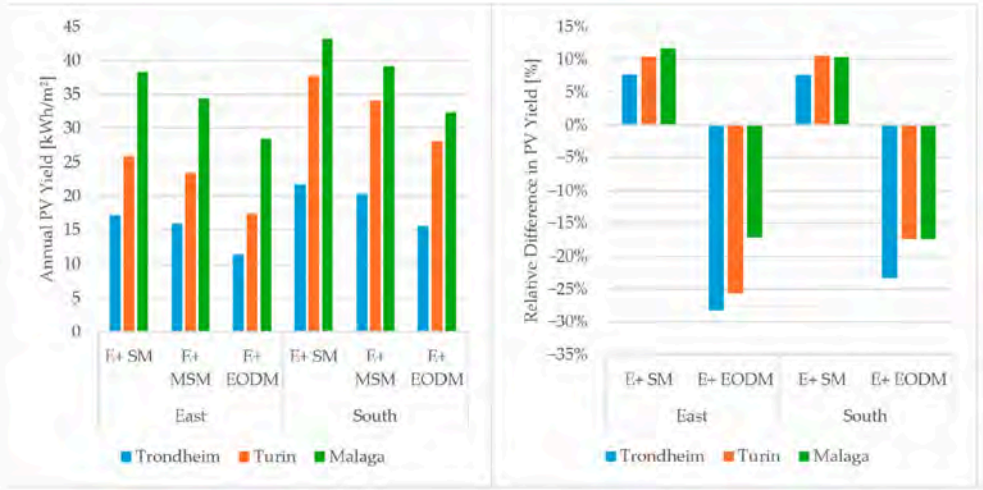

Figure 22. Relative differences in annual STPV yield across Turin, Trondheim, and Malaga.

EODM shows larger negative deviations from MSM. The differences range from −28.26% to −17.15% in the East orientation and from −23.26% to −17.36% in the South orientation, with the largest separation in Trondheim and smaller deviations in Malaga. Overall, the selected MSM configuration keeps the same relative position across the tested climates and orientations, remaining between SM and EODM while the magnitude of the deviations changes with climate and orientation.

4. Discussion

This discussion interprets what the comparison shows for PVSD and STPV yield assessment. It first addresses the role of shading representation and PV-conversion losses in the PVSD cases, then discusses the STPV temperature and coupling assumptions before summarizing the contribution and remaining limitations.

4.1. Interpretation of PVSD Cross-Tool Differences

The PVSD comparison is interpreted through two related aspects: how the proposed model relates to the other tools and models, and how geometric shading representation affects assessed yield. The first aspect is clearest under unshaded Level 0 conditions, where differences mainly reflect PV-conversion modeling, including the AOI- and temperature-related loss mechanisms included in the proposed model. The second emerges at Levels 1 and 2, where explicit louver geometry and surrounding context are introduced.

Under Level 0 conditions, explicit geometric shading is excluded. This makes Level 0 the most direct basis for interpreting differences in PV-conversion modeling. In this comparison, the EnergyPlus Simple model (SM) and Ladybug Tools (LBT) produce higher annual yields than the proposed model, which is consistent with their fixed-efficiency logic and the absence of AOI- and temperature-related efficiency losses. By contrast, the proposed model aligns closely with the EnergyPlus Equivalent One-Diode model (EODM). This alignment is relevant because EODM uses a more detailed electrical formulation but requires module-specific parameters that are often unavailable before product selection. Within the tested unshaded cases, the Level 0 comparison shows that MSM reaches annual yield levels close to EODM while requiring fewer electrical input parameters. This supports its use as an intermediate early-stage option for representing selected AOI- and temperature-related losses.

The selected additional climate-transferability analysis adds a check to the Level 0 interpretation because it tests whether the position of MSM changes when the same selected PVSD cases are evaluated with different weather files. MSM keeps its intermediate position across Trondheim, Turin, and Malaga. It remains lower than the fixed-efficiency SM and LBT results, close to EODM, and higher than PVGIS. The additional climates show that this model ordering is not specific to the Turin weather file, although the comparison remains limited to the selected European climate cases. The added climates therefore broaden the comparison beyond the original reference case, while still remaining within a selected European climate set. The differences between climates are still meaningful, but they mainly appear in the size of the deviations rather than in the model ordering. This is plausible because MSM responds to the hourly incidence-angle and temperature conditions of each weather file, whereas SM uses a fixed efficiency. In Trondheim, where the tested conditions are cooler and have lower irradiation, the difference to SM and LBT is smaller. In Turin and Malaga, the AOI- and temperature-adjusted formulation becomes more visible, so the distance to the fixed-efficiency approaches increases. EODM stays close to MSM across the selected climates, which supports the interpretation that the effective-efficiency formulation reaches a similar annual yield level to the more detailed EnergyPlus electrical model for the tested unshaded cases. PVGIS shows the widest spread, suggesting that its

relation to MSM is more sensitive to the combination of climate, orientation, and louver angle than the EnergyPlus-based comparisons.

Levels 1 and 2 show that PVSD yield assessment is also strongly affected by geometric shading representation. The introduction of explicit louver geometry at Level 1 produces substantial yield reductions compared with the unshaded setup, indicating that self-shading is an important performance driver for the tested PVSD systems. This effect is directly linked to the louver arrangement and therefore should be represented when comparing PVSD configurations. The inter-level comparison also shows that the surrounding context contributes a substantial share of the total reduction. In several configurations, the Level 1–Level 2 reduction is larger than the Level 0–Level 1 reduction, so the urban context becomes a major part of the assessed PVSD yield loss. In this comparison, these reductions mainly reflect how louver geometry and surrounding context reduce the incident irradiance on the PVSD surfaces. Detailed electrical effects under non-uniform shading, such as mismatch or string-level behavior, are not resolved in the present PVSD comparison. For early-stage PVSD assessment, comparative yield calculations should therefore include the relevant louver geometry and surrounding context, because both materially affect simulated performance in the tested cases. While louver self-shading is especially relevant to PVSD configurations, urban-context shading is also relevant for façade-integrated BIPV assessment more broadly. The SM–MSM comparison adds a second layer to this interpretation. Even after self-shading and urban-context shading are introduced, SM remains higher than MSM. This shows that the AOI- and temperature-related efficiency losses remain visible across the tested geometry levels, not only in the unshaded Level 0 case.

The changing relation between PVGIS and the proposed model further supports this interpretation. Across the three geometry levels, the PVGIS comparison does not follow a stable relation to the proposed model. It remains lower under Level 0 conditions, becomes configuration-dependent at Level 1, and remains higher across the tested Level 2 cases. Because the largest differences occur when explicit louver geometry and surrounding context are included, the results indicate that PV-yield tools without explicit geometry representation may be less suitable for assessing PVSD configurations whose performance depends strongly on geometry and shading context. The comparison boundary helps explain this pattern. PVGIS is kept as an external reference, whereas the EnergyPlus- and Ladybug-based simulations include explicit louver geometry from Level 1 onward and façade placement and urban obstructions at Level 2. The PVGIS difference is therefore not a constant offset from MSM. It changes as the comparison boundary changes: from unshaded yield calculation at Level 0 to self-shaded louver geometry at Level 1 and façade plus urban-context shading at Level 2. Because PVGIS is kept as an external unshaded reference, its relation to MSM changes when these geometric effects are added to the EnergyPlus and Ladybug simulations. This helps explain why PVGIS is below MSM at Level 0, configuration-dependent at Level 1, and higher than MSM at Level 2. This supports geometry-aware workflows for PVSD assessment, because the comparison is strongly shaped by the geometry and context included in the model.

Overall, the PVSD results show that the proposed model can be implemented within a geometry-aware simulation workflow while accounting for selected AOI- and temperature-related PV-conversion losses. The main finding is not only that the proposed model changes the assessed PV-conversion behavior relative to fixed-efficiency calculations, but also that PVSD yield assessment depends strongly on how louver self-shading and surrounding-context shading are represented. For the tested PVSD cases, the results therefore point to the need to consider PV-conversion losses, louver geometry, and surrounding context together when estimating annual yield at an early design stage.

4.2. Interpretation of STPV Modeling-Choice Differences

The STPV results are interpreted through two related questions: how the selected modeling assumptions affect simulated PV cell temperature, effective efficiency, and annual PV yield, and how the selected configuration of the proposed model compares with the other EnergyPlus PV models. This requires a separate discussion from the PVSD case because the PV-active layer is part of a glazing system and therefore links PV generation to the solar–optical and thermal behavior of the window. The PV-yield calculation is therefore connected not only to incident radiation and conversion efficiency, but also to the thermal state of the glazing layer.

The modeling-choice comparison shows that PV cell-temperature assessment has the clearest effect among the tested STPV assumptions. The NOCT-based variant produces higher PV cell temperatures because it adds an empirical irradiance-dependent temperature rise to the simulated glazing temperature, which already accounts for the thermal behavior of the window. These higher NOCT-based temperatures are therefore mainly a consequence of the selected temperature formulation, rather than an independently resolved STPV cell-temperature calculation.

The choice of temperature basis can change annual PV-yield estimates, especially when irradiance, glazing temperature, and STPV technology differ across climates or products. In the adapted NOCT-based STPV variant, the irradiance-dependent NOCT term is not added to outdoor air temperature, as in the conventional module-temperature formulation, but to the simulated exterior surface temperature of the STPV laminate. This exterior glazing temperature is already the result of the EnergyPlus window heat balance and therefore reflects outdoor and indoor boundary conditions, absorbed solar radiation, heat exchange, and the thermal and optical properties of the glazing stack. Adding a further irradiance-dependent temperature rise to this simulated glazing-temperature basis can therefore amplify the calculated PV cell temperature, particularly in climates where high irradiance coincides with elevated glazing temperatures. In colder or more diffuse climates, the absolute temperature level may be lower, but the difference between the two methods can still depend on how outdoor temperature, solar absorption, and the direct-to-diffuse radiation balance affect the simulated window heat balance.

The heat-balance-based approach avoids this additional empirical temperature rise and keeps the cell-temperature estimate tied to the simulated thermal state of the glazing layer. This is relevant for STPV because the PV-active layer is embedded in a glazing system rather than exposed as an opaque module surface. The method remains approximate because it uses a layer-averaged temperature estimate and does not resolve a separate PV-active thermal node. It is therefore a simplified glazing-based temperature estimate, not a detailed PV-layer thermal model. However, the WINDOW comparison in Appendix D supports the numerical consistency of the reconstructed inner-face temperature used in this workflow. The comparison therefore suggests that empirical module-temperature formulations require careful adaptation before being transferred to STPV glazing, while more detailed PV-layer thermal models would be preferable for later-stage or product-specific assessment.

The temperature-assessment approach affects effective efficiency through the temperature modifier. Higher NOCT-based PV cell temperatures increase temperature-related losses and lead to lower effective efficiencies, especially in the South orientation. However, the corresponding annual PV-yield differences remain modest. This can be explained by two related factors: the low temperature coefficient of the assumed a-Si technology reduces sensitivity to PV cell-temperature differences, while the low nominal efficiency of the tested STPV configuration limits the absolute magnitude of electricity-generation changes.

The limited annual-yield effect observed in the tested a-Si case is therefore linked to the selected technology assumptions. For technologies with stronger negative temperature

coefficients, differences in the estimated PV cell temperature could translate more directly into effective-efficiency differences. For higher-efficiency STPV products, the same relative efficiency reduction could correspond to a larger absolute reduction in the annual electricity yield. Different absorptance values, layer positions, laminate thicknesses, or glazing-stack compositions could further change the glazing temperature field from which the heat-balance-based estimate is derived. The reduction from nominal to effective efficiency should therefore be read as the combined result of the applied AOI- and temperature-related modifiers, while the comparison between the two temperature approaches isolates the additional effect of the cell-temperature assumption. The STPV results should therefore be read in relation to the tested a-Si configuration, rather than as a general ranking of all possible STPV temperature approaches.

The coupling formulation has a smaller effect than the temperature-assessment approach. It describes whether PV electricity generation is fed back into the glazing heat-balance calculation. The coupled case produces slightly lower annual median PV cell temperatures and marginally higher effective efficiencies than the decoupled case, but the resulting annual PV-yield differences remain limited. For the selected a-Si STPV window test case, the coupling formulation is therefore not a dominant driver of annual simulated yield.

This limited effect is linked to the low-efficiency a-Si configuration and the tested glazing assembly, because coupling effects can become more pronounced for higher-efficiency STPV products or different glazing assemblies. This is because higher conversion efficiency increases the fraction of incident solar radiation converted into electricity rather than retained as heat in the glazing system. Feeding this larger electricity-converted fraction back into the heat-balance calculation could therefore have a stronger effect on absorbed heat, glazing temperature, and related room-scale thermal outputs.

The cross-model comparison places the selected heat-balance-based decoupled configuration of the proposed model between the EnergyPlus Simple model (SM) and the EnergyPlus Equivalent One-Diode model (EODM). SM remains higher, consistent with its fixed-efficiency formulation and the absence of AOI- and temperature-related efficiency reductions. EODM remains lower by a larger margin, which should be interpreted cautiously in relation to the STPV technology assumptions.

This may partly be related to the fact that the EODM setup is more directly aligned with crystalline-silicon PV assumptions, whereas the investigated STPV laminate is based on amorphous silicon (a-Si). Since a-Si can perform relatively well under diffuse irradiance compared with crystalline silicon [46], using a crystalline-silicon-based electrical model for an a-Si laminate can potentially lead to lower calculated yields for the a-Si STPV laminate under diffuse conditions. The comparison therefore reinforces the need to align PV-conversion assumptions with the investigated STPV cell technology. The relative differences between models, especially between the proposed model and EODM, should also be interpreted together with the absolute values: they appear large in percentage terms, but the corresponding absolute differences remain comparatively small because STPV yield per unit window area is low.

The additional STPV cross-model climate comparison extends this interpretation by showing that the model ordering is stable across the selected climate cases. SM remains higher than MSM in all tested climates and orientations, which is consistent with its fixed-efficiency formulation and the absence of AOI- and temperature-related efficiency reductions. EODM remains lower than MSM in all tested cases, but the magnitude of the difference varies with climate and orientation.

The negative EODM deviation is largest in Trondheim, particularly for the East orientation, and becomes smaller in Malaga. This confirms the main cross-model pattern:

the selected heat-balance-based decoupled MSM configuration remains between the fixed-efficiency SM and EODM not only in Turin but also under the cooler Trondheim conditions and the warmer Malaga conditions. The changing magnitude of the deviations shows that climate and orientation still affect the distance between the models. The SM–MSM difference is smaller in Trondheim and larger in Turin and Malaga, which is consistent with the fact that MSM responds to hourly AOI and temperature conditions, while SM keeps the conversion efficiency fixed. The EODM–MSM difference follows a different pattern and remains clearly negative, especially in Trondheim. This suggests that the gap between MSM and EODM is not only a temperature-loss effect, but is also related to the different PV-conversion formulations used for the STPV case. This is different from the PVSD comparison, where EODM remained close to MSM under Level 0 conditions. For STPV, the larger EODM–MSM gap points to the stronger role of the selected glazing-integrated PV technology and model assumptions. The selected MSM configuration therefore remains appropriate for the tested early-stage STPV setup because it keeps AOI- and temperature-related losses linked to the simulated glazing thermal state, but the absolute and relative differences to EODM should not be generalized from the Turin case alone.

For the tested STPV case, the heat-balance-based decoupled configuration is the most consistent choice for the MSM. It keeps the temperature estimate tied to the simulated glazing heat balance, while the tested coupling formulation changes annual yield only slightly. This means that the heat-balance-based approach keeps the PV temperature representation consistent with the simulated glazing heat-balance behavior, while the coupling formulation produces only limited changes in PV cell temperature, effective efficiency, and annual simulated yield for the tested low-efficiency a-Si window. The results also indicate that STPV yield assessment depends strongly on keeping the thermal and PV-conversion assumptions aligned with the glazing-integrated system and the investigated cell technology.

4.3. Methodological Contribution for Early-Stage Transparent-Envelope BIPV Assessment

Across the PVSD and STPV analyses, MSM is positioned between fixed-efficiency yield estimates and detailed electrical PV models. It adds AOI- and temperature-related efficiency corrections to the EnergyPlus Simple model, but it does not require the full input set of a detailed PV model. The main methodological contribution is therefore not a new detailed electrical model, but a building-simulation-compatible PV-yield assessment workflow that adds selected operating-condition effects while retaining limited early-stage input requirements.

This position responds to a central limitation in BIPV workflows: tools with strong geometry and building-context representation are not always detailed in their PV-conversion modeling, while detailed PV tools often require inputs that are unavailable during early design or are less compatible with explicit BIPV geometry. The present workflow addresses this limitation by modifying the EnergyPlus Simple model itself, rather than only comparing available tools or selecting among existing EnergyPlus PV model options. By embedding the effective-efficiency formulation within the EnergyPlus Simple model, the proposed approach combines building-simulation compatibility with a more explicit representation of key PV loss mechanisms. The resulting workflow does not replace detailed PV design models; rather, it provides a controlled way to examine how selected AOI- and temperature-related efficiency effects change PV-yield estimates within the same geometry-aware simulation environment.

For PVSDs, the contribution is a comparison structure in which geometric complexity is treated as an explicit assessment dimension rather than as a fixed background condition. This allows unshaded, self-shaded, and urban-context cases to be interpreted as separate

stages of increasing geometric boundary complexity. In this way, the Level 0–Level 2 structure makes the assessment boundary itself part of the comparison. For STPV windows, the contribution is greater modeling transparency: the approach makes the assumptions behind PV cell temperature and thermal–optical–electrical coupling explicit instead of treating STPV yield with a fixed efficiency applied to incident radiation. Within this workflow, this clarifies how the selected temperature basis and coupling formulation affect effective efficiency and annual yield for a glazing-integrated PV layer.

The results also show that fixed-efficiency models can preserve some relative trends while shifting absolute annual yield. This is relevant in early-stage BIPV assessment, where absolute yield estimates are used to judge the possible renewable-energy contribution of a design option. The effective-efficiency approach embedded in the proposed model helps reduce the risk of overstated PV generation from nominal or fixed-efficiency assumptions, while remaining compatible with limited early-stage input data. In this sense, MSM is best understood as an early-stage comparison model. It keeps the main geometry, temperature, and efficiency assumptions visible across cases, but it does not replace detailed PV system design.

4.4. Scope and Limitations

This study evaluates the proposed model within a controlled cross-tool and cross-model comparison under aligned input assumptions. The results therefore describe the comparative behavior of the proposed model in the tested early-stage assessment setup. The reported values are case-specific benchmark results for the defined simulation conditions. Directly comparable measured datasets for the tested PVSD and STPV configurations were not identified; therefore, the reported annual yields are benchmark-based simulation results, not measurement-validated performance values.

For PVSDs, the comparison is limited to the tested horizontal and vertical louver configurations. These configurations include the defined louver depth, spacing, and angle variants, together with the selected South and East façade orientations and three shading-complexity levels. The exact annual simulated-yield values are therefore specific to the tested louver typologies, depth-to-spacing ratio, angular variants, façade orientations, and urban context. Other louver geometries, slat depths, spacing values, façade offsets, operable states, electrical layouts, climates, or urban morphologies may produce different self-shading and context-shading patterns.

This matters especially for slat depth and spacing, because their ratio controls the density of the louver field and therefore the potential for mutual self-shading. Closer spacing, larger depth-to-spacing ratios, or certain angle–spacing combinations can increase self-shading and reduce PV yield, while wider spacing or fewer slats can reduce self-shading. A separate sensitivity analysis of these geometric parameters was not performed because the objective was to compare PV-yield model behavior under a controlled louver geometry rather than optimize PVSD design.

For PVSD, the NOCT-based temperature estimate is an early-stage operating-temperature approximation, because it does not resolve louver-specific ventilation, rear heat transfer, or local wind effects. However, the results still indicate that louver self-shading and urban-context shading are relevant factors for early-stage PVSD yield assessment.

For the STPV cases, the analysis is based on one a-Si STPV window configuration and one double-glazing construction. Other STPV technologies, optical properties, efficiencies, and glazing constructions could change the magnitude of cell-temperature and coupling effects. They may also change how strongly cell-temperature estimation affects annual PV-yield predictions, because temperature coefficient, nominal efficiency, absorptance, layer position, and glazing-stack composition influence the link between glazing temperature,

effective efficiency, and electricity generation. This is particularly relevant because the low nominal efficiency and weak temperature sensitivity of the tested a-Si case limit both the temperature-related yield effect and the observed coupling effect.

Within this STPV scope, the STPV cell-temperature assessment remains approximate. In the proposed model, STPV cell temperature is derived from the EnergyPlus window heat-balance solution. This keeps the temperature basis consistent with the simulated glazing behavior, but the heat-balance-based approach also depends on the reconstructed inner-face temperature of the exterior STPV laminate. This reconstructed temperature is not directly reported by EnergyPlus and therefore represents the main additional approximation in the STPV temperature workflow. The approach also does not resolve a separate PV-layer thermal node, PV-layer thermal mass, or product-specific PV-layer heat balance. The verification check in Appendix D supports the numerical consistency of this reconstruction, but it confirms implementation consistency rather than measured accuracy.

The reported STPV cell temperatures serve as workflow-consistent inputs for comparing the tested formulations. They describe the selected modeling workflow, not measured product behavior. The observed differences in effective efficiency and annual PV yield therefore show the sensitivity of the workflow to the selected temperature basis. This distinction is important when transferring the findings to other STPV products, because PV-layer position, laminate design, frame-edge thermal effects, and transient PV-layer behavior could change the actual cell temperature and therefore the temperature modifier.

The NOCT-based variant adds a further limitation, because it applies an additional irradiance-dependent temperature increase to a glazing-temperature basis that has already been obtained from the window heat-balance calculation. This explains why the NOCT-based variant produces higher calculated cell temperatures than the heat-balance-based approach. The higher temperatures result from applying the NOCT term to a glazing temperature that has already been simulated. They do not represent an independently resolved STPV cell-temperature calculation.

A further scope boundary concerns the simplified representation of electrical-system losses. Detailed electrical layout and component-level system behavior are not resolved because product selection, cell layout, module interconnection, bypass-diode behavior, stringing, wiring losses, mismatch-sensitive effects, and inverter configuration are typically not yet defined at this stage. The empirical system-loss factor standardizes aggregate non-geometric losses across workflows, but it is not a substitute for electrical-layout modeling.

For PVSD, this limitation is particularly relevant because non-uniform irradiance across louvers may produce stringing- and mismatch-dependent losses that vary with the electrical connection scheme and cannot be represented by a single multiplicative factor. The PVSD results are geometry-aware early-stage yield estimates under aligned system-loss assumptions. They are not detailed predictions of final electrical-system performance. These effects remain outside the early-stage scope of this comparison and should be addressed in future work through electrical-layout and mismatch-sensitive PV modeling.

In addition, the sensitivity of the results to AOI coefficients, NOCT assumptions, temperature coefficients, and derate/loss factors was not systematically assessed in this study.

Finally, the study uses one building and context setup with one set of envelope and construction assumptions. This provides a consistent basis for comparing model behavior, but the resulting annual simulated-yield values remain case-specific. The selected climates and façade orientations are controlled reference conditions for evaluating model behavior across selected European climate and exposure contrasts. They do not provide a statistical representation of the European office-building stock. The selected additional climate-

transferability checks extend the tested boundary conditions for selected Level 0 PVSD and STPV yield comparisons, but they do not replace systematic multi-climate validation.

4.5. Future Research Directions

Future work should first include measurement-based validation for PVSD and STPV applications under comparable technology, geometry, climate, and reporting conditions, so that the cross-tool consistency shown here can be tested against observed PV output under measured shading, temperature, and operating conditions. For STPVs, measured laminate or PV-layer temperatures would be particularly useful for assessing how closely the heat-balance-based temperature estimate represents the actual thermal state of the embedded PV-active material across different climatic boundary conditions.

Second, the PV modeling scope should be expanded. This should include a systematic sensitivity analysis of AOI coefficients, NOCT assumptions, temperature coefficients, and derate/loss factors to quantify the uncertainty associated with these fixed modeling inputs. For PVSDs, this includes electrical layout, mismatch, stringing, inverter behavior, wiring losses, and broader louver geometry parameters such as slat depth, spacing, façade distance, and operable states. For STPVs, future work should improve PV cell-temperature representation within glazing assemblies and test a wider range of technologies, including higher-efficiency semi-transparent photovoltaic products.

Third, the relationship between the PV yield and building performance should be investigated more comprehensively. This is especially relevant for STPV windows, where solar–optical, thermal, and electrical effects are linked through the glazing system. Although this paper focuses on the PV yield, future studies should assess whether the same modeling assumptions affect cooling loads, indoor surface temperatures, daylight availability, and comfort.

5. Conclusions

This study developed and evaluated a PV-yield assessment model for transparent-envelope BIPV applications in early-stage building design. The proposed model replaces the fixed-efficiency input of the EnergyPlus Simple model (SM) with a time-varying effective-efficiency formulation that accounts for angle-of-incidence (AOI) reflection effects and temperature-related losses. The MSM therefore provides an intermediate approach between fixed-efficiency early-stage estimates and more detailed PV design models: it retains the limited input requirements and building-simulation compatibility of the EnergyPlus Simple model while adding AOI- and temperature-related efficiency effects that are otherwise missing from fixed-efficiency yield estimates. The selected climate checks for Trondheim and Malaga further showed that the MSM remained sensitive to climate-related changes in absolute annual yield while keeping a similar relative position among the compared models. This suggests that the MSM can be interpreted as a comparative early-stage model beyond the primary Turin case, within the limits of the tested climate set.

For PVSD applications, the results show that PV-conversion losses should be considered, but shading representation had a stronger effect than these losses in the tested cases. Under unshaded conditions, MSM remained close to the EnergyPlus Equivalent One-Diode model (EODM), while fixed-efficiency approaches gave higher yields. Once louver self-shading and urban-context shading were introduced, assessed PV yield changed substantially. PVSD yield estimates should therefore include the louver geometry and the surrounding shading context when these conditions are relevant to the design case.

For STPV windows, PV cell-temperature representation had the clearest effect among the tested STPV modeling choices. The heat-balance-based approach was therefore selected because it is better aligned with the EnergyPlus glazing heat balance than the adapted

NOCT-based variant. By contrast, the tested coupling formulation had only a limited effect on annual simulated yield for the selected low-efficiency a-Si window. The relative importance of temperature and coupling effects may change for other STPV technologies or glazing configurations, especially for higher-efficiency systems.

Within this scope, the proposed model can be used for comparative early-stage PV-yield assessment of transparent-envelope BIPV applications. This matters in early design, where architects and designers often need to compare BIPV placement, orientation, inclination, shading configuration, and system type before detailed product and electrical-system data are available. Because MSM is implemented in the same building-performance simulation environment, PVSD and STPV alternatives can be compared using the same geometry and boundary conditions as the building model. This reduces the risk of overstating PV yield compared with fixed-efficiency estimates, while keeping the assessment usable before detailed product and electrical-system data are available. Detailed electrical layout and component-level losses remain outside this early-stage scope and are represented through an empirical system derate factor.

Future work should extend the comparison with measured BIPV data, sensitivity analyses of key input parameters, broader climate and PVSD geometry sets, additional STPV technologies and glazing configurations, and later-stage electrical-layout modeling. Overall, MSM is best suited for comparative PV-yield assessment during early design, when geometry and system options can still change and detailed PV-system inputs are not yet fixed.

Author Contributions: Conceptualization, D.K., F.F., A.R. and G.L.C.; methodology, D.K., F.F., A.R. and G.L.C.; software, D.K., A.R. and G.L.C.; validation, D.K., F.F., A.R. and G.L.C.; formal analysis, D.K.; investigation, D.K.; resources, F.F. and A.R.; data curation, D.K.; writing—original draft preparation, D.K.; writing—review and editing, F.F. and G.L.C.; visualization, D.K.; supervision, F.F., A.R. and G.L.C.; project administration, F.F. All authors have read and agreed to the published version of the manuscript.

Funding: This research received no external funding.

Data Availability Statement: The original contributions presented in this study are included in the article. Further inquiries can be directed to the corresponding author.

Conflicts of Interest: The authors declare no conflicts of interest.

Abbreviations

The following abbreviations are used in this manuscript:

AOI	Angle of incidence
a-Si	Amorphous silicon
BIPV	Building-integrated photovoltaics
BPS	Building performance simulation
EMS	Energy Management System
EODM	EnergyPlus Equivalent One-Diode Model
EPBD	Energy Performance of Buildings Directive
HVAC	Heating, ventilation, and air conditioning
KPI	Key performance indicator
LBT	Ladybug Tools
m-Si	Monocrystalline silicon
MSM	EnergyPlus Modified Simple Model
NOCT	Nominal operating cell temperature
NZEB	Nearly zero-energy building
POA	Plane of array

PV	Photovoltaic
PVGIS	Photovoltaic Geographical Information System
PVSD	Photovoltaic shading device
SHGC	Solar heat gain coefficient
SM	EnergyPlus Simple model
STC	Standard test conditions
STPV	Semi-transparent photovoltaic
TMY	Typical meteorological year
ZEB	Zero-emission building

Appendix A. EnergyPlus Model Inputs

This appendix reports the EnergyPlus input assumptions used in the simulation setup. Table A1 summarizes the base operational inputs, including internal loads, ventilation, natural ventilation, thermostat setpoints, and HVAC availability.

Table A1. Operational, load, ventilation, setpoint, and system assumptions used in the EnergyPlus simulations.

Category	Parameter	Value	Unit/Note
Zone Loads	Occupancy Density	0.0565	people/m^2
	Occupant Activity Level	120	W/person; constant schedule
	Equipment Power Density	10.33	W/m^2
	Lighting Power Density	10.55	W/m^2
Ventilation and Infiltration	Infiltration Design Flow Rate	0.0002266	m^3/s per m^2 façade
	Outdoor Air Method	Sum	per person + per area
	Design Ventilation Air Flow Rate per Person	0.00236	m^3/s per person
	Design Ventilation Air Flow Rate per Area	0.000305	$m^3/s{\cdot}m^2$
Natural Ventilation	Opening Model	Wind- and stack-driven opening area	-
	Opening Area per Modeled STPV Zone	2.355	m^2
	Opening Schedule	Always on	-
	Minimum/Maximum Indoor Temperature	20/26	°C
	Minimum/Maximum Outdoor Temperature	20/30	°C
	Minimum Indoor–Outdoor Temperature Difference	1.0	°C
	Maximum Wind Speed	40.0	m/s
Setpoints and Control	Heating/Heating Setback	21/16	°C
	Cooling/Cooling Setback	26/30	°C
	Electrical Lighting Dimming Setpoint	300	lux
Systems	HVAC System Type	Ideal Loads Air System	-
	Heating Availability, Turin Case	1 January–15 April; 15 October–31 December	-
	Cooling Availability, Turin Case	16 April–14 October	-
	Heating and Cooling Availability, Additional Climate Cases	Always on	-

Appendix B. PV-Yield Model Input Parameters

Appendix B summarizes the main PV-yield model input parameters used in the comparative analyses. Appendix B.1 reports the common technology, correction, area, and loss assumptions applied in the MSM and post-processing. Appendix B.2 reports the additional electrical and thermal input parameters required for the EnergyPlus Equivalent One-Diode Model (EODM).

Appendix B.1. Common PV-Yield Assumptions Used in the Comparative Workflow

Table A2 summarizes the common numerical assumptions used for the MSM and for post-processing the PV-yield outputs. These parameters define the PV technology assumptions, effective-efficiency correction inputs, active-area assumption, and system-loss factor used across the comparative analyses. The last column indicates where each parameter is defined in the main text.

Table A2. Common PV-yield model assumptions used in the MSM and post-processing workflow.

Parameter Group	Parameter	Value	Applies to	Main Text Location
PV Technology	Nominal m-Si PV Efficiency	18%	PVSD	Section 2.3.1
PV Technology	Nominal a-Si PV Efficiency	3.6%	STPV	Section 2.3.2
Temperature Correction	m-Si Temperature Coefficient	$-0.004\ ^{\circ}C^{-1}$	PVSD	Section 2.2.2
Temperature Correction	a-Si Temperature Coefficient	$-0.002\ ^{\circ}C^{-1}$	STPV	Section 2.2.2
AOI Correction	Martin–Ruiz Angular-Loss Coefficient	$a_r = 0.17$	PVSD, STPV	Section 2.2.1
Cell-Temperature Assessment	Nominal Operating Cell Temperature	45 °C	PVSD; STPV NOCT Variant	Section 2.2.2
PV Area Assumption	Active-Area Fraction	0.90	PVSD, STPV	Section 2.4
System Losses	System Derate Factor	0.85	PVSD, STPV	Section 2.4

Appendix B.2. Input Parameters for the Equivalent One-Diode Model

Table A3 reports the additional input parameters used for the EnergyPlus Equivalent One-Diode Model (EODM). These parameters are specific to the EODM simulations and are therefore reported separately from the common MSM and post-processing assumptions in Table A2. Values are provided for both photovoltaic technologies considered in the EODM-based comparison: the monocrystalline-silicon (m-Si) configuration used for the PVSD analysis, and the amorphous-silicon (a-Si) configuration used for the STPV analysis.

Table A3. Equivalent one-diode model input parameters for the m-Si PVSD and a-Si STPV configurations.

Input Parameter	Unit	m-Si PVSD	a-Si STPV
Cell type	–	Crystalline Silicon	Amorphous Silicon
Number of cells in series	–	36	50
Active area	m^2	1	2.62
Transmittance–absorptance product	–	Not specified	
Semiconductor bandgap	eV	1.12	
Shunt resistance	Ω	1,000,000	
Short-circuit current	A	11.04	3.87
Open-circuit voltage	V	21.6	45
Reference temperature	°C	25	
Reference insolation	W/m^2	1000	
Module current at maximum power	A	10.42	3.03
Module voltage at maximum power	V	17.28	31.05
Temperature coefficient of short-circuit current	A/K	0.005	0.003
Temperature coefficient of open-circuit voltage	V/K	−0.075	−0.126
NOCT test ambient temperature	°C	20	
NOCT test cell temperature	°C	45	
NOCT test insolation	W/m^2	800	
Module heat loss coefficient	W/m^2K	30	
Total heat capacity	J/m^2K	50,000	

Appendix C. Additional Cross-Tool and Modeling-Choice Comparison Results

Appendix C provides additional numerical results for the PVSD and STPV analyses. These results complement the relative results discussed in the main text by providing the underlying absolute annual and monthly values. The appendix also includes the selected Level 0 PVSD climate-transferability results and the STPV cross-model climate comparison.

Appendix C.1. Absolute PV Yield Results for PVSD Cross-Tool Comparison

Tables A4–A6 report the absolute annual PV-yield results for the PVSD cross-tool comparison across the three geometry levels. The tables provide the numerical basis for the relative model differences and geometry-level effects discussed in Section 3.1.

Table A4. Absolute annual PV yield results in kWh/m^2·y for PVSD configurations at Level 0.

		Tilt/Rotation Angle [°]	E+ Simple Model L0	E+ Simple Model Modified L0	E+ Equivalent One-Diode Model L0	Ladybug Tools L0	PVGIS (L0)
Horizontal Louvers	East	0	230.05	207.47	214.30	228.91	188.83
		15	236.01	213.57	220.25	234.34	185.68
		30	234.30	212.70	218.89	231.81	179.19
		45	224.03	204.40	209.60	223.58	168.77
		60	210.80	192.92	197.49	209.18	153.34
		75	190.55	175.06	178.76	189.18	133.24
		90	165.91	152.76	155.72	163.70	109.38
	South	0	229.98	207.42	214.17	228.91	188.83
		15	262.43	238.80	244.82	261.31	214.50
		30	281.87	256.97	263.14	280.53	228.60
		45	283.80	259.56	265.32	284.45	230.96
		60	273.10	250.22	255.94	273.38	221.53
		75	246.09	225.79	231.43	247.58	200.34
		90	206.49	188.75	194.82	209.12	167.53
Vertical Louvers	East	−90	165.91	152.76	155.71	163.70	109.47
		−75	184.15	169.84	173.36	183.37	124.69
		−60	198.48	183.12	187.27	198.52	139.49
		−45	208.27	191.90	196.84	209.16	151.14
		−30	212.69	195.47	201.21	213.70	160.33
		−15	211.54	193.80	200.01	213.92	165.74
		0	206.46	188.72	194.85	209.12	167.34
	South	−90	165.83	152.69	155.59	163.70	109.47
		−75	184.10	169.79	173.25	183.37	124.69
		−60	198.45	183.09	187.18	198.52	139.49
		−45	208.27	191.90	196.78	209.16	151.14
		−30	212.69	195.47	201.14	213.70	160.33
		−15	211.54	193.80	199.95	213.92	165.74
		0	206.50	188.76	194.83	209.12	167.34
		15	198.79	181.69	186.95	200.91	165.99
		30	188.22	172.10	176.26	189.00	161.10
		45	174.94	160.15	162.99	175.88	152.77
		60	160.00	146.50	148.38	160.05	140.75
		75	143.59	131.44	132.50	142.84	127.16
		90	126.19	115.19	115.75	123.94	110.20

Table A5. Absolute annual PV yield results in kWh/m^2·y for PVSD configurations at Level 1.

		Tilt/Rotation Angle [°]	E+ Simple Model L1	E+ Simple Model Modified L1	Ladybug Tools L1	PVGIS (L0)
Horizontal Louvers	East	0	160.46	147.46	159.12	188.83
		15	180.84	167.57	180.58	185.68
		30	193.83	179.25	193.15	179.19
		45	198.57	182.89	198.99	168.77
		60	198.50	180.72	198.42	153.34
		75	187.37	169.90	185.98	133.24
		90	165.90	147.47	163.70	109.38
	South	0	202.10	183.98	194.68	188.83
		15	233.57	215.26	228.56	214.50
		30	254.45	234.43	252.41	228.60
		45	262.74	241.55	266.00	230.96
		60	261.65	238.82	262.86	221.53
		75	244.17	221.87	246.13	200.34
		90	206.50	184.66	209.12	167.53
Vertical Louvers	East	−90	165.90	150.49	163.70	109.47
		−75	180.80	165.00	178.39	124.69
		−60	185.07	169.84	185.91	139.49
		−45	182.59	168.04	181.36	151.14
		−30	166.84	153.15	173.47	160.33
		−15	148.60	135.64	159.26	165.74
		0	125.87	114.27	140.47	167.34
	South	−90	113.59	103.48	115.99	109.47
		−75	136.23	124.74	137.27	124.69
		−60	157.70	144.85	161.81	139.49
		−45	181.12	166.57	182.67	151.14
		−30	196.79	180.69	201.88	160.33
		−15	207.21	189.30	210.06	165.74
		0	206.50	187.87	209.12	167.34
		15	196.00	178.40	198.25	165.99
		30	177.85	162.03	181.35	161.10
		45	157.63	143.74	158.24	152.77
		60	134.27	121.87	135.57	140.75
		75	113.21	102.25	111.94	127.16
		90	92.29	82.56	91.16	110.20

Table A6. Absolute annual PV yield results in kWh/m^2·y for PVSD configurations at Level 2.

		Tilt/Rotation Angle [°]	E+ Simple Model L2	E+ Simple Model Modified L2	Ladybug Tools L2	PVGIS (L0)
Horizontal Louvers	East	0	99.66	92.16	93.03	188.83
		15	117.63	109.83	112.98	185.68
		30	130.25	121.78	126.54	179.19
		45	136.69	127.61	134.26	168.77
		60	136.76	127.30	137.21	153.34
		75	128.90	119.27	129.56	133.24
		90	108.56	99.36	111.32	109.38

Table A6. *Cont.*

		Tilt/Rotation Angle [°]	E+ Simple Model L2	E+ Simple Model Modified L2	Ladybug Tools L2	PVGIS (L0)
Horizontal Louvers	South	0	164.30	151.23	151.02	188.83
		15	188.22	174.96	176.19	214.50
		30	203.72	189.63	194.58	228.60
		45	209.52	194.78	206.44	230.96
		60	206.03	190.95	203.07	221.53
		75	190.30	175.38	189.34	200.34
		90	153.23	139.59	156.25	167.53
Vertical Louvers	East	−90	108.94	99.68	111.65	109.47
		−75	121.76	112.92	124.71	124.69
		−60	123.98	116.02	126.48	139.49
		−45	119.87	112.62	120.15	151.14
		−30	111.14	104.33	108.11	160.33
		−15	97.26	90.73	93.53	165.74
		0	80.54	74.12	74.25	167.34
	South	−90	81.66	74.54	74.26	109.47
		−75	97.71	89.87	94.91	124.69
		−60	114.09	105.16	113.20	139.49
		−45	129.11	119.09	132.01	151.14
		−30	142.23	131.20	144.13	160.33
		−15	152.71	140.27	155.70	165.74
		0	153.33	139.70	155.93	167.34
		15	144.76	132.47	147.27	165.99
		30	130.25	119.37	131.49	161.10
		45	114.86	105.06	116.38	152.77
		60	99.27	90.63	97.12	140.75
		75	83.76	76.27	79.23	127.16
		90	68.91	62.00	60.29	110.20

Appendix C.2. Additional STPV Results

Appendix C.2 reports monthly STPV results for the modeling-choice and cross-model comparisons. Table A7 provides monthly PV cell temperature, effective efficiency, and PV yield values for the tested temperature-calculation approaches and coupling formulations. The heat-balance-based decoupled case corresponds to the selected MSM configuration used in the cross-model comparison in Table A8. Table A8 reports the monthly PV-yield comparison between the SM, the selected MSM model configuration, and the EODM.

Table A7. Monthly STPV cell temperature (°C), effective efficiency (%), and PV yield (kWh/m^2·m) by orientation, cell temperature approach, and coupling formulation.

	East				South			
	Heat Balance Approach		NOCT Approach		Heat Balance Approach		NOCT Approach	
	Coupled	Decoupled	Coupled	Decoupled	Coupled	Decoupled	Coupled	Decoupled
Cell Temperature								
Jan	16.06	16.38	18.96	19.22	23.00	23.78	28.39	28.99
Feb	19.49	19.83	22.82	23.24	28.85	29.76	37.30	38.21
Mar	21.96	22.35	26.15	26.60	27.52	28.26	35.29	36.04
Apr	22.88	23.24	27.47	27.82	23.02	23.63	28.59	28.94
May	23.97	24.35	28.27	28.63	22.36	22.66	26.84	27.14
Jun	23.83	24.20	28.32	28.67	21.33	21.52	24.64	24.94

Table A7. *Cont.*

	East				South			
	Heat Balance Approach		NOCT Approach		Heat Balance Approach		NOCT Approach	
	Coupled	Decoupled	Coupled	Decoupled	Coupled	Decoupled	Coupled	Decoupled
Jul	24.74	25.11	29.16	29.57	22.71	23.08	26.46	26.74
Aug	25.68	26.03	30.17	30.60	26.36	27.05	32.46	32.96
Sept	25.60	25.95	29.64	29.99	31.86	32.65	41.47	42.23
Oct	23.71	24.07	27.55	27.85	31.81	32.56	41.61	42.42
Nov	21.15	21.60	24.57	24.94	31.14	32.09	41.68	42.68
Dec	17.54	17.80	20.13	20.42	29.30	30.24	38.30	39.20
Effective Efficiency								
Jan	3.41%	3.41%	3.40%	3.40%	3.41%	3.41%	3.32%	3.31%
Feb	3.41%	3.41%	3.39%	3.38%	3.36%	3.35%	3.27%	3.26%
Mar	3.41%	3.40%	3.37%	3.37%	3.30%	3.29%	3.19%	3.18%
Apr	3.40%	3.40%	3.36%	3.36%	3.25%	3.24%	3.15%	3.14%
May	3.40%	3.40%	3.37%	3.37%	3.19%	3.18%	3.13%	3.13%
Jun	3.40%	3.39%	3.36%	3.36%	3.13%	3.13%	3.09%	3.08%
Jul	3.40%	3.40%	3.36%	3.36%	3.12%	3.12%	3.09%	3.09%
Aug	3.38%	3.38%	3.34%	3.33%	3.15%	3.15%	3.08%	3.07%
Sept	3.39%	3.39%	3.36%	3.36%	3.24%	3.23%	3.13%	3.12%
Oct	3.39%	3.39%	3.35%	3.35%	3.32%	3.31%	3.21%	3.20%
Nov	3.41%	3.41%	3.39%	3.39%	3.38%	3.37%	3.28%	3.27%
Dec	3.41%	3.41%	3.39%	3.39%	3.40%	3.39%	3.28%	3.27%
PV Yield								
Jan	0.92	0.92	0.92	0.92	3.20	3.20	3.20	3.12
Feb	1.49	1.48	1.49	1.46	3.09	3.08	3.09	3.00
Mar	1.78	1.78	1.78	1.75	3.29	3.29	3.29	3.20
Apr	2.46	2.45	2.46	2.40	3.06	3.06	3.06	3.00
May	2.98	2.97	2.98	2.91	2.21	2.21	2.21	2.17
Jun	2.58	2.58	2.58	2.52	2.08	2.08	2.08	2.05
Jul	2.96	2.96	2.96	2.90	2.30	2.30	2.30	2.26
Aug	3.13	3.12	3.13	3.05	2.79	2.78	2.79	2.73
Sept	1.95	1.95	1.95	1.91	3.14	3.13	3.14	3.04
Oct	1.26	1.26	1.26	1.24	2.83	2.82	2.83	2.74
Nov	1.18	1.18	1.18	1.16	2.84	2.84	2.84	2.75
Dec	1.13	1.13	1.13	1.12	3.24	3.23	3.24	3.14

Table A8. Monthly STPV PV yield comparison between the E+ Simple model, E+ modified Simple model (heat-balance approach, decoupled), and EODM (kWh/m^2·m).

	East			South		
	E+ Simple Model	E+ Modified Simple Model	EOD Model	E+ Simple Model	E+ Modified Simple Model	EOD Model
Jan	1.00	0.92	0.61	3.44	3.20	2.94
Feb	1.60	1.48	1.18	3.30	3.08	2.79
Mar	1.93	1.78	1.32	3.60	3.29	2.87
Apr	2.66	2.45	1.86	3.41	3.06	2.50
May	3.22	2.97	2.30	2.53	2.21	1.60
Jun	2.83	2.58	1.79	2.45	2.08	1.44
Jul	3.22	2.96	2.11	2.70	2.30	1.61
Aug	3.42	3.12	2.42	3.19	2.78	2.09
Sept	2.13	1.95	1.34	3.49	3.13	2.51
Oct	1.38	1.26	0.83	3.07	2.82	2.32
Nov	1.28	1.18	0.89	3.05	2.84	2.54
Dec	1.22	1.13	0.82	3.43	3.23	2.90

Appendix C.3. Additional PVSD Climate-Transferability Results

Tables A9 and A10 report the selected Level 0 PVSD climate-transferability results for Trondheim, Turin, and Malaga. The comparison is limited to the four selected configurations used in the additional analysis: horizontal louvers East 90°, horizontal louvers South 60°, vertical louvers East −90°, and vertical louvers South −90°.

Table A9. Absolute annual PV yield results in kWh/m^2 · y for selected Level 0 PVSD configurations across Trondheim, Turin, and Malaga.

System Orientation	Orientation	Tilt Angle	Azimuth Angle	Tool	Trondheim	Turin	Malaga
Horizontal	East	90	−90	E+_SM	86.49	165.96	193.01
				E+_MSM	81.48	152.80	176.62
				E+_EODM	81.56	155.77	177.75
				LBT	86.22	163.69	193.13
				PVGIS	66.82	109.38	137.25
Horizontal	South	60	0	E+_SM	135.69	273.28	305.63
				E+_MSM	127.89	250.38	280.86
				E+_EODM	129.47	256.10	281.26
				LBT	137.86	273.38	306.32
				PVGIS	127.77	221.53	266.85
Vertical	East	90	−90	E+_SM	86.49	165.96	193.01
				E+_MSM	81.48	152.80	176.62
				E+_EODM	81.56	155.77	177.75
				LBT	86.22	163.69	193.13
				PVGIS	66.82	109.38	137.25
Vertical	South	90	−90	E+_SM	86.41	165.89	192.93
				E+_MSM	81.41	152.73	176.55
				E+_EODM	81.46	155.64	177.62
				LBT	86.22	163.69	193.13
				PVGIS	66.82	109.38	137.25

Table A10. Relative differences in annual PV yield relative to the EnergyPlus modified Simple model for selected Level 0 PVSD configurations across Trondheim, Turin, and Malaga.

System Orientation	Orientation	Azimuth Angle	Tilt Angle	Tool	Trondheim	Turin	Malaga
Horizontal	East	−90	90	E+ SM	6.14%	8.61%	9.28%
				E+ EODM	0.09%	1.94%	0.64%
				LBT	5.81%	7.13%	9.35%
				PVGIS	−18.00%	−28.42%	−22.29%
Horizontal	South	0	60	E+ SM	6.14%	8.61%	9.28%
				E+ EODM	0.09%	1.94%	0.64%
				LBT	5.81%	7.13%	9.35%
				PVGIS	−18.00%	−28.42%	−22.29%
Vertical	East	−90	90	E+ SM	6.10%	9.15%	8.82%
				E+ EODM	1.23%	2.28%	0.14%
				LBT	7.79%	9.19%	9.07%
				PVGIS	−0.10%	−11.52%	−4.99%

Table A10. *Cont.*

System Orientation	Orientation	Azimuth Angle	Tilt Angle	Tool	Trondheim	Turin	Malaga
Vertical	South	−90	90	E+ SM	6.14%	8.61%	9.28%
				E+ EODM	0.05%	1.90%	0.60%
				LBT	5.91%	7.18%	9.39%
				PVGIS	−17.92%	−28.39%	−22.26%

Appendix C.4. Additional STPV Climate-Transferability Results

Appendix C.4 reports the additional STPV cross-model climate comparison for the selected heat-balance-based decoupled MSM configuration, SM, and EODM. Results are provided for East and South orientations in Trondheim, Turin, and Malaga.

Table A11. Absolute annual STPV PV yield results in kWh/m^2 · y across EnergyPlus model configurations, orientations, and climate locations.

Orientation	Model	Trondheim	Turin	Malaga
East	E+ SM	17.14	25.90	38.39
	E+ MSM	15.92	23.47	34.35
	E+ EODM	11.42	17.45	28.46
South	E+ SM	21.84	37.66	43.21
	E+ MSM	20.31	34.08	39.16
	E+ EODM	15.59	28.13	32.36

Table A12. Relative differences in annual STPV PV yield relative to the EnergyPlus modified Simple model across EnergyPlus model configurations, orientations, and climate locations.

Orientation	Model	Trondheim	Turin	Malaga
East	E+ SM	7.63%	10.36%	11.76%
	E+ EODM	−28.26%	−25.63%	−17.15%
South	E+ SM	7.52%	10.50%	10.33%
	E+ EODM	−23.26%	−17.46%	−17.36%

Appendix D. STPV Glazing Temperature Reconstruction Verification

Appendix D reports a cross-software consistency check for the reconstructed inner-face temperature of the exterior STPV laminate, θ_2, used in the heat-balance-based STPV cell-temperature approach. The check compares EnergyPlus-reconstructed θ_2 values with corresponding glazing-node temperatures calculated in WINDOW 8.1 under selected matched boundary conditions. Because both values come from simulation tools, the check verifies implementation consistency rather than empirical accuracy.

The check was performed for a South-facing STPV window with the same properties as described in Section 2.3.2. The Turin weather file used in the main cross-tool comparison was also used here. Three representative days were selected to cover winter, equinox-period, and summer boundary conditions: 15 January, 30 March, and 31 July. For each day, five hourly conditions were evaluated at 9:00, 11:00, 13:00, 15:00, and 17:00, resulting in a total of 15 comparison points. The transferred EnergyPlus outputs included outdoor, sky, indoor air, and mean radiant temperatures; incident solar radiation; interior and exterior convective heat-transfer coefficients; and the relevant glazing temperatures T1,

T4, and reconstructed T2. Here, T1 and T2 denote the corresponding software-specific temperature-node identifiers for the mathematical variables θ_1 and θ_2, respectively.

The temperature-node notation is defined as follows. T1/θ_1 denotes the exterior surface temperature of the STPV laminate. T2/θ_2 denotes the inner-face temperature of the STPV laminate; in EnergyPlus, this value is reconstructed through EMS from the exterior glazing heat balance, while in WINDOW it is obtained directly as the corresponding glazing-node temperature. T4/θ_4 denotes the inner surface temperature of the inner glazing layer. The STPV double-glazing unit was modeled in WINDOW using the same layer sequence as the EnergyPlus STPV construction, and 15 corresponding environmental cases were created from the exported EnergyPlus boundary-condition outputs.

Table A13 reports the EnergyPlus boundary conditions used to define the matched WINDOW environmental cases.

Table A13. EnergyPlus boundary conditions used to define the matched WINDOW environmental cases for the STPV temperature-reconstruction verification check.

Hour	Indoor Temperature [°C]	Convective Heat Transfer Coefficient Inside [W/m^{2}K]	Mean Radiant Temperature [°C]	Outdoor Temperature [°C]	Solar Radiation [W/m^2]	Convective Heat Transfer Coefficient Outside [W/m^{2}K]	Sky Temperature [°C]
			01/15				
09:00	17.65	1.56	19.21	−0.42	5.02	1.80	−16.74
11:00	17.61	1.27	19.10	0.35	39.47	2.20	−7.43
13:00	17.52	1.28	18.96	0.88	38.05	3.19	−4.44
15:00	17.40	1.22	18.83	0.96	49.95	4.46	−3.82
17:00	17.33	0.65	18.75	1.06	93.94	3.88	−7.20
			03/30				
09:00	23.94	1.24	24.45	10.00	194.37	6.56	−2.51
11:00	24.00	1.90	25.04	16.07	451.25	7.20	−0.10
13:00	22.66	2.05	25.19	21.58	534.69	14.05	1.49
15:00	22.68	2.06	25.46	21.42	581.34	13.38	1.07
17:00	24.01	1.75	25.38	20.00	303.54	8.59	−0.33
			07/31				
09:00	24.00	1.63	24.48	24.75	194.06	2.50	8.54
11:00	24.00	2.13	25.16	30.17	444.06	3.63	11.93
13:00	24.00	2.26	25.69	31.58	552.69	4.02	14.16
15:00	24.00	2.16	25.94	32.58	438.81	4.61	15.44
17:00	24.00	1.89	25.89	33.42	202.12	3.98	16.40

Figure A1 provides context for the selected test points by showing the solar-radiation conditions and EnergyPlus glazing-temperature behavior across the three representative days.

Table A14 reports the EnergyPlus and WINDOW glazing temperatures resulting from the comparison. Figure A2 compares the EnergyPlus-reconstructed T2/θ_2 values with the corresponding WINDOW T2/θ_2 values. Figure A3 compares the WINDOW–EnergyPlus differences for T1/θ_1 and T2/θ_2 of the exterior STPV laminate.

Table A14. EnergyPlus and WINDOW glazing temperatures in °C used for the STPV temperature-reconstruction verification check.

Day	Hour	E+			WINDOW		
		T1	T2	T4	T1	T2	T4
Jan 15	9 am	0.38	0.08	15.58	−0.70	−0.50	14.60
	11 am	5.14	5.31	16.69	1.80	2.10	15.20
	1 pm	5.24	5.65	16.61	2.50	2.80	15.30

Table A14. *Cont.*

Day	Hour	E+			WINDOW		
		T1	T2	T4	T1	T2	T4
Jan 15	3 pm	5.55	5.63	16.62	3.00	3.30	15.30
	5 pm	8.47	8.83	17.40	4.10	4.60	15.70
Mar 30	9 am	19.82	18.66	24.82	15.50	16.30	23.70
	11 am	36.99	39.13	28.79	28.80	30.20	26.70
	1 pm	37.29	38.98	28.88	35.80	37.50	26.90
	3 pm	39.21	41.69	29.73	37.00	38.80	27.30
	5 pm	31.23	32.99	27.42	27.50	28.40	25.90
Jul 31	9 am	33.89	32.33	26.69	28.90	29.50	25.60
	11 am	52.56	52.62	31.57	41.10	42.30	28.50
	1 pm	59.16	60.29	33.61	45.50	47.10	29.80
	3 pm	52.61	54.45	31.99	43.20	44.40	28.90
	5 pm	40.43	42.33	28.70	37.00	37.60	26.80

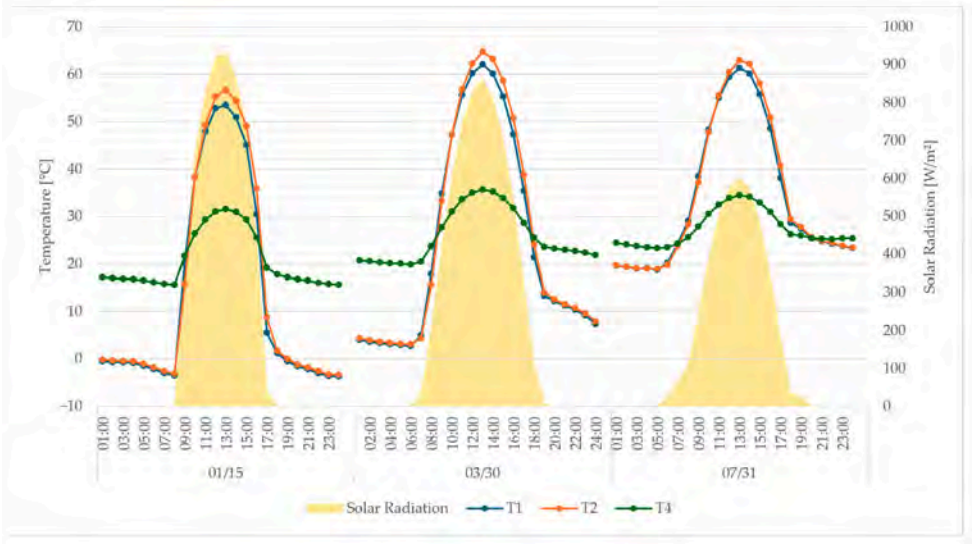

Figure A1. Selected EnergyPlus boundary conditions and glazing temperatures used for the STPV temperature-reconstruction verification check.

The comparison shows broadly similar temperature ranges and trends between the EnergyPlus reconstruction and WINDOW results. The reconstructed EnergyPlus T2/θ_2 values and the corresponding WINDOW T2/θ_2 values follow the same seasonal and irradiance-related pattern, with lower temperatures under winter low-irradiance conditions and higher temperatures under summer high-irradiance conditions. WINDOW generally gives lower T2/θ_2 values than EnergyPlus, especially during warmer and higher-irradiance cases. More importantly for the reconstruction check, the cross-tool differences for T1/θ_1 and T2/θ_2 are broadly proportional. Because T1/θ_1 is directly reported by EnergyPlus, while T2/θ_2 is reconstructed through EMS, this indicates that the remaining deviations are not specific to the reconstructed T2/θ_2 node, but reflect broader differences between the EnergyPlus and WINDOW glazing-temperature calculations.

The residual differences can be attributed mainly to differences in calculation context and solar-optical representation. EnergyPlus temperatures are extracted from a timestep-based building simulation, in which each reported hourly state is influenced by the preceding simulation sequence, including zone conditions, surface heat balances, solar gains, and convective exchange [31]. WINDOW, by contrast, evaluates each selected glazing

case under independently prescribed environmental boundary conditions [47]. Differences may also arise from how the two tools apply solar-optical properties and absorbed solar radiation under the selected boundary conditions, including the use of incidence-angle-dependent optical behavior in EnergyPlus and perpendicular-incidence optical properties in the WINDOW comparison cases used here [31,47]. The observed deviations are therefore consistent with expected cross-tool differences rather than with a separate error introduced by the EMS-based θ_2 reconstruction.

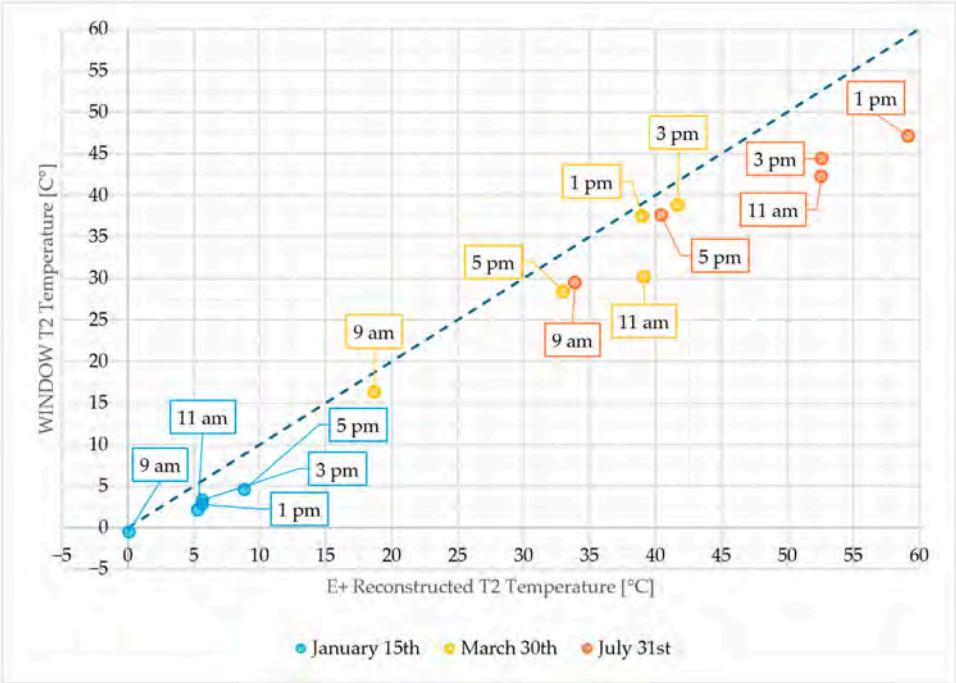

Figure A2. Comparison between EnergyPlus-reconstructed T2/θ_2 and WINDOW T2/θ_2 for selected boundary conditions. The dashed line indicates one-to-one agreement.

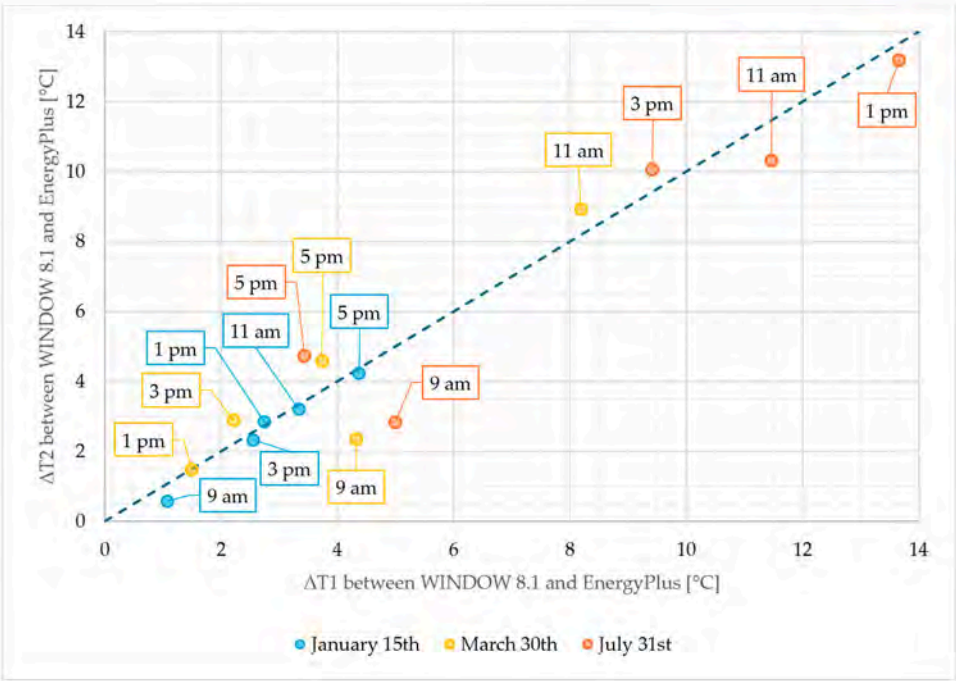

Figure A3. Cross-tool temperature differences for the exterior STPV laminate surface nodes: T1/θ_1 on the x-Axis and T2/θ_2 on the y-Axis. The dashed line indicates equal cross-tool differences.

Overall, the comparison indicates that the EMS-based θ_2 reconstruction is numerically consistent within the intended EnergyPlus workflow. The reconstructed θ_2 values follow the expected seasonal and irradiance-related behavior, and the T2/θ_2 deviations remain consistent with the directly reported T1/θ_1 deviations. The check should therefore be read as cross-tool consistency verification, not as measurement-based validation of STPV laminate or PV cell temperature.

Appendix E. EMS and IDF Implementation Logic for the MSM

Appendix E reports the EMS and IDF implementation logic used for the EnergyPlus modified Simple model (MSM). It complements the model formulation in Section 2.2 by reporting the main implementation steps for the effective-efficiency calculation, the second-run schedule-based PV object chain, the STPV cell-temperature assessment, and the coupled STPV construction-switching logic.

The code blocks are provided as annotated EMS- or IDF-style pseudocode rather than directly executable IDF extracts. Case-specific object names, file paths, and repeated identifiers are generalized for readability. The placeholder <zone> denotes the EnergyPlus zone or reporting group to which PV elements are attributed, <surface> denotes an individual PVSD louver or slat surface, and <window> denotes an individual STPV window surface.

Appendix E.1. EMS Implementation Logic for the PVSD MSM Effective-Efficiency Run

The PVSD MSM first-run EnergyPlus model uses the Energy Management System (EMS) to calculate a timestep-dependent effective PV efficiency for a representative PVSD surface. The EMS calculation reads outdoor air temperature, incident irradiance components, and beam-incidence information from EnergyPlus output variables. These inputs are used to calculate the AOI-related modifier, the NOCT-based PV cell temperature, the temperature modifier, and the final effective efficiency. The exported effective-efficiency time series from Run 1 is then used as the scheduled PV efficiency input in Run 2.

The EMS-style pseudocode reports the implemented calculation order, while replacing case-specific surface, room, and scenario identifiers with the generic suffix <surface>. It is therefore a generalized pseudocode description, not a directly executable EMS object block. The corresponding EMS calculation sequence for the PVSD MSM effective-efficiency calculation is presented in Algorithm A1.

Table A15. EMS sensor mapping for the PVSD MSM effective-efficiency run.

Generic EMS Sensor	EnergyPlus Output Variable Read by EMS	Key Value	Role in Calculation
T_o	Site Outdoor Air Drybulb Temperature	*	Outdoor air temperature
q_sol_<surface>	Surface Outside Face Incident Solar Radiation Rate per Area	Representative PVSD surface	Total incident irradiance on the PVSD surface
RadBeam_<surface>	Surface Outside Face Incident Beam Solar Radiation Rate per Area		Beam/direct irradiance on the PVSD surface
RadDiffuse_<surface>	Surface Outside Face Incident Sky Diffuse Solar Radiation Rate per Area		Sky-diffuse irradiance on the PVSD surface
RadGround_<surface>	Surface Outside Face Incident Ground Diffuse Solar Radiation Rate per Area		Ground-reflected irradiance on the PVSD surface
theta_<surface>	Surface Outside Face Beam Solar Incident Angle Cosine Value		Beam-incidence cosine used in the AOI modifier calculation

The asterisk (*) indicates a global EnergyPlus output variable with the key value "Environment"; no surface-specific key value is required.

Table A16. Constants used in the PVSD MSM effective-efficiency calculation.

EMS Variable	Value	Description
gamma	−0.004	Relative temperature coefficient for m-Si PV, equivalent to −0.4%/°C
eta_nom	0.18	Nominal PV conversion efficiency
c1	4/(3 × PI)	Martin–Ruiz diffuse and ground-reflected fitting constant
c2	−0.069	Martin–Ruiz diffuse and ground-reflected fitting constant
ar	0.17	Martin–Ruiz angular-loss coefficient
beta	<surface tilt angle>	Tilt angle of the representative PVSD surface
NOCT	45	Nominal operating cell temperature in °C

Algorithm A1. EMS-style pseudocode for the PVSD MSM effective-efficiency calculation

EMS Program 1: Constant Initialization

```
SET gamma = −0.004
SET eta_nom = 0.18
SET c1 = 4/(3 * PI)
SET c2 = −0.069
SET ar = 0.17
SET beta = <surface tilt angle>
SET NOCT = 45
```

EMS Program 2: NOCT-Based PV Cell Temperature

```
SET Tambient = T_o
SET T_PV_NOCT_<surface> = Tambient + q_sol_<surface> * (NOCT - 20)/800
```

EMS Program 3: Temperature Modifier

```
SET MTEMP_<surface> = 1 + gamma * (T_PV_NOCT_<surface> - 25)
IF MTEMP_<surface> > 1
SET MTEMP_<surface> = 1
ENDIF
```

EMS Program 4: AOI Modifier

```
SET X = @Exp (−1/ar)

IF theta_<surface> < 0
SET theta_clamp_<surface> = 0
ELSE
SET theta_clamp_<surface> = theta_<surface>
ENDIF
```

Algorithm A1. *Cont.*

```
IF (1 - X) == 0
SET LF_Beam_<surface> = 0
ELSE
SET LF_Beam_<surface> = (@Exp (-theta_clamp_<surface>/ar) - X)/(1 - X)
ENDIF

SET beta_rad_<surface> = beta * PI/180

SET Y_D_<surface> = @Sin beta_rad_<surface> + (PI - beta_rad_<surface> - @Sin
beta_rad_<surface>)/(1 + @Cos beta_rad_<surface>)

SET LF_Diffuse_<surface> = @Exp (-(1/ar) * (c1 * Y_D_<surface> + c2 * Y_D_<surface>
* Y_D_<surface>))

IF (1 - @Cos beta_rad_<surface>) == 0
SET Y_A_<surface> = 0
ELSE
SET Y_A_<surface> = @Sin beta_rad_<surface> + (beta_rad_<surface> - @Sin
beta_rad_<surface>)/(1 - @Cos beta_rad_<surface>)
ENDIF

SET LF_Ground_<surface> = @Exp (-(1/ar) * (c1 * Y_A_<surface> + c2 * Y_A_<surface>
* Y_A_<surface>))

SET Rad_<surface> = RadBeam_<surface> + RadDiffuse_<surface> +
RadGround_<surface>

IF Rad_<surface> == 0
SET MAOI_<surface> = 0
ELSE
SET MAOI_<surface> = (RadBeam_<surface> * (1 - LF_Beam_<surface>) +
RadDiffuse_<surface> * (1 - LF_Diffuse_<surface>) + RadGround_<surface> * (1 -
LF_Ground_<surface>))/Rad_<surface>
ENDIF
```

EMS Program 5: Effective Efficiency

```
SET eta_eff_<surface> = eta_nom * MTEMP_<surface> * MAOI_<surface>
```

EMS Output Variable

```
EnergyManagementSystem:OutputVariable,
eta_eff_<surface>, !- Name
eta_eff_<surface>, !- EMS Variable Name
Averaged, !- Type of Data in Variable
ZoneTimestep; !- Update Frequency
```

The exported eta_eff_<surface> output is requested at hourly frequency and used as the effective-efficiency schedule in the second EnergyPlus run.

Table A17. EMS output and program calling-point definition.

EMS Component	Implementation in the PVSD MSM First Run
Exported EMS output variable	eta_eff_<surface>
EMS output type	Averaged
EMS reporting basis	ZoneTimestep
Reported output frequency	Hourly
Use of exported output	Effective-efficiency schedule for Run 2
Constant-initialization calling point	BeginTimestepBeforePredictor
Effective-efficiency calculation calling point	EndOfZoneTimestepBeforeZoneReporting
Programs called by effective-efficiency calculation	NOCT-based PV cell temperature; temperature modifier; AOI modifier; effective efficiency

Implementation Note: The EnergyPlus EMS implementation uses one representative PVSD surface for each case to calculate the effective-efficiency time series. The same calculation structure is repeated across the relevant PVSD configurations. The placeholder <surface> denotes the case-specific identifier used in the IDF for each representative PVSD surface. The variable theta_<surface> reads the EnergyPlus beam-incidence cosine output, not the incidence angle in degrees.

Appendix E.2. PVSD MSM Second-Run Schedule-Based PV Yield Implementation

In the second EnergyPlus run of the PVSD MSM workflow the effective-efficiency time series exported from Run 1 is imported through Schedule:File objects and assigned to PhotovoltaicPerformance:Simple objects using scheduled conversion efficiency. The resulting PV performance objects are connected to the PVSD surfaces through Generator:Photovoltaic objects and linked to the EnergyPlus electric load center.

Algorithm A2 reports the second-run object chain as annotated IDF-style pseudocode. The EnergyPlus field labels after "!-" are retained to clarify the meaning of each input. Here, <zone> denotes the zone or reporting group for which the photovoltaic generators are considered, while <surface> denotes an individual PVSD generator surface that is attributed to that zone.

Algorithm A2. Annotated IDF-Style Pseudocode for the PVSD MSM Second-Run PV Object Chain

```
Step 1: Import the Run 1 Effective-Efficiency Schedule
Schedule:File,
Schedule_<zone>,    !- Name
Fractional,    !- Schedule Type Limits Name
<Run 1 effective-efficiency CSV file>,    !- File Name
<eta_eff column number>,    !- Column Number
1,    !- Rows to Skip at Top
8760,    !- Number of Hours of Data
Comma,    !- Column Separator
No,    !- Interpolate to Timestep
60,    !- Minutes per Item
Yes;    !- Adjust Schedule for Daylight Savings

Step 2: Define the Scheduled Simple PV Performance Object
PhotovoltaicPerformance:Simple,
MSM_<zone>,    !- Name
1,    !- Fraction of Surface Area with Active Solar Cells {dimensionless}
Scheduled,    !- Conversion Efficiency Input Mode
```

Algorithm A2. *Cont.*

```
    ,   !- Value for Cell Efficiency if Fixed
Schedule_<zone>;   !- Efficiency Schedule Name


Step 3: Assign a PV Generator to Each PVSD Surface
Generator:Photovoltaic,
Generator_<zone>_<surface>,   !- Name
<PVSD surface name>,   !- Surface Name
PhotovoltaicPerformance:Simple,   !- Photovoltaic Performance Object Type
MSM_<zone>,   !- Module Performance Name
Decoupled,   !- Heat Transfer Integration Mode
1,   !- Number of Series Strings in Parallel {dimensionless}
1;   !- Number of Modules in Series {dimensionless}

Step 4: Group the PV Generators of Each Case
ElectricLoadCenter:Generators,
List_<zone>,   !- Name
Generator_<zone>_<surface_1>,   !- Generator_1 Name
Generator:Photovoltaic,   !- Generator_1 Object Type
0,   !- Generator_1 Rated Electric Power Output {W}
Always On,   !- Generator_1 Availability Schedule Name
,   !- Generator_1 Rated Thermal to Electrical Power Ratio
Generator_<zone>_<surface_2>,   !- Generator_2 Name
Generator:Photovoltaic,   !- Generator_2 Object Type
0,   !- Generator_2 Rated Electric Power Output {W}
Always On,   !- Generator_2 Availability Schedule Name
,   !- Generator_2 Rated Thermal to Electrical Power Ratio
..   !- Repeated for all PVSD generators assigned to the same zone
;   !- Last Generator Rated Thermal to Electrical Power Ratio

Step 5: Define the Simple Inverter
ElectricLoadCenter:Inverter:Simple,
SimpleInverter_<zone>,   !- Name
Always On,   !- Availability Schedule Name
,   !- Zone Name
,   !- Radiative Fraction
1.00;   !- Inverter Efficiency

Step 6: Connect the Generator List to the Electric Load Center
ElectricLoadCenter:Distribution,
Distribution_<zone>,   !- Name
List_<zone>,   !- Generator List Name
Baseload,   !- Generator Operation Scheme Type
,   !- Generator Demand Limit Scheme Purchased Electric Demand Limit {W}
,   !- Generator Track Schedule Name Scheme Schedule Name
,   !- Generator Track Meter Scheme Meter Name
AlternatingCurrent,   !- Electrical Buss Type
```

Algorithm A2. *Cont.*

```
SimpleInverter_<zone>,   !- Inverter Name
,   !- Electrical Storage Object Name
,   !- Transformer Object Name
,   !- Storage Operation Scheme
,   !- Storage Control Track Meter Name
,   !- Storage Converter Object Name
1;   !- Maximum Storage State of Charge Fraction
```

Implementation Note: The second-run IDF does not include EMS programs or EMS calling managers. The PV electricity calculation is performed through the scheduled Simple PV performance objects and the EnergyPlus electric load center object chain. For each <zone>, all assigned PVSD generators use the same imported effective-efficiency schedule from Run 1. The individual Generator:Photovoltaic objects remain linked to their own PVSD surfaces, so EnergyPlus still evaluates the surface-specific incident irradiance and active surface area during Run 2. The inverter efficiency is set to 1.00 in the EnergyPlus object chain because the harmonized system derate factor is applied during post-processing, avoiding double counting of inverter or system-level losses.

Appendix E.3. STPV MSM PV Cell-Temperature Assessment in the First-Run EMS

The STPV MSM first-run EMS implementation follows the same effective-efficiency structure reported for the PVSD MSM, namely the calculation of an AOI modifier, a temperature modifier, and the resulting effective PV efficiency. The main difference is the assessment of PV cell temperature. Therefore, this subsection focuses only on the two STPV cell-temperature approaches implemented in EMS: a NOCT-based approach and a heat-balance-based approach. Case-specific window identifiers used in the IDF are replaced by the generic suffix <window>.

The NOCT-based approach adapts the opaque-PV temperature formulation by using the front-face temperature of glazing layer 1 as the temperature basis. The heat-balance-based approach instead uses EnergyPlus window heat-balance outputs to reconstruct an approximate PV laminate temperature from the outer glazing surface conditions. The EMS implementation of both STPV PV cell-temperature assessment approaches and their corresponding temperature modifiers is summarized in Algorithm A3. In this implementation, EnergyPlus solves the window heat balance, while EMS uses selected heat-balance outputs to calculate the temperature variable used in the PV efficiency correction.

Table A18. EMS sensor inputs used for the STPV PV cell-temperature assessment.

Generic EMS Sensor	EnergyPlus Output Variable Read by EMS	Role in STPV Temperature Calculation	Used in
T1_<window>	Surface Window Front Face Temperature Layer 1	Front-face temperature of the outer glazing/PV laminate layer	NOCT and heat-balance approaches
q_sol_<window>	Surface Outside Face Incident Solar Radiation Rate per Area	Total incident solar radiation on the STPV window	NOCT and heat-balance approaches
T_o_<window>	Surface Outside Face Outdoor Air Drybulb Temperature	Outdoor air temperature at the STPV surface	Heat-balance approach
h_o_<window>	Surface Outside Face Convection Heat Transfer Coefficient	Outside-face convection coefficient	Heat-balance approach
q_LW_net_<window>	Surface Outside Face Net Thermal Radiation Heat Gain Rate per Area	Net longwave radiation heat-gain term at the outside face	Heat-balance approach

Table A19. Constants used in the STPV PV cell-temperature assessment.

EMS Variable	Value	Unit	Description	Used in
rho_lam	0.11	dimensionless	Solar reflectance of the PV laminate	Heat-balance approach
tau_lam	0.30	dimensionless	Solar transmittance of the PV laminate	
U_lam	97.282791	W/m^2K	Conductance term used for PV laminate temperature reconstruction	
NOCT	45	°C	Nominal operating cell temperature	NOCT approach
gamma	−0.002	1/°C	Relative temperature coefficient for a-Si PV, equivalent to −0.2%/°C	Downstream temperature modifier

Algorithm A3. EMS-Style Pseudocode for the STPV PV Cell-Temperature Assessment

Step 1: Constant Initialization for STPV Temperature Assessment
SET gamma = −0.002
SET rho_lam = 0.11
SET tau_lam = 0.3
SET U_lam = 97.282791
SET NOCT = 45

Step 2: NOCT-Based PV Cell Temperature
SET Tambient_<window> = T1_<window>
SET T_PV_NOCT_<window> = Tambient_<window>
+ q_sol_<window> * (NOCT - 20)/800

Step 3: Heat-Balance-Based PV Cell Temperature
SET term_1_<window> = q_LW_net_<window>
SET term_2_<window> = h_o_<window> * (T_o_<window> - T1_<window>)

IF q_sol_<window> == 0
SET term_3_<window> = 0
ELSE
SET alpha_lam_<window> = 1 - rho_lam - tau_lam
SET term_3_<window> = (alpha_lam_<window> * q_sol_<window>)/2
ENDIF

SET term_X_<window> = term_1_<window> + term_2_<window> +
term_3_<window>
SET T2_<window> = T1_<window> - (term_X_<window>/U_lam)
SET T_PV_HB_<window> = (T1_<window> + T2_<window>)/2

Step 4: Temperature Modifier for the NOCT-Based Approach
SET MTEMP_NOCT_<window> = 1 + (gamma * (T_PV_NOCT_<window> - 25))

IF MTEMP_NOCT_<window> > 1
SET MTEMP_NOCT_<window> = 1

Algorithm A3. *Cont.*

ENDIF

Step 5: Temperature Modifier for the Heat-Balance-Based Approach
SET MTEMP_HB_<window> = 1 + (gamma * (T_PV_HB_<window> - 25))

IF MTEMP_HB_<window> > 1
SET MTEMP_HB_<window> = 1
ENDIF

Table A20. EMS calling points and temperature-related outputs for the STPV PV cell-temperature assessment.

EMS Component	Implementation in the STPV First-Run IDF
Constant-initialization calling point	BeginTimestepBeforePredictor
STPV temperature-calculation calling point	InsideHVACSystemIterationLoop
Temperature programs called	PV_Temp_Program_HB_<window>; PV_Temp_Program_NOCT_<window>; TemperatureModifier_Program_HB_<window>; TemperatureModifier_Program_NOCT_<window>
Temperature-related EMS outputs	T_PV_HB_<window>; T_PV_NOCT_<window>; MTEMP_HB_<window>; MTEMP_NOCT_<window>
EMS output type and reporting basis	Averaged; ZoneTimestep

Implementation Note: The pseudocode reports only the two PV cell-temperature assessment approaches used for STPVs. The downstream AOI modifier and effective-efficiency formulation follow the same structure as the PVSD MSM, with STPV-specific input values for the PV technology and window geometry.

Appendix E.4. STPV MSM EMS Coupled Formulation Code Structure

In the coupled STPV MSM formulation, the PV conversion efficiency is also reflected in the optical definition of the STPV glazing. The EMS first calculates an effective reflectance by adding the base solar reflectance of the PV laminate to the effective PV efficiency. The resulting value is then used to select one of several predefined STPV window constructions with different outward solar reflectance values. The selected construction is assigned to the STPV window surface through an EMS construction-state actuator.

In this study, the coupled logic was evaluated for both STPV cell-temperature approaches. Algorithm A4 therefore uses the generic placeholder eta_eff_<window>, which can refer to the effective efficiency calculated from either the NOCT-based or the heat-balance-based temperature approach.

The decoupled STPV formulation is not reported separately because it uses the effective-efficiency output as the PV input without changing the glazing construction during the simulation. Therefore, the additional EMS logic needed for the coupled formulation is limited to the effective-reflectance calculation, construction-state definitions, and construction-state switching.

Table A21. EMS objects used for STPV construction-state switching.

EMS Object Type	Generic Name	Role in the Coupled Formulation
EnergyManagementSystem:Actuator	STPV_Actuator_<window>	Assigns a construction state to the selected STPV window surface
Actuated component unique name	<STPV window surface>	Identifies the STPV window surface whose construction is switched
Actuated component type	Surface	Defines the actuated EnergyPlus object type
Actuated component control type	Construction State	Allows EMS to switch the window construction
EnergyManagementSystem:ConstructionIndexVariable	STPV_Window_00 to STPV_Window_05	Provides EMS-accessible references to the predefined STPV constructions

Table A21. *Cont.*

EMS Object Type	Generic Name	Role in the Coupled Formulation
EMS effective-reflectance variable	rho_eff_<window>	Stores the effective reflectance used for construction-state selection
EMS selection variable	R_<window>	Temporary variable used to compare effective reflectance against the switching thresholds

Table A22. STPV construction states used for effective-reflectance discretization.

EMS Construction State	Outside Layer	Front-Side Solar Reflectance at Normal Incidence [-]
STPV_Window_00	aSi_PV_laminate_00	0.11
STPV_Window_01	aSi_PV_laminate_01	0.12
STPV_Window_02	aSi_PV_laminate_02	0.13
STPV_Window_03	aSi_PV_laminate_03	0.14
STPV_Window_04	aSi_PV_laminate_04	0.15
STPV_Window_05	aSi_PV_laminate_05	0.16

The predefined STPV constructions use the same construction sequence and differ only in the outward, front-side solar reflectance assigned to the a-Si PV laminate layer. This discretization allows EMS to approximate the time-varying effective reflectance by switching between otherwise equivalent glazing constructions.

Algorithm A4. EMS-Style Pseudocode for Effective-Reflectance Calculation and Construction-State Switching in the STPV MSM Coupled Formulation

Step 1: Define the Construction-State Actuator

```
EnergyManagementSystem:Actuator,
STPV_Actuator_<window>,          !- Name
<STPV window surface>,           !- Actuated Component Unique Name
Surface,                         !- Actuated Component Type
Construction State;              !- Actuated Component Control Type
```

Step 2: Define the EMS Construction Index Variables

```
EnergyManagementSystem:ConstructionIndexVariable,
STPV_Window_00,                  !- Name
STPV_Window_00;                  !- Construction Object Name

EnergyManagementSystem:ConstructionIndexVariable,
STPV_Window_01,                  !- Name
STPV_Window_01;                  !- Construction Object Name

EnergyManagementSystem:ConstructionIndexVariable,
STPV_Window_02,                  !- Name
STPV_Window_02;                  !- Construction Object Name
```

Algorithm A4. *Cont.*

```
EnergyManagementSystem:ConstructionIndexVariable,
STPV_Window_03,                    !- Name
STPV_Window_03;                    !- Construction Object Name

EnergyManagementSystem:ConstructionIndexVariable,
STPV_Window_04,                    !- Name
STPV_Window_04;                    !- Construction Object Name

EnergyManagementSystem:ConstructionIndexVariable,
STPV_Window_05,                    !- Name
STPV_Window_05;                    !- Construction Object Name
```

Step 3: Calculate the Effective Reflectance

```
IF Warmupflag == 1
SET rho_eff_<window> = rho_lam + eta_nom
ELSE
SET rho_eff_<window> = rho_lam + eta_eff_<window>
ENDIF
```

Step 4: Select the Construction State Based on Effective Reflectance

```
SET R_<window> = rho_eff_<window>

IF R_<window> < 0.12
SET STPV_Actuator_<window> = STPV_Window_00
ELSEIF R_<window> < 0.13
SET STPV_Actuator_<window> = STPV_Window_01
ELSEIF R_<window> < 0.14
SET STPV_Actuator_<window> = STPV_Window_02
ELSEIF R_<window> < 0.15
SET STPV_Actuator_<window> = STPV_Window_03
ELSEIF R_<window> < 0.16
SET STPV_Actuator_<window> = STPV_Window_04
ELSE
SET STPV_Actuator_<window> = STPV_Window_05
ENDIF
```

Table A23. EMS calling points used for the STPV coupled formulation.

EMS Program Calling Manager	Calling Point	Programs Called	Role
Initialize_Constant_Variables	BeginTimestepBeforePredictor	Constant_Variables_Program	Initializes constants such as rho_lam, eta_nom, and other MSM parameters
PreStateSelection_Calculations_<window>	InsideHVACSystemIterationLoop	Temperature, AOI, effective-efficiency, and effective-reflectance programs	Calculates the effective efficiency and effective reflectance before construction-state selection

Table A23. *Cont.*

EMS Program Calling Manager	Calling Point	Programs Called	Role
STPV_Select_State_<window>	InsideHVACSystemIterationLoop	STPV_SelectState_Program_<window>	Assigns the corresponding STPV construction state through the EMS actuator

In the uploaded representative IDF, the construction-state selection is implemented for two STPV window surfaces. Algorithm A4 reports the generalized structure for one representative window only. The placeholder <window> denotes the window-specific EMS identifier, while <STPV window surface> denotes the EnergyPlus surface whose construction state is actuated.

References

1. United Nations Environment Programme. *Global Status Report for Buildings and Construction 2024/25: Not Just Another Brick in the Wall*; United Nations Environment Programme: Nairobi, Kenya, 2025.
2. European Commission. Nearly-Zero Energy and Zero-Emission Buildings. Available online: https://energy.ec.europa.eu/topics/energy-efficiency/energy-performance-buildings/nearly-zero-energy-and-zero-emission-buildings_en (accessed on 17 March 2026).
3. Bonomo, P.; Frontini, F.; Loonen, R.; Reinders, A.H.M.E. Comprehensive review and state of play in the use of photovoltaics in buildings. *Energy Build.* **2024**, *323*, 114737. [CrossRef]
4. Kirimtat, A.; Tasgetiren, M.F.; Brida, P.; Krejcar, O. Control of PV integrated shading devices in buildings: A review. *Build. Environ.* **2022**, *214*, 108961. [CrossRef]
5. Yu, G.; Yang, H.; Luo, D.; Cheng, X.; Ansah, M.K. A review on developments and researches of building integrated photovoltaic (BIPV) windows and shading blinds. *Renew. Sustain. Energy Rev.* **2021**, *149*, 111355. [CrossRef]
6. Romaní, J.; Ramos, A.; Salom, J. Review of Transparent and Semi-Transparent Building-Integrated Photovoltaics for Fenestration Application Modeling in Building Simulations. *Energies* **2022**, *15*, 3286. [CrossRef]
7. Martín-Chivelet, N.; Kapsis, K.; Wilson, H.R.; Delisle, V.; Yang, R.; Olivieri, L.; Polo, J.; Eisenlohr, J.; Roy, B.; Maturi, L.; et al. Building-Integrated Photovoltaic (BIPV) products and systems: A review of energy-related behavior. *Energy Build.* **2022**, *262*, 111998. [CrossRef]
8. Solar Architecture. In a Nutshell: Freiburg City Hall. 2024. Available online: https://solarchitecture.ch/in-a-nutshell-freiburg-city-hall/ (accessed on 13 May 2026).
9. Onyx Solar. Seneca College. Available online: https://onyxsolar.com/seneca-college (accessed on 13 May 2026).
10. Corti, P.; Bonomo, P.; Frontini, F. Paper Review of External Integrated Systems as Photovoltaic Shading Devices. *Energies* **2023**, *16*, 5542. [CrossRef]
11. Zhang, X.; Lau, S.-K.; Lau, S.S.Y.; Zhao, Y. Photovoltaic integrated shading devices (PVSDs): A review. *Sol. Energy* **2018**, *170*, 947–968. [CrossRef]
12. Joseph, B.; Pogrebnaya, T.; Kichonge, B. Semitransparent Building-Integrated Photovoltaic: Review on Energy Performance, Challenges, and Future Potential. *Int. J. Photoenergy* **2019**, *2019*, 5214150. [CrossRef]
13. Bragança, L.; Vieira, S.M.; Andrade, J.B. Early Stage Design Decisions: The Way to Achieve Sustainable Buildings at Lower Costs. *Sci. World J.* **2014**, *2014*, 365364. [CrossRef] [PubMed]
14. de Medeiros, J.V.F.F.; Gomes, E.T.A.; Alonso-Suárez, R.; de Castro Vilela, O. Combining physical models to estimate PV power: Evaluation and optimal modeling in the solar resource-rich semi-arid Brazilian region. *Renew. Energy* **2026**, *256*, 123999. [CrossRef]
15. Gonçalves, A.; Rativa, D.; Gómez-Malagón, L.A. Model-Based Assessment of the Incident Angle Modifier on the Annual Angular Losses and Gain of PV Modules in Tracking Systems. *IEEE J. Photovolt.* **2024**, *14*, 185–193. [CrossRef]
16. Martin, N.; Ruiz, J.M. Calculation of the PV modules angular losses under field conditions by means of an analytical model. *Sol. Energy Mater. Sol. Cells* **2001**, *70*, 25–38. [CrossRef]
17. Dubey, S.; Sarvaiya, J.N.; Seshadri, B. Temperature Dependent Photovoltaic (PV) Efficiency and Its Effect on PV Production in the World—A Review. *Energy Procedia* **2013**, *33*, 311–321. [CrossRef]
18. Leite Didoné, E.; Wagner, A. Semi-transparent PV windows: A study for office buildings in Brazil. *Energy Build.* **2013**, *67*, 136–142. [CrossRef]
19. Zhou, H.; Peng, J.; Rose Wilson, H.; Wang, M.; Jonsson, J.; Ma, T.; Wu, B.; Wu, B.; Fu, G. Investigation of decoupling of thermal and electrical performance of semi-transparent photovoltaic windows based on the external quantum efficiency. *Energy Build.* **2022**, *277*, 112539. [CrossRef]

20. Wijeratne, W.M.P.U.; Yang, R.J.; Too, E.; Wakefield, R. Design and development of distributed solar PV systems: Do the current tools work? *Sustain. Cities Soc.* **2019**, *45*, 553–578. [CrossRef]
21. Yang, R.; Wijeratne, W.M.P.U.; Zhao, H.; Martín-Chivelet, N.; Saretta, E.; Bonomo, P.; Eisenlohr, J. *BIPV Digitalization: Design Workflows and Methods—A Global Survey*; IEA-PVPS T15-14:2022; International Energy Agency Photovoltaic Power Systems Programme: Paris, France, 2022.
22. Jing Yang, R.; Zhao, Y.; Dev Sureshkumar Jayakumari, S.; Schneider, A.; Prithivi Rajan, S.; Leloux, J.; Alamy, P.; Prasetyo Raharjo, G.; Rende, F.; Samarasinghalage, T.; et al. Digitalising BIPV energy simulation: A cross tool investigation. *Energy Build.* **2024**, *318*, 114484. [CrossRef]
23. Saber, E.M.; Lee, S.E.; Manthapuri, S.; Yi, W.; Deb, C. PV (photovoltaics) performance evaluation and simulation-based energy yield prediction for tropical buildings. *Energy* **2014**, *71*, 588–595. [CrossRef]
24. Mun, S.-H.; Kang, J.; Kwak, Y.; Jeong, Y.-S.; Lee, S.-M.; Huh, J.-H. Limitations of EnergyPlus in analyzing energy performance of semi-transparent photovoltaic modules. *Case Stud. Therm. Eng.* **2020**, *22*, 100765. [CrossRef]
25. Pvlib Python Developers. pvlib.iam.martin_ruiz. Available online: https://pvlib-python.readthedocs.io/en/v0.7.2/generated/pvlib.iam.martin_ruiz.html (accessed on 13 December 2025).
26. Solargis. Argus PV Simulation Chain. 2026. Available online: https://kb.solargis.com/docs/solargis-evaluate-simulation-chain (accessed on 13 December 2025).
27. Ghosh, A. Potential of building integrated and attached/applied photovoltaic (BIPV/BAPV) for adaptive less energy-hungry building's skin: A comprehensive review. *J. Clean. Prod.* **2020**, *276*, 123343. [CrossRef]
28. Duffie, J.A.; Beckman, W.A. Design of Photovoltaic Systems. In *Solar Engineering of Thermal Processes*; John Wiley & Sons: Hoboken, NJ, USA, 2013.
29. Toledo, C.; López-Vicente, R.; Abad, J.; Urbina, A. Thermal performance of PV modules as building elements: Analysis under real operating conditions of different technologies. *Energy Build.* **2020**, *223*, 110087. [CrossRef]
30. Davis, M.W.; Fanney, A.H.; Dougherty, B.P. Prediction of Building Integrated Photovoltaic Cell Temperatures*. *J. Sol. Energy Eng.* **2001**, *123*, 200–210. [CrossRef]
31. U.S. Department of Energy. *EnergyPlus Version 24.2.0 Documentation: Engineering Reference, Version 24.2.0*; Build 94a887817b; U.S. Department of Energy: Washington, DC, USA, 2024.
32. U.S. Department of Energy. *EnergyPlus Version 24.2.0 Documentation: Application Guide for EMS, Version 24.2.0*; Build 94a887817b; U.S. Department of Energy: Washington, DC, USA, 2024.
33. Liu, J.; Bi, G.; Gao, G.; Zhao, L. Optimal design method for photovoltaic shading devices (PVSDs) by combining geometric optimization and adaptive control model. *J. Build. Eng.* **2023**, *69*, 106101. [CrossRef]
34. European Commission, Joint Research Centre. Photovoltaic Geographical Information System (PVGIS). 2026. Available online: https://joint-research-centre.ec.europa.eu/photovoltaic-geographical-information-system-pvgis_en (accessed on 13 May 2026).
35. Ladybug Tools LLC. Ladybug Tools. Available online: https://www.ladybug.tools/index.html (accessed on 13 May 2026).
36. Martellotta, F.; Cannavale, A.; Ayr, U. Comparing energy performance of different semi-transparent, building-integrated photovoltaic cells applied to "reference" buildings. *Energy Procedia* **2017**, *126*, 219–226. [CrossRef]
37. Tian, H.; Zhang, W.; Xie, L.; Wu, Y.; Sun, Y.; Chen, M.; Wang, W.; Wu, X. Study on the Energy Saving Potential for Semi-Transparent PV Window in Southwest China. *Energies* **2018**, *11*, 3239. [CrossRef]
38. Roberts, F.; Yang, S.; Du, H.; Yang, R. Effect of semi-transparent a-Si PV glazing within double-skin façades on visual and energy performances under the UK climate condition. *Renew. Energy* **2023**, *207*, 601–610. [CrossRef]
39. Moralejo-Vázquez, F.J.; Martín-Chivelet, N.; Olivieri, L.; Caamaño-Martín, E. Luminous and solar characterization of PV modules for building integration. *Energy Build.* **2015**, *103*, 326–337. [CrossRef]
40. Lawrence Berkeley National Laboratory. WINDOW Software Downloads. 2025. Available online: https://windows.lbl.gov/window-software-downloads (accessed on 14 May 2026).
41. Duran, A.; Waibel, C.; Schlueter, A. A Parametric Approach to Evaluate the Impact of BIPV Façades on Outdoor Thermal Comfort in Different Urban Contexts. In Proceedings of the 18th IBPSA Building Simulation Conference, Shanghai, China, 4 September 2023; pp. 1665–1672. [CrossRef]
42. pvlib.modelchain.ModelChain.with_pvwatts—Pvlib Python 0.15.1 Documentation. Available online: https://pvlib-python.readthedocs.io/en/stable/reference/generated/pvlib.modelchain.ModelChain.with_pvwatts.html (accessed on 11 June 2026).
43. PVGIS 5 User Manual-Joint Research Centre-European Commission. Available online: https://joint-research-centre.ec.europa.eu/photovoltaic-geographical-information-system-pvgis/using-pvgis-5/pvgis-5-user-manual_en (accessed on 11 June 2026).
44. Milosavljević, D.D.; Kevkić, T.S.; Jovanović, S.J. Review and validation of photovoltaic solar simulation tools/software based on case study. *Open Phys.* **2022**, *20*, 431–451. [CrossRef]

45. Chivelet, N.M.; Kapsis, C.; Frontini, F. *Building-Integrated Photovoltaics: A Technical Guidebook*; Routledge: New York, NY, USA, 2025.
46. Mittal, A.; Rennhofer, M.; Dangel, A.; Duman, B.; Schlosser, V. Power change in amorphous silicon technology by low temperature annealing. *EPJ Photovolt.* **2015**, *6*, 65304. [CrossRef]
47. Curcija, C.; Vidanovic, S.; Hart, R.; Jonsson, J.; Powles, R. *WINDOW Technical Documentation*; Lawrence Berkeley National Laboratory: Berkeley, CA, USA, 2018.

Disclaimer/Publisher's Note: The statements, opinions and data contained in all publications are solely those of the individual author(s) and contributor(s) and not of MDPI and/or the editor(s). MDPI and/or the editor(s) disclaim responsibility for any injury to people or property resulting from any ideas, methods, instructions or products referred to in the content.